

LANCASTER UNIVERSITY

**New Methods of Measurements in
Superfluid Helium**

by

Mark Theodore Noble, MPhys (Hons)

*This thesis is submitted in partial fulfilment of the requirements for the degree of
Doctor of Philosophy*

in the

Faculty of Science and Technology
Department of Physics



September 2019

Declaration of Authorship

I declare that the work contained within this thesis is the author's own work and has not been submitted for the award of a higher degree at any other university. The work described is part of a collaborative effort of the Lancaster University Ultra-Low Temperature Physics group, however the majority of the analysis and data taking was performed by the author, except where otherwise noted.

I confirm that the total length of this thesis is 26688 words and does not exceed the 80000 word limit of a PhD thesis.

The following publications are published works of the author and others that contain work that has contributed to this thesis, correct as of the time of publication of this thesis:

- D. I. Bradley, R. P. Haley, S. Kafanov, M. T. Noble, G. R. Pickett, V. Tsepelin, J. Vonka and T. Wilcox, "Probing Liquid ^4He with Quartz Tuning Forks Using a Novel Multifrequency Lock-in Technique", *Journal of Low Temperature Physics* **184**, 1080–1091 (2016).
- A. M. Guénault, R. P. Haley, S. Kafanov, M. T. Noble, G. R. Pickett, M. Poole, R. Schanen, V. Tsepelin, J. Vonka, T. Wilcox, and D. E. Zmееv, "Acoustic damping of quartz tuning forks in normal and superfluid ^3He ", *Physical Review B* **100**, 104526 (2019).

Mark Theodore Noble, MPhys (Hons)

Abstract

Mark Theodore Noble, MPhys (Hons)

New Methods of Measurements in Superfluid Helium

Doctor of Philosophy, September 2019.

In this thesis we use quartz tuning fork resonators to probe properties of normal and superfluid ^4He and ^3He . Our main goal is to study both quantum turbulence and acoustic emission of tuning forks in liquid helium.

By employing a multi-frequency lock-in amplifier we contrast single and multi-frequency methods of measuring tuning forks in the linear regime. In the non-linear response of tuning forks during turbulence we create multi-frequency excitations called intermodulation products which are used to find the non-linear forces that created them. We apply this technique to quantum turbulence in superfluid $^4\text{He-II}$ and find that the retarding in-phase force on the fork increases at a critical velocity for turbulence nucleation. We also observe that the out-of-phase non-linear force increases, which we attribute to energy loss via vortex ring emission by the fork.

Superfluid ^3He is a fermionic condensate of Cooper pairs of ^3He atoms. At ultra-low temperatures of $120\ \mu\text{K}$ thermally excited unpaired quasiparticles travel ballistically through the condensate. We beam quasiparticles from a black body source towards a 5×5 -pixel camera and observe that the excitations follow photonic-like trajectories. We apply the source-camera configuration to non-invasively detect and even image quantum vortices, that are topological defects in the superfluid.

Lastly, we explore the frequency dependent damping of quartz tuning forks in liquid ^3He . We find that at high frequencies the fork damping is governed by acoustic emission. Furthermore, we show that existing models developed for sound emission in ^4He can be used to predict observed acoustic damping in ^3He . The results also suggest that devices for ^3He experiments should be placed in cavities or designed to operate at low frequencies.

Acknowledgements

Much work in modern physics is a group effort, and this work is no different. I here would like to thank all members of the Lancaster Ultra-Low Temperature group for all their assistance and help in my work.

Firstly I thank my supervisor Viktor for always been ready to help with answers or assistance, to any problem not matter the size. From undergraduate director of studies, to masters to PhD it is hard to think of a better supervisor. I also thank my deputy supervisor Rich for wise words and help with administration. I thank Tony for seeing the funny side of life and especially his help in understanding ³He acoustics, he will be sorely missed. I thank Dima for his close reading of paper drafts and letting me relax at his sauna. I thank Sergey for challenging my understanding of physics and providing the fork SEM images. I also thank George, Roche, Ian and Mal for occasional knowledge and helping hand. Big thanks go to Alan and Martin for fixing pumps and keeping the helium flowing.

My thanks to fellow PhDs of one form and another. Especially Tom Wilcox for sharing many long hours in a warm tin box, solving problems together and sharing a opening year together. I also thank Alex Jones, for his technical knowledge, and willingness to help organise or problem solve practically anything. My PhD would have certainly been a lot harder without you. I thank Jakub and Sarsby for often answering questions and showing the ropes during the first year of my PhD. I thank Andy for his many attempts to get a journal to understand my name and making the office a good place to be. It's a pity I did not get to author that paper 11 times. I thank Josh for been the most friendly guy I know, and frequent lifts to campus. I thank Roscoe for his many interesting off topic chats and co-developing the wraps recipe. Thanks to the rest of the Lunch crew of fellow 'Sheds': Ash, Francis, Matt, Tom, James and Samuli for making life fun and giving lively discussion on varied topics.

I would also like to thank those who inexplicably do not study low temperature physics. I thank my parents, Roger and Lindy, for their love and invaluable help during my write up. Thanks for everything. I thank my brother, Dom, for occasional tech support. I would also like to thank Becky, James, Tom, Mike and Stewart for introducing me to DnD and being great friends to relax with.

Lastly I thank Kathryn, for love, understanding and unconditional support. And also giving up on sleep to take three stranded PhDs to Manchester airport. This all would have been a lot harder without you, and I look forward to continuing our adventures together.

Contents

Declaration of Authorship	iii
Abstract	v
Acknowledgements	vii
1 Introduction	1
1.1 Layout	4
2 Helium Superfluids	5
2.1 Helium-4	5
2.1.1 Landau's Two Fluid Model	7
2.1.2 Circulation Quanta and Quantum vortices	9
2.1.3 Quantum Turbulence	12
2.2 Helium 3	13
2.2.1 Fermi Liquids	14
2.2.2 Collective Modes	15
2.2.3 Superfluid Helium-3	16
2.2.4 Quasiparticle Excitations	20
2.2.5 Quantum Vortices and Quantum Turbulence	21
3 Mechanical Oscillators	23
3.1 Oscillator Basics	23
3.1.1 Vibrating Wire Loop	26
3.1.2 Tuning Forks	28
3.2 Operation and Measurement	30
3.2.1 Frequency Sweep	31
3.2.2 Amplitude Sweep	32
3.2.3 Resonance Tracking	32
3.3 Damping in Helium Liquids	32
3.3.1 Hydrodynamic Regime	33
3.3.2 Ballistic Regime	34
Andreev Reflection	35

3.4	Helium-3 Thermometry	37
4	Refrigeration	39
4.1	^4He Cryostat	39
4.2	Dilution Refrigeration	40
4.3	Adiabatic Nuclear Demagnetisation Refrigeration	43
4.4	Noise and Heat Leak Reduction	47
5	Multi-Frequency Measurements and Techniques	51
5.1	Multi-frequency effects in the Linear Regime	52
5.1.1	Multi-frequency Measurements of a Tuning fork	52
5.1.2	Multi-frequency Measurements of a Fork Cooling in ^4He	55
5.2	Multi-frequency effects in the Non-Linear Regime	57
5.2.1	Intermodulation Products	57
5.2.2	Non-Linear Forces of Quantum Turbulence in ^4He	61
	(A) Emergence of Turbulence	65
	(B) Just Above the Critical Velocity	66
	(C) Far Above the Critical Velocity	66
5.2.3	Discussion	69
5.3	Summary	72
6	A Quasiparticle Camera in $^3\text{He-B}$	75
6.1	Imaging a Quasiparticle Beam	75
6.1.1	Generating Light - The Quasiparticle Source	75
6.1.2	A Quasiparticle Camera	77
6.1.3	Theoretical Prediction of the Black Box Radiator Beam	80
6.1.4	Simulations of the Quasiparticle Beam	81
6.1.5	Measurement Scheme	83
	Data Corrections and Calibrations	83
6.1.6	Measurements of the Quasiparticle Beam	84
6.2	Imaging Quantum Turbulence with Quasiparticles	88
6.2.1	Detecting and Creating Vortices	88
6.2.2	Measurements of the Source Wire Beam	91
6.2.3	Measurements of Quantum Turbulence	95
6.3	Conclusions	98
7	Acoustic Damping of Quartz Tuning Forks in ^3He	101
7.1	Overall Damping Model	101
7.1.1	Acoustic Damping	102
7.2	Acoustic Damping Measurements in ^4He	104

7.3	Measurements in ^3He	106
7.3.1	Initial Fitting Attempts	110
7.3.2	The Effects of Fork Confinement	112
7.3.3	Present Understanding	115
7.4	Conclusions	115
8	Summary	119
	Bibliography	123

List of Figures

2.1	Phase diagram of ^4He	6
2.2	Relative densities of the normal and superfluid factions of He-II	7
2.3	Dispersion curves of a free particle gas and He-II	10
2.4	Superflow velocity about a vortex	11
2.5	Femri-Dirac distribution	14
2.6	Phase diagram of ^3He	17
2.7	Phase diagram of ^3He in a small magnetic field	18
2.8	Phase diagram of ^3He in strong confinement by aerogel	19
2.9	Superfluid ^3He dispersion curve	21
3.1	In and out of phase components of an oscillator	25
3.2	Vibrating Wire Schematic	27
3.3	Quartz Tuning Fork Schematic	28
3.4	A fork scanning electron microscope image	29
3.5	Wire Measurement Scheme Schematic	30
3.6	Andreev's reflection of quasiparticles	35
4.1	^3He - ^4He Mixture Phase Diagram	41
4.2	^3He - ^4He Dilution Refrigerator Photo	42
4.3	Copper Nuclear Energy Levels	44
4.4	Precool Temperature	45
4.5	Entropy temperature curve of cooper	46
4.6	Heating spike in the cell	48
5.1	Single vs Multi-Frequency Techniques	53
5.2	Multi and single frequency measurements of a tuning fork.	54
5.3	Fork Resonance Temperature Dependence	56
5.4	Intermodulation Products	58
5.5	Example spectrum analysis	60
5.6	Force, Velocity and Frequency Measurements of the Fork in He-II at 1.3 K	62
5.7	Turbulent Force Spectrum at the Critical Velocity	64
5.8	Turbulent Non-Linear Forces at the Critical Velocity	65

5.9	Turbulent Force Spectrum above the Critical Velocity	67
5.10	Turbulent Non-Linear Forces above Critical Velocity	68
5.11	Turbulent Force Spectrum far above the Critical Velocity	69
5.12	Turbulent Non-Linear Forces far above the Critical Velocity	70
5.13	Turbulent Non-Linear forces for multiple Velocity Sweeps	71
6.1	Quasiparticle Camera Cell Picture	76
6.2	Quasiparticle Camera Picture	78
6.3	Measurement setup for the Quasiparticle Camera	79
6.4	Dimensions of the camera and BBR	81
6.5	Analytical prediction of the beam profile	82
6.6	Quasiparticle Beam Picture	85
6.7	Quasiparticle Beam Picture	85
6.8	Picture of Quasiparticle Beam of Black Box Radiator	86
6.9	The quasiparticle flux by column with theoretical and simulated models.	87
6.10	Source wire force velocity curve	89
6.11	Andreev Reflection by a Vortex	90
6.12	Source wire beam width parameter vs velocity for amplitude sweeps	92
6.13	Source wire beam width parameter verses velocity for pulsed sweeps	93
6.14	Camera images of the source wire beam	94
6.15	Fractional Screening by Quantum Turbulence during a Amplitude Sweep	95
6.16	Fractional Screening by Quantum Turbulence during a Pulsed Sweep	96
6.17	Pictures of the Quantum Turbulence	97
7.1	3D model acoustic monopole positions	103
7.2	Acoustic damping in ^3He and ^4He	107
7.3	Frequency sweeps of a Fork at multiple temperatures	109
7.4	Fork damping vs magnetic field	111
7.5	^4He camera fork damping against frequency	113
7.6	Fork damping against wavelength of emitted sound in ^4He and ^3He	114
7.7	Acoustic Damping in ^3He	116
8.1	Heat map image of quantum turbulence	120

List of Abbreviations

ac	Alternating Current
AFM	Atomic Force Microscopy
BBR	Blackbody Radiator
BEC	Bose-Einstein Condensate
BCS	Bardeen, Cooper and Schrieffer
DAQ	Data Acquisition instrument
HWD	Height times Width over Drive
MEMS	Microelectromechanical System
MLA	Multifrequency Lockin Amplifier
NEMS	Nanoelectromechanical System
SEM	Scanning Electron Microscope

Chapter 1

Introduction

A superfluid is a fluid that flows with no viscosity, such that a ball moving through the fluid would feel nothing. First discovered in ^4He in 1938[1, 2] this is an ideal example of a macroscopic quantum mechanical effect that you can see with your own eyes. For example if a beaker of superfluid ^4He is lifted out from the main bath, the superfluid in the beaker will crawl up and out of the beaker and return to the bath. It flows through the thin film of liquid helium attached to the walls by intermolecular forces. Despite this though some similarities remain between these fluids and classical fluids.

Imagine spinning a bucket of superfluid - naively we would think the bucket would have no effect on the superfluid and the superfluid surface would be flat. Alternatively if we spun a bucket of water, a normal fluid, a meniscus would form with a characteristic dip. Experiments show, however, that superfluid ^4He forms a meniscus[3], just like water. This implies the existence of vortices in the superfluid, although these will be quite different objects to a classical vortex. Returning to our water bucket we find one vortex in the middle with a circulation that is dependent on how fast the water is moving. In the superfluid helium bucket we see multiple *quantum* vortices, with a fixed circulation and size[4]. The large scale motion recreates the same meniscus shape as for the water, but on the microscopic scale there is a group of string-like vortices going through the superfluid. This example shows the possibility of comparisons between the quantum mechanical world of superfluids and the classical world we are familiar with, despite underlying differences.

In everyday life, creating vorticity is associated with turbulent motion in the fluid: airplanes, ships, cars, etc lose energy into the creation of large vortices that decay into smaller and smaller vortices until they are lost to viscous heating in unpredictable chaotic motion. This flow of energy down from large to small scales is known as the Kolmogorov spectrum[5]. Superfluids also experience turbulence. This quantum turbulence is made up of a tangle of string-like vortex filaments which offers a much more conceptually intuitive system to the chaotic dance of classical turbulence. As with the spinning bucket, we have opportunities for comparison between the classical

and quantum worlds. Like classical turbulence the quantum system is believed to follow an energy cascade similar to the Kolmogorov spectrum[6]. The intrinsically chaotic nature of classical turbulence leaves no easy solution and it is largely regarded as the last great problem of classical physics. Further study of quantum turbulence in superfluid helium offers the chance that we may be able to make more comparisons between the quantum and classical world.

Physicists and engineers typically use a wind tunnel with smoke, or a water stream with ink to see turbulence in air and water respectively. These experiments however cannot reach extremely high turbulent flows found in nature, being limited by the viscosity of air and water and the characteristic size of the test object. Helium, even the non-superfluid phase, has much lower viscosity and offers much potential to access turbulent flows not accessible with conventional efforts. Unfortunately however the visualisation of the flow is not possible with smoke or inks in superfluids and alternatives have to be found. The great challenge therefore is to design an experiment capable of picturing or visualising quantum turbulence at these extremely turbulent states. Recent progress has been made with the picturing of tracer molecules in ^4He using a laser[7-9]. Quantum vortices trap the tracer molecules and then the laser can track the movement of the tracers and hence the vortices themselves.

In this work we will be using mechanical oscillatory resonators to investigate and image turbulence in helium. These devices create an oscillatory superflow that we can use to create and detect turbulence via the interactions between the flow and oscillator. Their ease of use allows the user to easily measure the driving force and peak velocity in helium at all currently achievable temperatures. Typically to see turbulence on a resonator one increases the driving force on the oscillator and measures the resultant velocity. By plotting the relationship between the force and velocity one can distinctly see turbulence through a characteristic decrease in the gradient between the two variables from an initial linear relationship. These methods have been extensively applied to turbulence studies in superfluid ^4He [6, 10-14] and ^3He [15-17].

The method used to study turbulence detects the turbulent damping force on the oscillator from the changes in driving force's velocity relationship. However it is possible to directly see the effects of non-linear forces (such as turbulence) on an oscillator using multi-frequency driving forces. These methods developed by the atomic force microscopy community increase the available force data from resonators[18, 19]. It seems fairly natural to wonder if the same can be done for resonators probing liquids instead. By verifying that multifrequency methods can be used on our resonators[20] we can pursue the advanced techniques that allow non-linear force extraction[21]. Multi-frequency excitations on a non-linear system create extra frequency excitations from the non-linear forces. By carefully measuring

these excitations we can then derive and separate the non-linear damping force from turbulence into the in-phase and out-of-phase components acting on a fork.

We will also pursue a method to directly image turbulence via a elegant solution using thermal quasiparticles in superfluid $^3\text{He-B}$. Liquid ^3He is a Fermi liquid system which becomes a superfluid at about 1 mK by forming Cooper pairs of ^3He atoms[4]. The remaining thermal energy leaves unpaired particles that continue to travel as thermal quasiparticles. Lowering the temperature naturally reduces the population of thermal excitations and at ultra low temperatures the population becomes so low that the mean free path for the quasiparticles is far larger than any experimental cell. For our purposes any excitation moves with a ballistic trajectory through the fluid. We can create thermal excitations by breaking Cooper pairs with a heater. If we then place a heater in a box we locally confine the particles inside the box which then thermalise with each other and the walls of the box. A small hole on one side allows the quasiparticles to escape from the box into the bulk fluid as a beam[22].

In front of the beam of quasiparticles we have a vibrating wire that creates a turbulent tangle of quantum vortices. The flow field about the vortices lifts the energy gap of quasiparticles, and some quasiparticles no longer have sufficient energy to carry on into the flow field[23]. The quasiparticles with insufficient energy are Andreev reflected becoming their anti-partner (quasiparticle to a hole and vice versa) while the quasiparticles with higher energies can travel onward through the vortex flow field. Therefore behind the vortex there is a decrease in the flux of quasiparticles. By measuring the flux with a camera we can then image quantum turbulence by the flux shadow it leaves behind[24].

We use 25 quartz tuning fork resonators in a 5 by 5 grid surrounded by a copper matrix to form the quasiparticle camera[24]. Quasiparticles incident on a fork exchange their momentum with the fork causing the fork's resonance width to increase. By measuring the resonance width of the forks simultaneously we can take a image of the quasiparticle flux on the camera. By comparing an image of the beam and the turbulent pictures we can deduce the shadow of the vortex tangle. This shadowgram allows us to image turbulence in a unique manner without significantly disturbing the fluid. The momentum exchange between the quasiparticles and quantum vortices is tiny. Furthermore the quasiparticles are integral to the fluid, unlike tracer molecules so the chance of a disturbance is reduced.

The measurement of the quasiparticle flux is highly dependent on the sensitivity of the resonators chosen. The quartz tuning forks we use are highly sensitive to small changes in the surrounding fluid. However it is known that in ^4He that at higher frequencies the sensitivity of forks and other devices drops off due to sound emission[12, 25]. There has been no detailed study into sound emission by these structures in ^3He . It is important that we understand the damping effects of the fluid

which may affect the sensitivity of our devices, to avoid a significant loss of effort. This is important because the next generation of quasiparticle camera may include forks with a high range of frequencies or nanoelectromechanical devices (NEMS)[26, 27] which have a much larger frequency range.

We will present the first systematic type study of acoustic damping in ^3He . We will be using the 25 forks of the quasiparticle camera to study the frequency dependent damping in normal and superfluid ^3He . It is likely that the current model for ^4He can describe sound emission in ^3He , but ^3He has collective modes not found in ^4He which may affect the forks: namely zero sound and spin waves. The experiments described here will test the established ^4He model against the results in ^3He . Knowledge on how the sound emission affects the sensitivity of higher frequency devices can help inform the design next generation of nano-scaled resonators for ^3He experiments.

1.1 Layout

Chapter 2 is an introduction to the physics of both ^4He and ^3He . It will cover the basics of the condensation into a superfluid in both liquids and introduces excitations and vortices in the fluids.

Chapter 3 will discuss the mechanical oscillators used as tools to study helium. The chapter starts with the basics of an oscillator, then discusses the damping effects of helium fluids, and shows the use of oscillators as thermometers in ^3He .

In chapter 4 the refrigeration techniques used in this work are considered: both the fridge used to cool ^4He to a superfluid, and the fridge used to achieve the ultra-low temperatures that superfluid $^3\text{He-B}$ exists in.

Chapter 5 will present multi-frequency measurements using a multi-frequency lock-in amplifier. We show that single and multi-frequency techniques get the same results for tuning fork oscillators at low excitations. Non-linear multi-frequency mixing effect of intermodulation products are then used to measure quantum turbulence on tuning forks at higher excitations.

In chapter 6 we present the results of measurements of a quasiparticle camera in superfluid $^3\text{He-B}$ at ultra-low temperatures.

Chapter 7 uses the tuning forks from the quasiparticle camera to measure the acoustic damping felt by the forks in normal and superfluid $^3\text{He-B}$. We will compare these results with measurements taken in ^4He and theoretical models developed to explain acoustic damping in ^4He .

Lastly chapter 8 will summarise the results of this work.

Chapter 2

Helium Superfluids

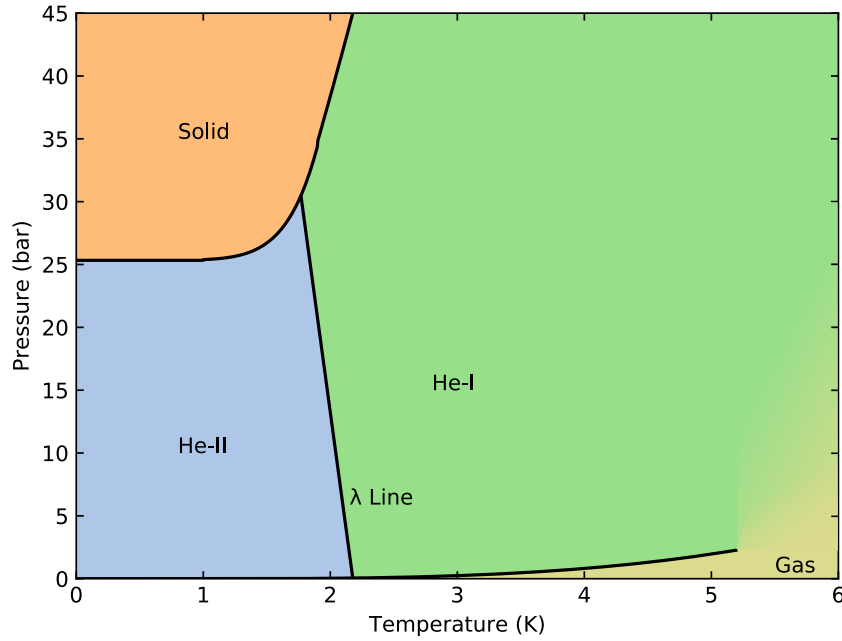
In 1868 the astronomers Jules Janssen and Norman Lockyer discovered anomalous absorption lines in the solar spectrum of the sun[28]. Lockyer proposed that these lines were caused by an unknown element. He subsequently, along with Edward Frankland, named the new element after the Sun using its greek name, *Helios*; and so Helium joined the periodic table of elements.

It took until 1895 to discover terrestrial helium in uranium ore[29]. The reason for its apparent scarcity, despite being the second most common element in the universe, is that helium in the atmosphere is so light that it will be lost to space. Any terrestrial occurrence of the heavier stable isotope ^4He comes from the natural radioactive decay of elements in the Earth's crust. Helium-4 then accumulates in oil fields and ores and is today largely produced as by-product of the oil industry. Back in the 1890-1900s these sources were underdeveloped and it took considerable time and effort to accumulate enough helium to start attempts into condensing the gas into a liquid.

2.1 Helium-4

Helium-4 was first liquefied by Heike Kamerlingh Onnes in 1908 in experiments cooling it down to 1.5 K[30]. Unfortunately, he did not notice the phase transition between the two liquid phases of ^4He . That discovery was made later by a student of his, Keesom, who along with Clusius in 1932 measured the specific heat capacity of ^4He . They discovered the tell tale discontinuity of a transition at 2.17 K, a point called the λ -point for the unusual shape of the specific heat curve about the transition[31]. Helium-4 above the transition was called He-I while ^4He below was called He-II (see fig. 2.1).

Keesom also looked at viscosity in He-II and discovered a similar figure to He-I. However experiments in 1938 by Kapitsa[1] and, independently, by Allen and Meisener[2], discovered that in certain conditions He-II had no measurable viscosity, or as Kapitsa expressed it: He-II was a 'superfluid.'

FIGURE 2.1: Phase diagram of ${}^4\text{He}$.

Theorists rapidly worked to try and explain the apparently contradictory experimental findings. Fritz London in 1939 suggested that the phenomena was related to Bose-Einstein Condensates (BECs)[32], a state where a macroscopic number of bosons occupy the ground state of the system. The bosons themselves, in BEC theory, are assumed to be a gas with no intermolecular forces. While ${}^4\text{He}$ is bosonic it is also a liquid with strong intermolecular forces breaking some of the assumptions behind BECs, however the theory goes a long way to explaining the fundamental physics of what happens below the lambda point of ${}^4\text{He}$.

Subsequently Tisza suggested a simple phenomenological model to explain what Keeson and Kapitsa had seen[33]. He-II was made up of two fluids: a normal fluid with temperature, viscosity and entropy as measured by Keeson; and a superfluid with zero temperature, viscosity and entropy as measured by Kapitsa. The two fluids interpenetrate each other, and in the absence of excitations they are non-interacting.

The normal and superfluid components, further to having their own temperatures and viscosity, also carry independent densities and velocities: ρ_n , v_n , ρ_s and v_s respectively. The sum of the densities is the density of the He-II ρ as a whole,

$$\rho = \rho_n + \rho_s. \quad (2.1)$$

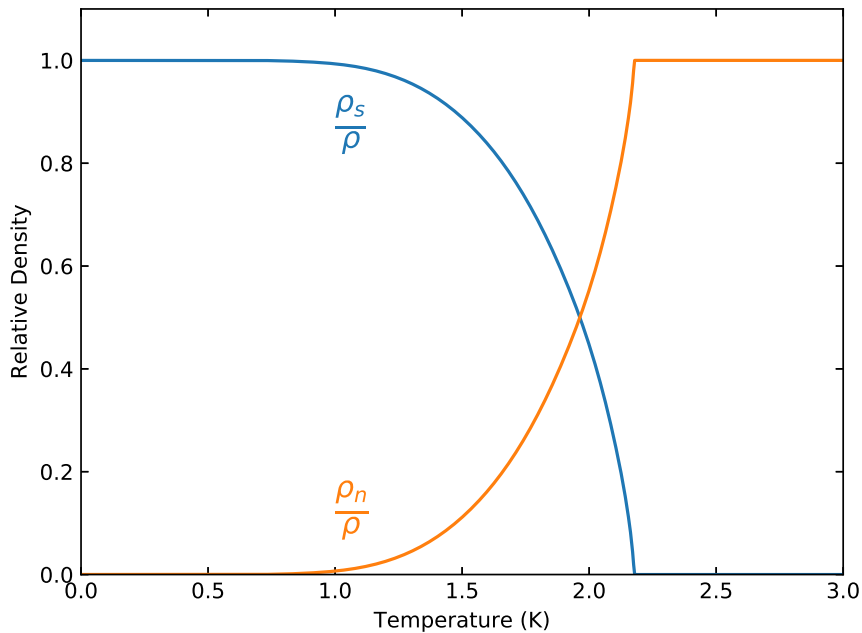


FIGURE 2.2: The fractional relative density as a function of temperature of the normal (orange) and superfluid (blue) components of He-II.

The temperature dependence of ρ_n and ρ_s is plotted in fig. 2.2. Above the λ -point there is 100% normal fluid, which rapidly drops with temperature until around 1 K where there is so little normal fluid fraction left that it is insignificant.

2.1.1 Landau's Two Fluid Model

Landau independently also suggested a two fluid model in much more detail than Tisza[34]. Landau's model considered how excitations would behave in a superfluid and it was a great success in explaining all previous work. Here we will discuss some of its main results.

Landau's key insight was the existence of an energy gap in the superfluid between the ground state and any excitations. If there were no gap any flow could dissipate energy in excitations and the superfluid would not be able to flow with zero viscosity, so there must exist an energy gap.

Consider a large mass M moving through a stationary superfluid at a constant velocity \mathbf{u} that creates an excitation. If an excitation of energy E and momentum \mathbf{p} is created, the velocity of the mass must change to \mathbf{v} to satisfy conservation of

momentum:

$$\mathbf{p} + M\mathbf{v} = M\mathbf{u}, \quad (2.2)$$

$$\mathbf{p} = M(\mathbf{u} - \mathbf{v}), \quad (2.3)$$

and also energy,

$$\frac{1}{2}M|\mathbf{v}|^2 + E = \frac{1}{2}M|\mathbf{u}|^2, \quad (2.4)$$

$$E = \frac{1}{2}M(|\mathbf{u}|^2 - |\mathbf{v}|^2). \quad (2.5)$$

Which tells us the energy of the excitation. We can rearrange this into:

$$E = \frac{1}{2}M(\mathbf{u} \cdot \mathbf{u} - \mathbf{v} \cdot \mathbf{v}), \quad (2.6)$$

$$E = \frac{1}{2}M(\mathbf{u} - \mathbf{v}) \cdot (\mathbf{u} + \mathbf{v}), \quad (2.7)$$

substituting eq. (2.3) into eq. (2.7) and we find that:

$$E = \frac{1}{2}\mathbf{p} \cdot (\mathbf{u} + \mathbf{v}), \quad (2.8)$$

$$E = \frac{1}{2}\mathbf{p} \cdot (2\mathbf{u} - [\mathbf{u} - \mathbf{v}]). \quad (2.9)$$

The excitation's mass will be much less than the mass of the large mass, this in turn implies that the velocity before and after will be approximately the same so that $|\mathbf{u} - \mathbf{v}| \approx 0$. In this limit we can then approximate eq. (2.5) to:

$$E \approx \mathbf{p} \cdot \mathbf{u}. \quad (2.10)$$

The dot product can only be less than the multiplication of the magnitudes of \mathbf{p} and \mathbf{u} so we have the condition that $E \leq pu$. Or alternatively the minimum velocity v_L to create an excitation is

$$v_L = \frac{E}{p}, \quad (2.11)$$

where v_L is Landau's velocity.

In normal fluids we assume a free particle dispersion curve $E = p^2/2m$ shown in fig. 2.3a. Figure 2.3a shows no energy gap to create excited states so any movement can create drag and therefore $v_L = 0$. In the case of superfluid He-II the dispersion curve shown in fig. 2.3b does have a energy gap to reach an excited state and it follows that Landau's velocity is non zero. In He-II Landau's velocity has been measured by ion spectra to be about 50 m s^{-1} [35] which is far above what any macroscopic

experiments are capable of probing.

Macroscopic objects however still feel damping from the superfluid. Resonators can create phonons by acoustic emission and this takes energy away from the resonator[12]. Furthermore at higher velocities that are far below Landau's velocity these objects can feel increased drag. This drag comes from the creation of vortex rings by the object creating turbulence in the superfluid. But to fully explain this we will first discuss quantum vortices.

2.1.2 Circulation Quanta and Quantum vortices

To appreciate quantum vortices first consider that superfluid helium is made up a condensate of atoms all in lowest energy state and hence they share the same coherent wave-function Ψ [36]:

$$\Psi(\mathbf{r}) = \psi_0 e^{i\theta(\mathbf{r})} \quad (2.12)$$

that is a function of the position \mathbf{r} . ψ_0 is an function of the relative superfluid density such that $\psi_0 = \sqrt{\rho_s/\rho}$. Using the momentum operator \mathbf{p} on eq. (2.12) we can find the momentum[4] as:

$$\mathbf{p}\Psi = -i\hbar\nabla\Psi \quad (2.13)$$

and because ψ_0 is constant it follows that:

$$\mathbf{p} = \hbar\nabla\theta \quad (2.14)$$

where \hbar is the reduced Planck constant. We can then rearrange for the velocity using $p = mv$ and find:

$$\mathbf{v}_s = \frac{\hbar}{m}\nabla\theta \quad (2.15)$$

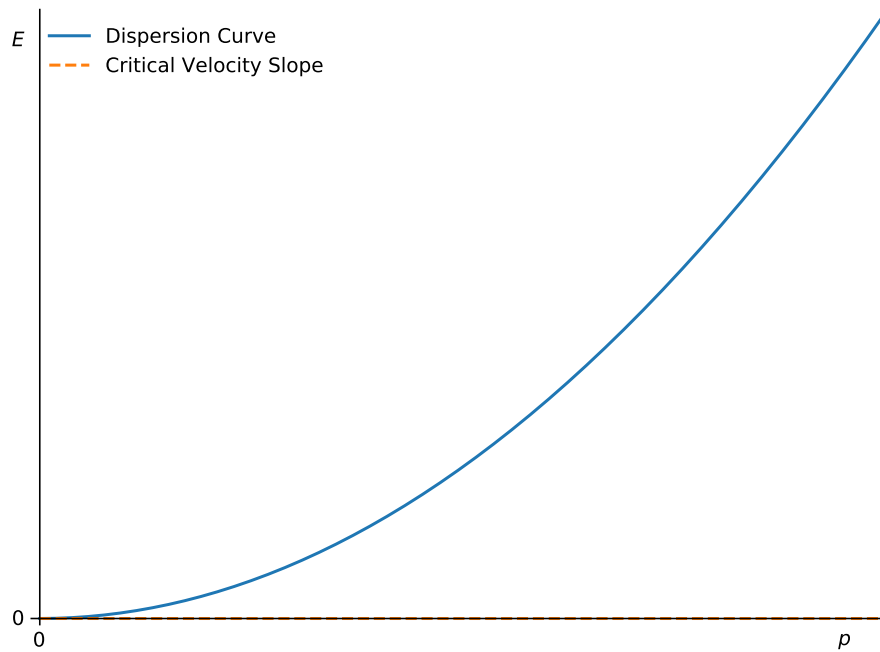
where \mathbf{v}_s is the velocity of the superfluid and m the mass of a ${}^4\text{He}$ particle.

Looking at the definition of vorticity $\boldsymbol{\omega} = \nabla \times \mathbf{v}$ we can see that in a superfluid,

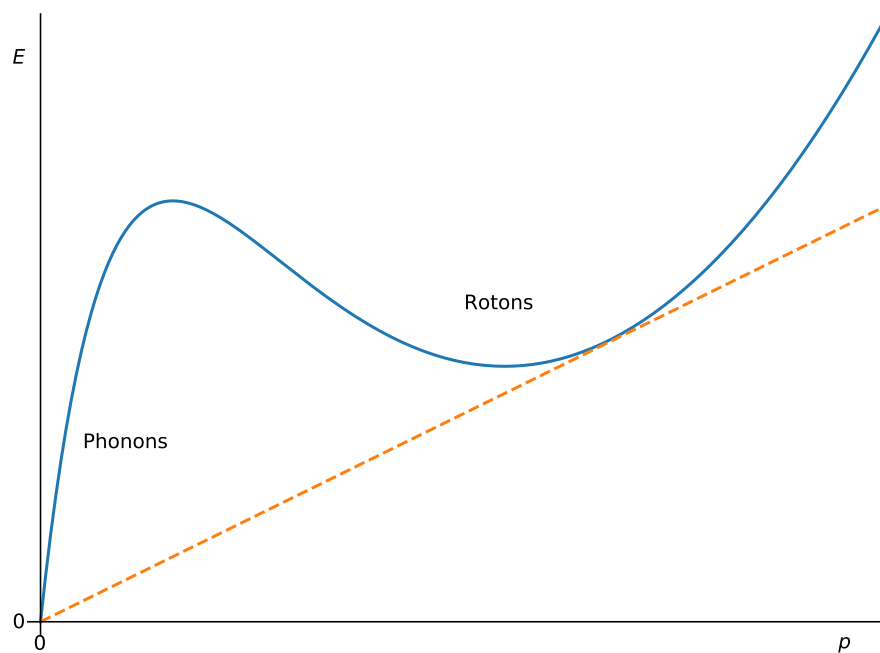
$$\boldsymbol{\omega} = \frac{\hbar}{m}\nabla \times (\nabla\theta) = 0, \quad (2.16)$$

since the curl of the gradient of a scalar field is zero. The identity $\nabla \times \mathbf{v}_s = 0$ directly implies that any superfluid is irrotational. This would seemingly forbid the presence of vortices in a superfluid or any rotational motion. Despite this experiments showed that spinning superfluid ${}^4\text{He}$ still showed a meniscus macroscopically close to that of a classical fluid[3], indicating rotational motion is present in the superfluid.

Looking at the wavefunction Onsager[37] and later Feynman realised[38] that a circulation was not forbidden, and for a superfluid can be found from the circulation



(A) Free Particle Gas



(B) He-II

FIGURE 2.3: The dispersion curves and Landau velocities of a gas of free particles $E = p^2/2m$ (a) and of He-II (b) (not to scale). Note that the free particle gas has no gap and hence zero Landau velocity, while He-II shows a superfluid gap and hence a nonzero Landau velocity (found by the slope of the dashed line.)

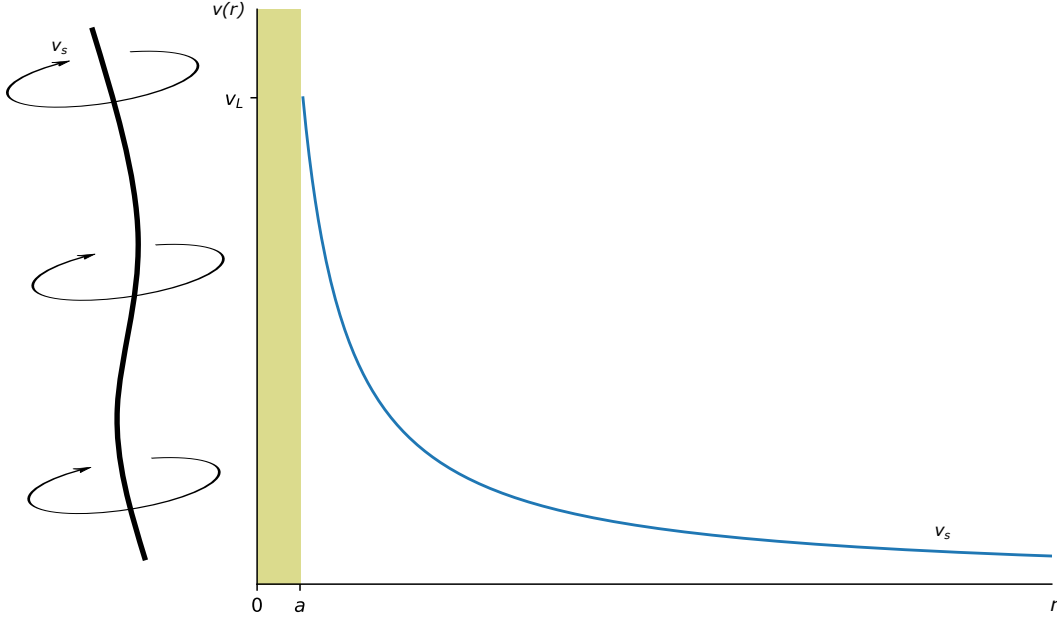


FIGURE 2.4: A illustration of a quantum vortex line and a graph of the superflow velocity about a quantum vortex as function of radius using eq. (2.19). At Landau's velocity v_L the superfluid phase function collapses defining the vortex core radius a .

definition $\Gamma = \oint \mathbf{v} \cdot d\mathbf{l}$ as:

$$\Gamma = \frac{\hbar}{m} \oint \nabla \theta \cdot d\mathbf{l} \quad (2.17)$$

where Γ is the circulation and the integration path is any arbitrary closed loop in the fluid. The integral is closed so the phase can only vary by a factor of 2π about the loop. Therefore

$$\Gamma = \frac{nh}{m} \quad (2.18)$$

where n is any positive non-zero integer. Equation (2.18) shows us that the circulation of a superfluid is quantised with a quantum of $\kappa = h/m$. This suggests a vortex is allowed in a superfluid, although its size will be fixed by the circulation quantum, a quantum vortex.

The quantum of circulation was experimentally confirmed in 1958 by Vinen[39]. Vinen placed a straight oscillatory wire in a rotating He-II cryostat. Vorticity on the wire causes a frequency shift in which he saw distinct steps, confirming that a quantum of circulation exists. The earlier measurements of the meniscus can be explained as large groups of quantum vortices recreating the same effect as classical large scale motion.

This leaves a paradox: we know quantum vortices exist, but the superflow must

be irrotational. The solution is to consider the flow of superfluid about the vortex. Looking at eqs. (2.17) and (2.18) the velocity field about a vortex varies as function of radius r as:

$$v(r) = \frac{\Gamma}{2\pi r}. \quad (2.19)$$

As we approach the vortex core we can assume that the superfluid velocity will eventually exceed Landau's velocity. At this point we know from Landau's two fluid model that the superfluid breaks down. The wave function collapses, decreasing the density of the superfluid leaving normal fluid in the core, and a topological defect in the wavefunction. This gives a neat result that the core region can carry vorticity in the core's normal fluid while the superflow outside the core remains irrotational.

The energy of a vortex can be found from the kinetic energy of the fluid flowing around it:

$$E = \int_V \frac{1}{2} \rho v^2 dV \quad (2.20)$$

where dV is the infinitesimal volume element. Assuming a vortex of length L in the cylindrical reference frame centered on the vortex we get the energy per unit length:

$$\frac{E}{L} = \int_a^R \pi \rho r v^2 dr. \quad (2.21)$$

We assume the volume inside the core radius a can be neglected and R is the radius of interest. Solving eq. (2.21) using eqs. (2.18) and (2.19), and the circulation quantum $\kappa = h/m$, finds the energy of a vortex:

$$E = \frac{\rho L n^2 \kappa^2}{4\pi} \ln \left(\frac{R}{a} \right). \quad (2.22)$$

We can see from eq. (2.22) that the energy is proportional to n^2 . An $n = 2$ vortex will have double the energy of two single quantized vortices. Physically this makes single quantum vortices more energetically favourable. A higher order ($n > 1$) quantum vortex would decay into single quantum vortices.

Using the knowledge that $n = 1$ we can derive the size of a vortex core in the superfluid. Using eq. (2.19) with Landau's velocity in He-II the core has a size of around 0.3 nm which is of order of the coherence length of the superfluid. This small size also justifies the assumption used to derive the vortex energy in eq. (2.21).

2.1.3 Quantum Turbulence

If vortices exist in the fluid it naturally follows that there can also be turbulence. Turbulence in its classical form is an everyday effect that occurs in all fluids. It is created when a fast moving object creates vortices in a fluid that the object is

traveling through. The vortices spread out and interact with each other, getting smaller and smaller until they dissipate through viscose damping at the Kolmogorov length scale[40, 41]. In such a way energy is moved from the moving object and into the fluid, increasing the damping on the object and slowing it down. The process is inherently chaotic and it is impossible to predict how the vortices develop. This makes it hard for engineers to reduce the drag on airplanes, ships etc and so turbulence is often referred to as one of the last great problems of classical physics.

Typically to describe turbulence in viscous fluids the dimensionless Reynolds number Re is used[42]:

$$Re = \frac{\rho v L}{\eta} \quad (2.23)$$

where L is the characteristic size of the system under consideration and η the dynamic viscosity of the fluid. For low Reynolds numbers $Re \ll 1$ the flow is laminar and smooth with no vorticity. For large Reynolds numbers $Re \gg 1$ the flow is chaotic and turbulent.

In superfluids, quantum vortices produce quantum turbulence. Every vortex is fixed in size and so the turbulence is a tangle of vortex lines that are constantly reconnecting with each other. The large scale motion of the superfluid replicates that of classical turbulence. In this thesis we will perform experiments in two regimes of quantum turbulence.

The first regime is semi-classical quantum turbulence found in He-II roughly above 1 K[10, 43, 44]. Thermal excitations can interact with the quantum vortex cores creating a mutual friction force between the superfluid and normal fluid. This force couples the superfluid and normal fluid velocities, so that turbulence in the superfluid creates turbulence in the normal fluid as well[45].

The second regime is pure quantum turbulence at the lowest temperatures[17, 43, 44]. The absence of any appreciable normal fluid allows for a quantum vortex tangle with only the superfluid in motion. This can offer physicists a conceptually simpler system to study compared to classically turbulent systems. The energy cascade here is mediated by Kelvin waves that are helical displacements of the vortex line[46]. As the vortices move they are incident on other vortices and they reconnect with each other creating Kelvin waves along their length[47]. These waves interact with one another and create high frequency Kelvin waves that eventually decay into phonons[48, 49].

2.2 Helium 3

Helium-3 is the much rarer stable isotope of helium. Helium-4 occurs naturally in oil fields from the radioactive decay of elements in the Earth's crust, but this leaves only trace amounts of ^3He . Helium-3 in use today has been synthesised as a by-product of

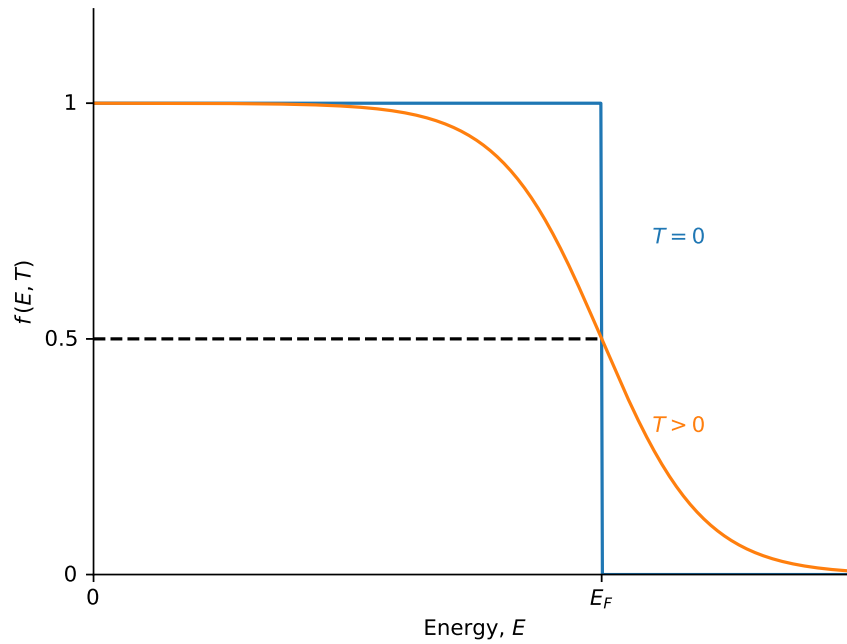


FIGURE 2.5: Fermi Dirac distribution for a gas of fermions at $T = 0$ (blue line) and $T > 0$ (orange line) from eq. (2.24).

nuclear weapons and some nuclear reactors. Despite this it is widely used in dilution refrigerators around the world to achieve milli-kelvin temperatures. Like ^4He it also becomes a superfluid at very low temperatures.

2.2.1 Fermi Liquids

Unlike ^4He , which is a boson, ^3He is a fermion with half integer spin. It explicitly cannot undergo Bose-Einstein condensation because Fermi's exclusion principle forbids any two fermions existing in the same state. Particles in a Fermi gas at absolute zero will instead fill out every state from the ground state to the Fermi-energy E_F [4]. Any thermal energy will lift some particles above the Fermi energy leaving holes below. The distribution for any temperature and energy is described by the Fermi-Dirac distribution[4]:

$$f(E, T) = \frac{1}{e^{(E-E_F)/k_b T} + 1}. \quad (2.24)$$

Figure 2.5 shows graphically eq. (2.24) at absolute zero and a finite temperature.

We should note that eq. (2.24) describes a non-interacting gas of fermions, not a liquid. Liquid ^3He has strong inter-particle forces that attract the atoms towards each other. A moving atom feels the pull of other atoms around itself, increasing the force required to move it. As Landau first described, this can be effectively modelled as an increase of mass. Taking the atom as a quasiparticle with an effective mass higher than the atomic mass, we can then neglect the forces of other atoms vastly simplifying the problem.

Taking all excitations as quasiparticles, we can model them as a weakly interacting Fermi gas[4]. The interaction force is described fully in Landau's Fermi liquid theory by an infinite set of Landau parameters, of which only the first few are needed for acceptable accuracy. They can be found from experimentally measurable values of ^3He (heat capacity, speed of sound, etc).

Landau's Fermi liquid theory preserves the dependencies of properties from Fermi gas to a Fermi Liquid. In a Fermi gas, for example, we see that viscosity is dependent on the mean collision time of the particles[4]:

$$\eta = \frac{1}{3}\rho\tau v_F^2 \quad (2.25)$$

where τ is the mean collision time. This itself is proportional to the inverse square of the temperature[4]. So we know the viscosity of the Fermi liquid will be proportional to T^{-2} which has been confirmed by experimental observations of ^3He [50].

Properties of the fluid then differ from that for an ideal Fermi gas by a modification provided in Landau's theory. For example the speed of first sound c in a Fermi gas is given by[4]:

$$c^2 = \frac{v_F^2}{3} \quad (2.26)$$

While in a Fermi liquid it is modified by the addition of a second term[4]:

$$c^2 = \frac{v_F^2}{3} \frac{1 + F_0}{1 + \frac{1}{3}F_1} \quad (2.27)$$

where F_0 and F_1 are the first two Landau parameters.

2.2.2 Collective Modes

Due to the fermionic nature of ^3He it can support modes that have no analogue in bosonic ^4He . Firstly the half-integer spin causes spin interactions between atoms and their neighbours. In a magnetic field the spins of ^3He atoms will preferentially line up with the field. A disturbance, such as a short magnetic pulse, can cause spin waves to propagate as the precessions of particles effect their neighbours, causing a

precession of spins along the atoms. The spin wave's precession frequency is known as the Larmor frequency f_L found from:

$$f_L = \frac{\gamma B}{2\pi} \quad (2.28)$$

where γ is the gyromagnetic ratio of ^3He , which is the ratio between the magnetic moment and angular momentum of the atomic nucleus, and B the external field. Usually spin waves do not have a energy gap in ^3He , but the presence of a magnetic field creates an energy gap in certain modes.

Like all liquids ^3He can propagate sound waves. However, typically, as the collision time increases (as we lower the temperature) compared to the sound wave oscillation period, the propagation of sound becomes harder. Consider for example a high temperature liquid compared to a dilute gas at a similar temperature; sound in the gas cannot propagate as the particles in the gas do not collide often enough, and the opposite is the case in the liquid. Uniquely for Fermi liquids even as the temperature falls and the collision time increases sound still propagates, as predicted by Landau[51]. We call this sound mode *zereth sound*. Interactions with the full surroundings and Fermi-sphere provide the necessary restoring force for sound density fluctuations allowing the sound wave to propagate despite a lack of collisions. The crossover from normal first sound comes when the quasiparticle collision time is equal to the sound wave period T [4], i.e. when:

$$\omega\tau = 1, \quad (2.29)$$

where $\omega = 2\pi/T$.

2.2.3 Superfluid Helium-3

Despite its fermionic nature ^3He was expected to have superfluid properties at low temperatures in an analogous mechanism to superconductivity of electrons in certain metals[52, 53]. In the Bardeen, Cooper, and Schrieffer (BCS) theory of superconductivity conduction electrons can pair up to form a boson-like superconducting Cooper pair[54]; the newly formed quasibosons can then become a BEC explaining the superconducting properties of the metal. Likewise in ^3He two atoms can pair together to form a Cooper pair, with a coherence length of about 65 nm at a pressure of 1 bar[4], to form a superfluid. This process is only energetically favourable below the transition temperature.

While superfluid ^3He was predicted, the transition temperature from Fermi-liquid into a superfluid was not known. It was found in 1971 by Lee, Osheroff and Richardson who discovered two phase transitions along the solid liquid curve of

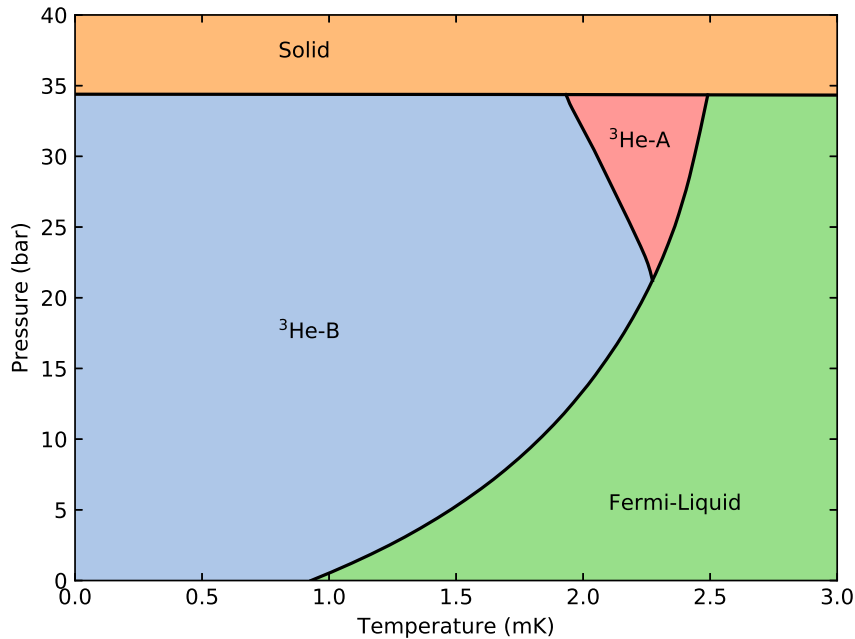


FIGURE 2.6: The phase diagram of bulk ^3He at low temperatures and at zero magnetic field.

helium[55]. They were looking for solid transitions so initially these were mislabelled as solid transitions, but nuclear magnetic resonance experiments later affirmed that these were phase changes in the liquid[56]. Two transitions were discovered and hence two superfluid phases, the A and B phases, had been discovered.

Multiple superfluid phases arise because pairing ^3He atoms is a more complicated process than for electrons. Atoms are not point-like particles and cannot occupy the same space as paired electrons do. Furthermore the magnetic exchange interactions prefer a parallel alignment of spins in the paired quasiparticles. The ground state of the wavefunction therefore has a spin $S = 1$ and orbital angular momentum $L = 1$. Each quantum number has 3 projections on the z axis ($1, 0, -1$) and combining them all shows there is a 3×3 matrix that describes Cooper pairs[4]. Physically speaking this means there are multiple allowed combinations of Cooper pairs.

Having multiple combinations of Cooper pairs means superfluid ^3He has multiple allowed phases as shown in the phase diagram in fig. 2.6. Lee, Osheroff and Richardson discovered two: the A and B phases, which correspond to Cooper pair spin projections $s_z = \pm 1$ and $s_z = \pm 1, 0$ respectively with each projection having an equal population. Adding a magnetic field, as one would intuitively expect, changes the population levels to prefer certain spin projections. The A-B phase boundary

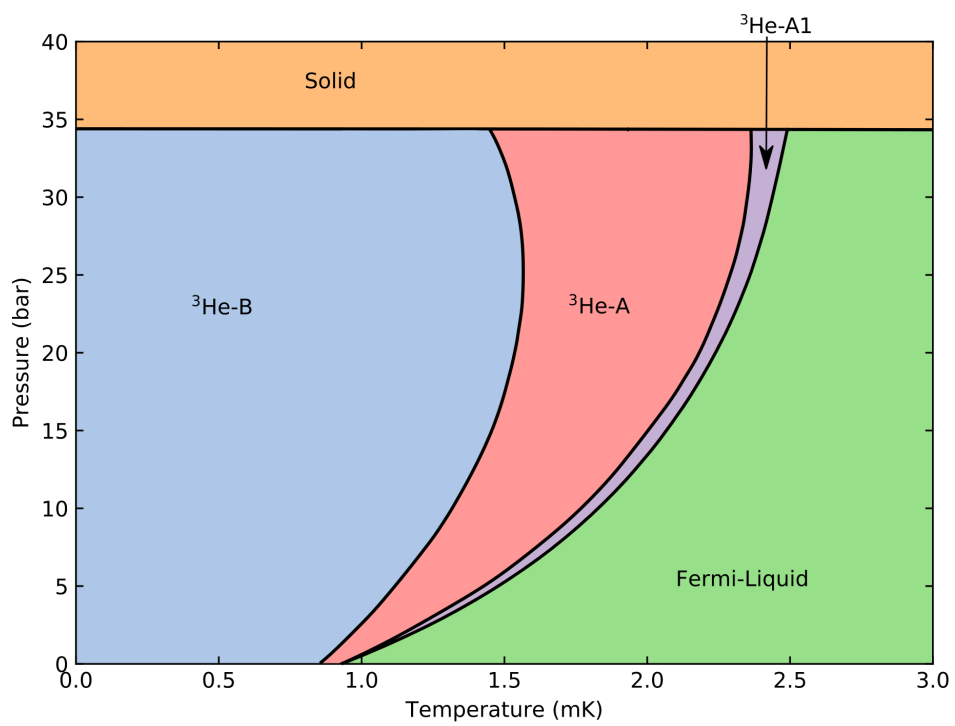


FIGURE 2.7: The phase diagram of bulk ^3He at low temperatures with a small finite field.

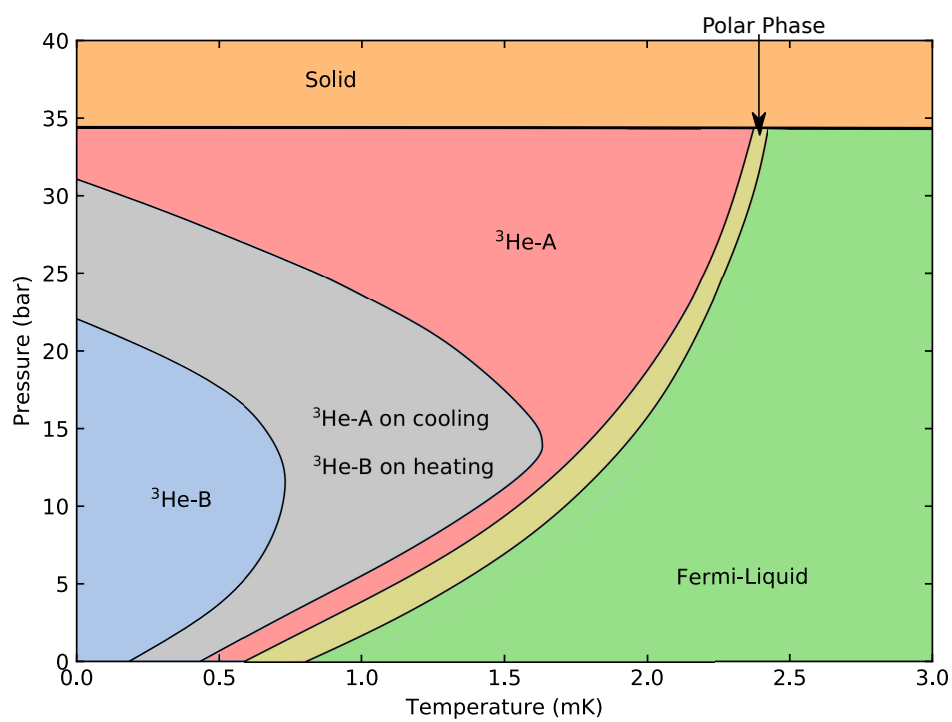


FIGURE 2.8: A sketch of the phase diagram of bulk ^3He at low temperatures under strong confinement from aerogel[57].

shifts to lower temperatures and a third A1 (spin projection $s_z = 1$) phase appears at phase boundary from A to Fermi-liquid.

Similarly to adding a magnetic field we can alter the population levels of Cooper pairs via the orbital angular momentum by the presence of walls. As a simplistic picture we can see that a Cooper pair with angular momentum parallel to a wall should be suppressed as the pair would be incident on the wall. While a Cooper pair with angular momentum perpendicular to the wall would not be suppressed. Walls therefore have the effect of fixing the direction of L , in an effect known as a texture. Extreme conditions are found in parallel strands of aerogel (known as nafen) placed tens of nm apart which leads to extreme confinement in the x-y plane and a fourth phase known as the polar phase[57] as we see in fig. 2.8. Further phases are expected to be found as the level of confinement increases.

2.2.4 Quasiparticle Excitations

We know that the Cooper pairs in the fluid must have a lower binding energy than the energy of two single particles, else the condensate would never form. This leads to an energy gap Δ between the Cooper pairs and single quasiparticle states. The gap is a function of temperature and in $^3\text{He-B}$ it is quasi-isotropic. As the temperature approaches absolute zero the gap tends to the the following limit[58]:

$$\Delta(T \rightarrow 0) = 1.76T_c k_B \quad (2.30)$$

where T_c is the critical temperature to form the superfluid. To then break a Cooper pair we require $2\Delta(T)$ that can split the Cooper pair into a quasiparticle and a quasihole.

Thermally excited quasiparticles in the superfluid can initially be considered as a gas because there is sufficient population that collisions are frequent. Eventually below about $0.3T_c$, where the mean free path of the quasiparticles becomes longer than the dimensions of the experimental cell, (towards $T = 100 \mu\text{K}$ the mean free path is measurable in kilometers)[22], quasiparticle-quasiparticle scattering events become exceedingly rare and we have to neglect the gas model and enter the ballistic regime. All of the measurements in $^3\text{He-B}$ described later were performed in the ballistic regime.

The energy gap changes the dispersion curve for these quasiparticles compared to normal fluid ^3He . The energy gap is above and below the Fermi energy and causes an increase in the density of states about the gap. This raises the excitation curve minima compared to a Fermi gas resulting in the dispersion curve shown in fig. 2.9.

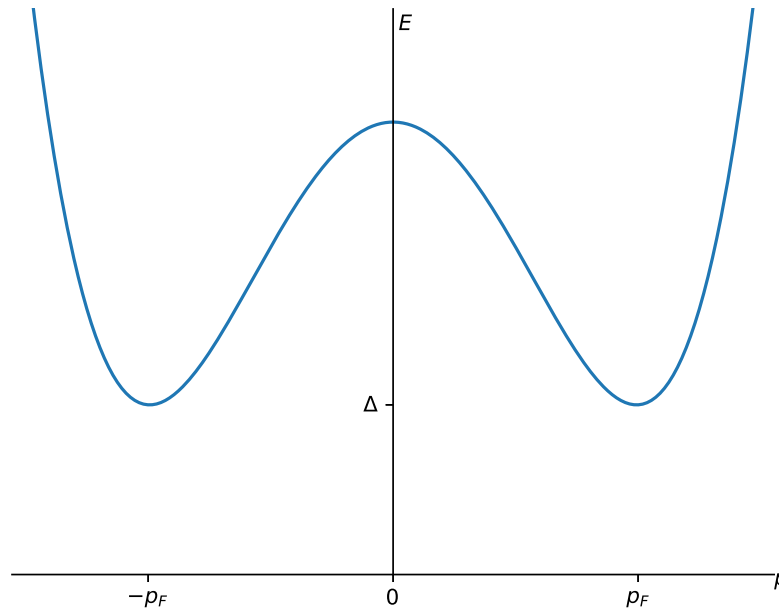


FIGURE 2.9: The dispersion curves for superfluid ^3He . Not to scale.

2.2.5 Quantum Vortices and Quantum Turbulence

Vortices in superfluid $^3\text{He-B}$ arise in a similar manner to vortices described in ^4He . However the large size of the vortices and the wavefunction allows multiple different types of vortex, of which in $^3\text{He-B}$ there are two. At higher pressures and temperatures these are axisymmetric and are fairly similar to ^4He vortices. At low temperatures and pressures vortices are non-axisymmetric with 2 cores. Each core carries a half quantum circulation and the phase change of π . An extra π rotation is required to satisfy earlier arguments and it is found in the spin direction which also rotates by π about the core. The second core then completes the rotations with a further rotation of π about both spin and phase. Half quantum vortices have recently been experimentally confirmed to exist in the polar phase[59] and the A and B phases under strong confinement[60].

The Landau velocity of ^3He is much lower than ^4He so that we can see it macroscopically with oscillatory devices. Experiments with oscillatory vibrating wire have show that Landau's velocity is about 27 mm s^{-1} above which Cooper pairs are broken in the fluid[61, 62].

Using eq. (2.18) we can find the quantum of circulation about the whole vortex structure is given by:

$$\kappa = \frac{h}{2m_3} \quad (2.31)$$

where $2m_3$ is the mass of a Cooper pair. Using Landau's velocity and eq. (2.19) the size of the vortex can be predicted to be about 390 nm. Again this large size is expected due to increased size of the Cooper pairs compared to ^4He atoms.

Similarly to ^4He superfluid $^3\text{He-B}$ supports quantum turbulence[15], which at the ultra low temperatures we use forms the so called pure quantum turbulence discussed in section 2.1.3.

Chapter 3

Mechanical Oscillators

In this work we will use vibrating wire and quartz tuning fork mechanical oscillators as tools to explore helium physics. The small mass of wires makes them highly sensitive to changes in the viscosity in helium and so they are ideal temperature probes[63, 64]. Forks are more massive but typically have a high quality factor and are sensitive devices in their own right. Both wires and forks have been used as probes of viscosity[65, 66], temperature[66] and quantum turbulence in helium[10–15, 67, 68].

The devices we use to probe helium have characteristic length scales from about 75 μm to 0.9 μm . More recent developments have moved towards shrinking the characteristic size of the oscillator to make micro and nano-electromechanical (MEMS and NEMS) oscillators, which are able to probe helium liquids on novel scales approaching the size of a quantum vortex core and the superfluid coherence length[26, 69–72].

In this chapter we shall discuss the basics of oscillator mechanics and consider the details relevant for vibrating wire loops and quartz tuning forks used in this thesis. Lastly we shall explore the effects of hydrodynamic and ballistic damping on oscillators in helium liquids.

3.1 Oscillator Basics

The dynamics of any linear oscillator can be described by the equations for simple harmonic oscillation derived from Hooke's law[73]. A oscillatory driving force $Fe^{i\omega t}$ at a frequency ω accelerates an object, opposed by a restoring force and a damping force proportional to the velocity.

$$m_{\text{eff}} \frac{d^2x}{dt^2} + \gamma m_{\text{eff}} \frac{dx}{dt} + kx = Fe^{i\omega t} \quad (3.1)$$

where m_{eff} is the effective mass of the oscillator, γ the damping constant, and k the spring constant.

The effective mass of the oscillator is the mass of the object in vacuum plus any contributions from fluids viscously clamped to the oscillator's surface (discussed in section 3.3.1). The damping constant γ has real and imaginary components γ_2 and γ_1 respectively that describe dissipative forces and drag from fluid backflow around the oscillator respectively. The spring constant k can be decomposed to:

$$k = m_{\text{eff}}\omega_0^2, \quad (3.2)$$

where the constant ω_0 is the natural resonant frequency of the oscillator in the absence of damping from the fluid.

When solving eq. (3.1) for the velocity amplitude v it is found that:

$$v(\omega) = \frac{F}{m_{\text{eff}}} \frac{\gamma_2\omega^2 + i\omega(\omega_0^2 - \omega^2 - \gamma_1\omega)}{(\omega_0^2 - \omega^2 - \gamma_1\omega)^2 + \gamma_2^2\omega^2}. \quad (3.3)$$

The equation describes a Lorentzian resonance peak with in phase and out of phase (or quadrature) components in the real and imaginary components of the equation respectively and is drawn in fig. 3.1.

At resonance, the in-phase component is at a maximum and the peak velocity of the oscillator v_{max} is given by:

$$v_{\text{max}} = \frac{F}{m_{\text{eff}}\gamma_2}. \quad (3.4)$$

The central frequency of the resonance peak can then be found by solving:

$$\omega_0^2 - \omega^2 - \gamma_1\omega = 0 \quad (3.5)$$

to give a resonant frequency of $\omega = \omega'_0$. The physical meaning is that the damping felt by the wire shifts the resonant frequency of the wire to ω'_0 . Provided the damping is small compared to the resonant frequency, which is generally true for our oscillators, the shift is given by:

$$\Delta\omega_1 = \omega'_0 - \omega_0 = -\frac{\gamma_1}{2}. \quad (3.6)$$

The out of phase component has its maximal or minimal value at half the height of the resonant peak at a frequency $\omega_{1/2}$. Looking at eq. (3.3) this will be found where:

$$\omega_0^2 - \omega_{1/2}^2 - \gamma_1\omega_{1/2} = \omega_{1/2}^2\gamma_2^2 \quad (3.7)$$

We need to additionally assume that $\gamma_2 \ll \omega'_0$, which is generally true in this work, and observe that:

$$\omega_0 - \omega_{1/2} \simeq \frac{\gamma_1 \pm \gamma_2}{2} \quad (3.8)$$

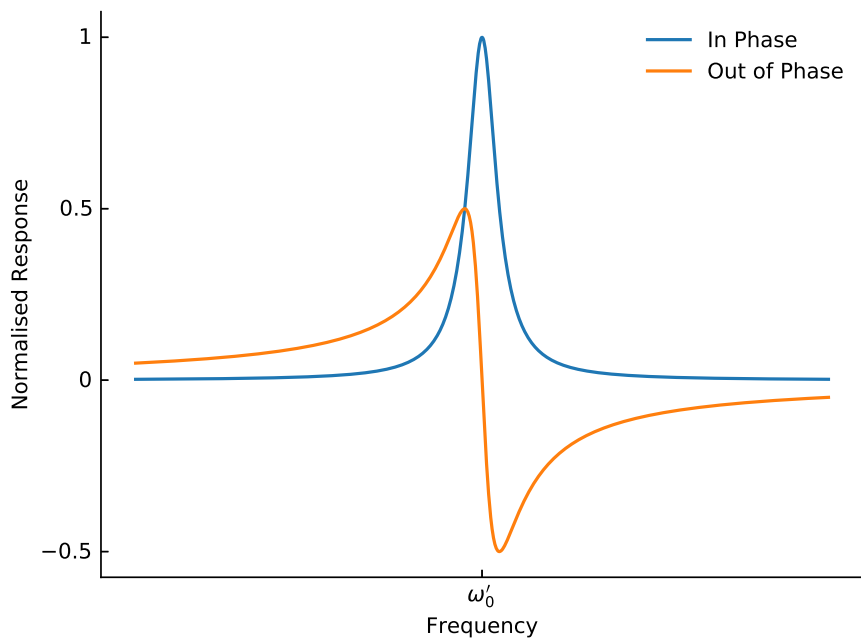


FIGURE 3.1: The in phase (blue) and out of phase (orange) components of an oscillator's resonance. The width of the resonance is the frequency difference between the maximal and minimal values of the out-of-phase (or quadrature) component.

The difference between the two solutions then allows us to find the full width at half maximum, also known as the width, of the resonance:

$$\Delta\omega_2 = \gamma_2. \quad (3.9)$$

Therefore the width is directly related to the damping experienced by the oscillator.

It is worth mentioning here the height times width over drive (HWD) value which we can see by rearranging eq. (3.4) and using eq. (3.9):

$$\frac{1}{m_{\text{eff}}} = \frac{v_{\text{max}}\Delta\omega_2}{F}. \quad (3.10)$$

We can see that the value is related to the effective mass alone. Since the mass of an oscillator is a constant this means the HWD is similarly a constant that can be found directly from fitting a Lorentzian to the oscillator's frequency response. As we will see below this usefully allows us to find one value of the constituent parts from the other two (drive from the height and width for example).

3.1.1 Vibrating Wire Loop

Vibrating wire loops have long been used by researchers to make measurements in helium liquids. They consist of a loop of superconducting NbTi wire or tantalum wire with two legs glued to a stycast paper base. Superconducting wire is used to prevent any Ohmic heating during low temperature measurements. A former is used to shape the wire to the desired shape, here we will discuss the commonly used semicircular wires which are used in this thesis, but rectangular 'goalpost' wires have been used elsewhere[74, 75]. A dedicated solenoid or the demagnetisation field itself provides the magnetic field necessary to drive the wire.

Vibrating wire loops are very sensitive when finely calibrated and are used for thermometry in normal fluid ^3He [63], $^3\text{He}/^4\text{He}$ mixtures[64] and superfluid ^3He -B[64]. A wire was used in the initial discovery of the quantisation of circulation in superfluid ^4He [39] and they have been used to investigate turbulence in both ^4He and ^3He [15, 67, 68].

Figure 3.2 shows a pictorial schematic of a vibrating wire. In a magnetic field B the wire loop feels a Lorentz force F if a current I passes through the wire. For a wire with a leg spacing of diameter l :

$$F = IBl. \quad (3.11)$$

The force on the wire creates motion and for an oscillatory current the wire's velocity v is also oscillatory. The motion causes a changing magnetic flux $\phi_B = \mathbf{B} \cdot \mathbf{A}$ in the magnetic field where \mathbf{A} is vector area bounded by the wire. This creates an

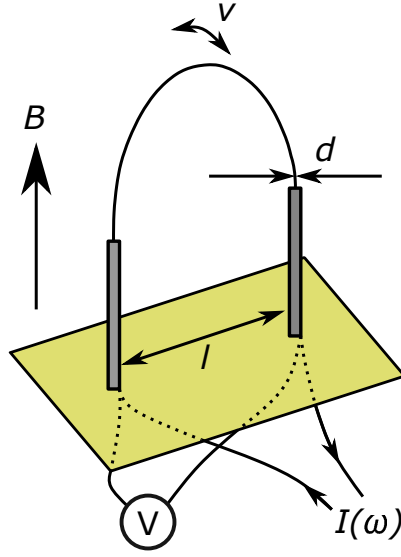


FIGURE 3.2: A schematic of a vibrating wire used in this thesis. An ac signal causes periodic motion in the wire with a magnetic field that creates detectable emf (see text).

electromotive-force V due to Faraday's law:

$$V = -\frac{d\phi_B}{dt}. \quad (3.12)$$

The area with respect to the magnetic field changes as the wire's position changes. The instantaneous change in the flux (assuming a constant field) is then proportional to the change in the cross-sectional area.

$$V = -B\frac{dA}{dt} \quad (3.13)$$

The area is given by the leg spacing multiplied by the wire's displacement x :

$$A = clx, \quad (3.14)$$

where c is a geometric factor for the wire. The change in the area comes from the change in the position, that is naturally given by the velocity v . For a semi-circular wire the maximum voltage V_0 is proportional to the velocity, that must also be at a maximum v_0 :

$$V_0 = \frac{\pi}{4}Blv_0. \quad (3.15)$$

Where $\pi/4$ is the aforementioned geometric factor.

The characteristic size of the wire is given by the diameter of the wire used to

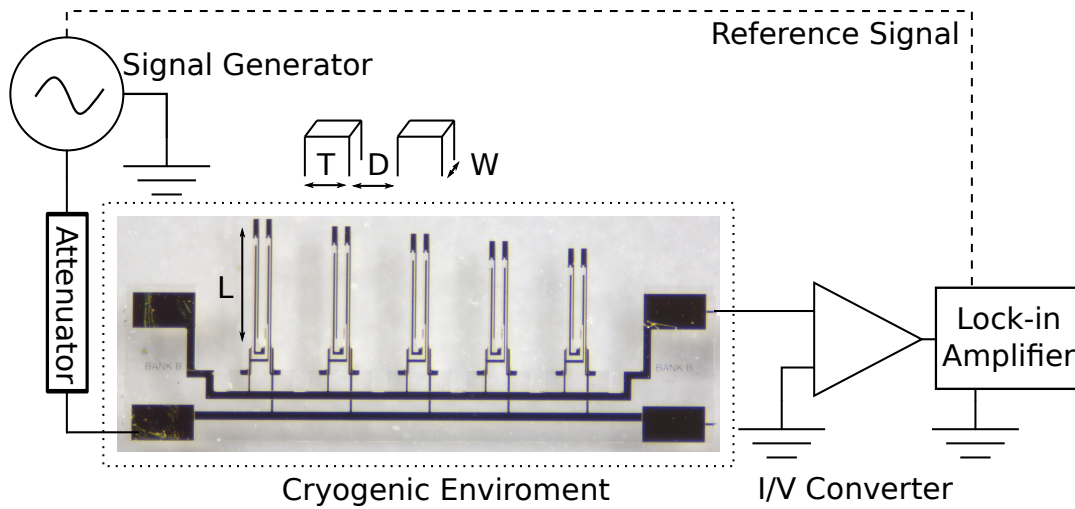


FIGURE 3.3: A photographic schematic of a quartz tuning fork array and the measurement setup. The fork's length L , width W , tine separation D and thickness T are also highlighted. An Agilent 33521A signal generator was used to excite the forks while a SR830 or SR844 lock-in amplifier was used to measure the response at the fundamental or overtone resonances respectively.

make the vibrating loop d and is what mainly controls the sensitivity of the wire. We use several different wire sizes of diameters ranging from $0.9\ \mu\text{m}$ to $120\ \mu\text{m}$, the thinnest being the most sensitive. The leg spacing also varies from $2.5\ \text{mm}$ to $3.2\ \text{mm}$.

3.1.2 Tuning Forks

Piezoelectric quartz tuning forks have been used for decades as the timepieces in digital watches, chosen for their high intrinsic quality factor, low cost and ease of mounting; these properties also made them of interest to researchers. They were first used for atomic force microscopy measurements[76–78] and then for quantum fluids research, originally used as viscometers[65, 66] and thermometers[66] and later were used to study quantum turbulence[10–14].

Figure 3.3 shows a picture of some the forks used in this thesis, and fig. 3.4 shows a scanning electron microscope close-up image of a single fork. They were all custom manufactured on a wafer as either single forks or arrays of 5 forks of different lengths but the same thickness¹. This allows a wide range of carefully selected resonant frequencies to avoid cross-talk between forks. After separation from the wafer two thin copper wires were soldered to the two contact pads for the array or single fork. A small amount of araldite glue was then used to strengthen the join between the

¹Manufactured by the Statek Corporation, 512 N. Main Street, Orange, CA 92868, USA

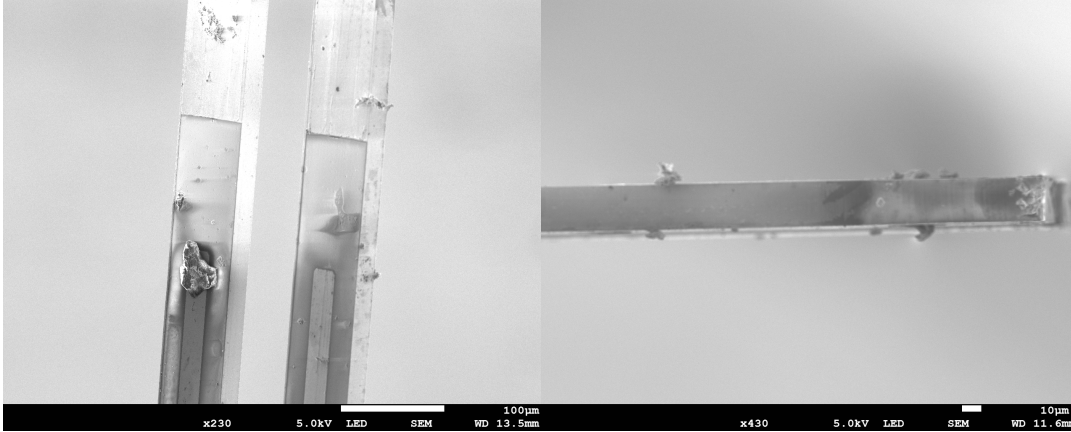


FIGURE 3.4: Scanning electron microscope images of one of the forks. Note dirt attached to the fork that can be cleaned off with acetone.

wire and tuning fork. From here the forks were then mounted in the experimental cell.

A potential difference applied on one of the wires creates an electric field from the electrodes along one of the prongs. The field polarizes atoms in the quartz crystal and causes lattice deformation and the prongs are displaced. An ac signal causes periodic motion in the prongs; the changing deformation creates a piezoelectric current that can then be measured. This current I is proportional to the velocity v of the prong:

$$I = av \quad (3.16)$$

where a is the fork constant unique to each fork. Likewise the force F felt by the prong due to an applied voltage V is:

$$F = \frac{1}{2}aV. \quad (3.17)$$

Each prong has a length L , width W , thickness T and is separated from the other prong by a separation D and are shown schematically in fig. 3.3. A fork has an effective mass m_{eff} equal to[25]:

$$m_{\text{eff}} = \frac{1}{4}\rho_q WTL \quad (3.18)$$

where ρ_q is the fork material (quartz) density equal to 2659 kg m^{-3} . Recalling equation 3.4 and substituting equations 3.16 and 3.17 allows us then find the fork constant a :

$$a = \sqrt{\frac{4\pi m_{\text{eff}} \Delta f_2 I_{\text{max}}}{V}} \quad (3.19)$$

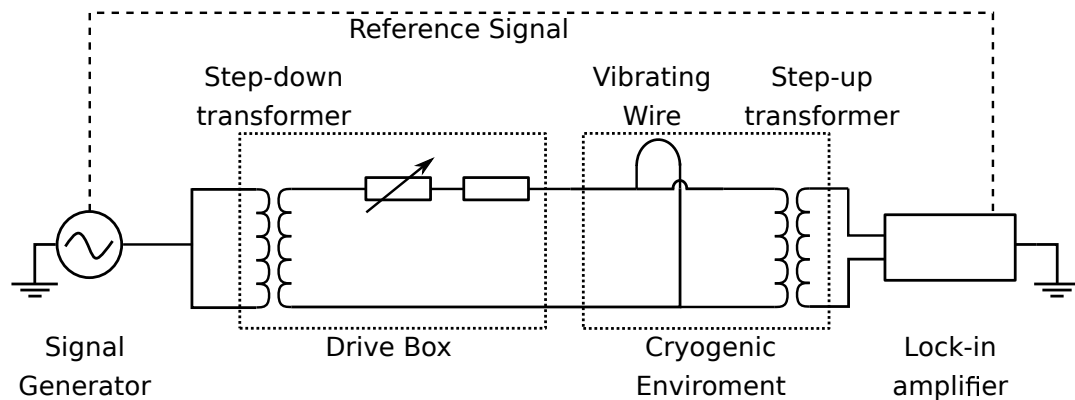


FIGURE 3.5: Schematic of the circuit used to measure the vibrating wires. An Agilent 33220A or 33521A signal generator was used to excite the wire while a SR830 lock-in amplifier was used to measure the response.

where I_{\max} is the current response at resonance. Since I and V are experimentally known, or measurable, all one needs to know to find the fork constant is the fork dimension and material, giving the velocity and force on the fork. Optical measurements have found that using the fork constant a to derive the velocity agrees with the actual prong tip velocity to within about 10%[\[79\]](#).

As well as the fundamental mode it is possible to excite forks at the first overtone mode. The frequency of this mode can be found via Euler-Bernoulli beam theory to be at a frequency approximately 6.3 times the fundamental resonance frequency[\[25\]](#). The mode has its own fork constant that allows the velocity to be calculated from the same equations above. Higher modes also exist but in the measurements here they were not measured.

3.2 Operation and Measurement

The basic measurement of any oscillator uses a signal generator paired with a lock-in amplifier. The signal generator provides an ac signal at a specified amplitude and frequency and a reference signal to the lock-in amplifier. The lock-in amplifier can then measure the in-phase and out-of-phase response of its input signal at the signal generator's frequency and at a constant phase. Both sets of measurements are typically performed at the root mean square amplitude and must be converted in analysis to find the true peak velocity of the oscillator.

Figure [3.5](#) shows the measurement circuit used to perform the four point measurement of the vibrating wire. The drive box is custom-made in house and contains a switch to select one of a series of resistors to vary the current and a step down

transformer (6:1) which further reduces the signal. The transformer has the additional advantage of breaking ground loops, reducing heating. The signal then goes to the wire and the response is stepped up by another transformer (typically 30:1, 100:1 or 1:1). A lock-in amplifier can then measure the wire's response compared to a reference frequency from the signal generator.

Figure 3.3 shows the setup for measuring a quartz tuning fork. Forks can be driven directly by the signal generator, but the input signal is usually attenuated to avoid over-driving the fork. The fork's response is tiny (of order 1 nA) so a custom-made voltage current converter (or trans-impedance amplifier) amplifies the signal by 100 kV/A or 1 MV/A[80]. The signal can then be measured by a lock-in amplifier.

3.2.1 Frequency Sweep

Frequency sweeps provide the greatest amount of information about an oscillator. The response of the oscillator at a single frequency is measured; this process is then repeated 60 to 300 times at successive frequencies. The responses trace out the Lorentzian curve described by eq. (3.3) as long as the resonance is within the range of the sweep.

A slight modification to eq. (3.3) is needed to account for the background signal. Stray capacitance and inductive couplings in the wiring and the device itself shift the in-phase and out-of-phase components away from each other. This necessitates measurement of the separate in-phase and out-of-phase components (not the modulus and phase commonly used elsewhere) and also the adding of a polynomial background term to the fitting Lorentzian to account for the effect. In this work, the polynomial was linear or a constant in both the in-phase and out-of-phase components.

The time taken to measure each point should be longer than the response time τ of the oscillator to avoid ringing effects:

$$\tau = \frac{2}{\Delta\omega_2}. \quad (3.20)$$

Successive measurements are preferably taken after 2τ where ringing effects have largely subsided. When the device is heavily damped we usually take 1 s to measure a point but at lower damping the measurement time should be increased to prevent ringing. If the device has only minimal damping, frequency sweeps, if done properly, can take hours, so other techniques can be pursued or compromises taken with ringing.

3.2.2 Amplitude Sweep

While staying on the resonant frequency of the oscillator, the drive is increased and the response recorded. We can stay on resonance by minimising the ratio of the in-phase component to the out-of-phase component to within a certain tolerance value ($<1\%$). If the ratio exceeds 1% the tolerance value is not passed and the program shifts the frequency and then retakes the measurement, and possibly repeats the step until the resonance is found.

In order to track the resonance, the aforementioned background signal must be known for each successive drive or the ratio will be incorrect. This is found by performing an amplitude sweep at fixed frequencies above and below resonance and far from it (at least 10 times the width away from the central resonance). Combining the two sweeps and taking the average allows us to find the background polynomial as function of drive at the resonance.

Each successive point should again allow a sufficient time for measurement to allow ringing effects to subside. An advantage of taking the down sweep is that it will have substantially different values to the up sweep if an insufficient measurement time is chosen. The sweep can then be retaken with a larger measurement time per point.

3.2.3 Resonance Tracking

When the properties of the fluid change quickly, frequency sweeps can be too slow to see any changes. We then use resonance tracking to measure the parameters of the oscillator at a rate of around one measurement per second, though this can be changed if even faster tracking is required. In a similar manner to the amplitude sweep, we track the resonance of the oscillator and measure the height of the resonance. By using the previously determined HWD, the width of the oscillator can be inferred from the height measurement and applied drive. Typically the drive will be adjusted to keep the height constant. Similarly to amplitude sweeps accurate knowledge of the background signal is needed and is found by the same method.

The fast nature of the tracking means the ringing effects for near instantaneous events do affect the resonator, especially at ultra low temperatures where resonator widths are typically <1 Hz. This manifests itself in the data by the width curving exponentially to the final value.

3.3 Damping in Helium Liquids

In a vacuum the only damping effects on an oscillator are the intrinsic effects of the material that it is made of. In a fluid the damping will increase as the oscillator

displaces fluid and feels the viscous drag of the fluid about it when moving[81]. In this section the effects of fluid damping will be discussed in reference to both normal and superfluid ^4He and ^3He . In the ultra low temperature regime fluid effects become insignificant and the effects of ballistic quasi-particles will dominate the damping.

3.3.1 Hydrodynamic Regime

A normal fluid has a non-zero viscosity that clamps a layer of fluid to any surface in the fluid. This layer will be dragged along a moving surface such as a mechanical oscillator in the fluid. This effectively adds an extra mass to the oscillator from the fluid dragged along. We can describe the layer thickness with the viscous penetration depth δ in terms of the fluid viscosity η , normal fluid density ρ_{nf} and oscillation frequency f :

$$\delta = \sqrt{\frac{\eta}{\pi f \rho_{\text{nf}}}}. \quad (3.21)$$

Using the normal fluid density and the oscillator surface area S and a geometrical factor B for the oscillator's shape, the added mass from viscous clamping will be $B\rho_{\text{nf}}S\delta$.

Fluid backflow around the oscillator will also add a contribution to the effective mass of the oscillator, which is described by the fluid mass displaced by the oscillator volume V and the whole fluid density ρ_H as $\beta\rho_H V$; note an extra geometric factor β that describes the shape of the oscillator.

The enhanced mass m of the oscillator in the liquid is sum of the vacuum effective mass m_{vac} and hydrodynamic contributions \tilde{m} :

$$m = m_{\text{vac}} + \tilde{m} = m_{\text{vac}} + \beta\rho_H V + B\rho_{\text{nf}}S\delta \quad (3.22)$$

The change in mass of the oscillator will cause the oscillator's resonant frequency to change, the spring constant will remain unchanged so using eq. (3.2) we see the new resonant frequency ω_0 :

$$\omega_0^2 = \omega_{0\text{vac}}^2 \frac{m_{\text{vac}}}{m} \quad (3.23)$$

in terms of the undamped vacuum resonance $\omega_{0\text{vac}}$. From here using eq. (3.22) we can find the new resonance frequency and width[66]:

$$\left(\frac{f_{0\text{vac}}}{f_0}\right)^2 = 1 + \beta\frac{\rho_H}{\rho_m} + B\frac{S}{V\rho_m}\sqrt{\frac{\eta\rho_{\text{nf}}}{\pi f_0}} \quad (3.24)$$

$$\Delta f_2 = \frac{1}{2}\sqrt{\frac{\rho_{\text{nf}}\eta f_0}{\pi}}CS\frac{(f_0/f_{0\text{vac}})^2}{m_{\text{vac}}} \quad (3.25)$$

where ρ_m is the mass density of the oscillator and C is another geometrical factor. β , B and C are naturally different for different types of oscillator, but also account for imperfections from idealised characteristics so they are treated as fitting parameters.

Equation (3.25) also represents the limit of Stokes theory where the viscous penetration depth is much less than characteristic size l , i.e. $l \gg \delta$ [50]. For small devices or high viscosity situations such as in low temperature ^3He this assumption can be broken. In such a case a full Stokes theory calculation can find the precise frequency shift and damping width of a cylinder with reference to the characteristic size of the device and a prefactor that represents the imperfections of the device.

3.3.2 Ballistic Regime

As the temperature of superfluid helium decreases the normal fluid will eventually become essentially non-existent. The remaining thermal excitations form a quasi-particle gas in the liquid interacting with the surroundings. After further cooling in ^3He below $0.3T_c$ the mean free path of the excitations exceeds the dimensions of the experimental cell and the path of the quasiparticles excitations becomes ballistic.

To explore the effects of the quasiparticles on an oscillator let us consider a flat paddle in isotropic superfluid helium. The paddle has an area A and a number density of n quasiparticles in the liquid are moving with an average velocity equal to the mean quasiparticle group velocity v_g and a momentum equal to the Fermi momentum p_F . At rest an equal amount of quasiparticles hit the paddle on both sides. A quasiparticle hitting on its front side exchanges $2p_F$ momentum as it is reflected back into the bulk by the paddle. Roughly half of the quasiparticles (and holes) will hit the front side and so the force on the side is:

$$F_{\text{front}} = Anv_g p_F \quad (3.26)$$

which is exactly the same magnitude as the force on the back side.

If the paddle moves towards the front with velocity v this will change the force on the front to $An(v_g + v)p_F$ and the back to $An(v_g - v)p_F$, so the balance of forces is no longer zero and the paddle will feel a retarding force:

$$F = 2Anvp_F. \quad (3.27)$$

In ^4He these simple arguments work quite well[82]. But in $^3\text{He-B}$ the observed force is three orders of magnitude greater than the prediction.

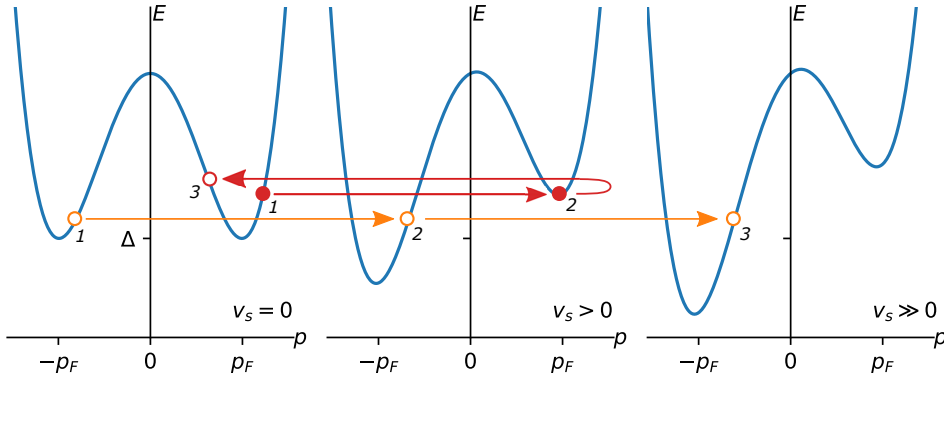


FIGURE 3.6: Andreev's reflection of a quasiparticle in $^3\text{He-B}$. A quasiparticle (red) and hole (orange) approach a velocity field causing a Galilean transformation in the dispersion curve. The quasiparticle at 1 penetrates the velocity field up until 2 where it no longer has an allowed state to travel into, so it is retro-reflected into a hole that travels back to 3. Meanwhile the hole from 1 can travel through the field unimpeded from 1 to 2 to 3.

Andreev Reflection

In $^3\text{He-B}$ the superflow of the liquid about the paddle as it moves interacts with quasiparticles in addition to the paddle. To appreciate this we will look at the quasiparticle dispersion curve of $^3\text{He-B}$ at rest and in motion.

Figure 3.6 shows quasiparticles moving into a superflow. The quasiparticle's relative velocity to the superfluid will increase or decrease shifting its position on the dispersion curve[83]. In the laboratory rest frame we see this as a slant in the dispersion curve. Depending on the quasiparticle's energy there may no longer be an allowed state for the quasiparticle. At which point in order to satisfy conservation of energy and momentum it is retro-reflected as a quasi-hole, in a process known as Andreev reflection. A quasiparticle approaching on the other side of the curve still has allowed states and is thus unimpeded. The process works vice-versa for quasi-hole excitations.

This means that as the paddle's velocity increases holes can hit the paddle increasingly only from the rear while quasiparticles can hit the paddle increasingly from the front only. Both the holes and quasiparticles exchange $-2p_F v$ energy with the paddle. Quasiparticles and holes moving with the opposite momentum are retro-reflected before hitting the paddle and hence the paddle will increasingly feel only a retarding force compared to its motion. This explains the increased damping seen in oscillators compared to ^4He .

Modifying our arguments given before, firstly lets consider the unimpeded quasiparticles and holes able to reach the paddle. Their force will be:

$$F = 2Ap_F \langle nv_g \rangle, \quad (3.28)$$

where $\langle nv_g \rangle$ is the quasiparticle flux. Which can be found by integrating over the allowed quasiparticle states:

$$\langle nv_g \rangle = \int_{\Delta}^{\infty} v_g(E) g(E) f(E) dE, \quad (3.29)$$

where $f(E)$ is Fermi distribution and $g(E)$ is the density of states.

Considering that a fraction of quasiparticles and holes are Andreev reflected, before reaching the paddle, we can not simply use the quasiparticle flux but must integrate over the allowed states. That is the particles with an energy above $\Delta + p_F v$:

$$F = -2Ap_F \int_{\Delta + p_F v}^{\infty} v_g(E) g(E) f(E) dE, \quad (3.30)$$

the Fermi distribution $f(E)$ in the ballistic regime can be approximated by a Boltzmann distribution, and the density of states $g(E)$ in energy space can be combined with the group velocity into the density of states in momentum space $g(p)$. Most quasiparticles and holes will be near one of the minima of the dispersion curve so we can estimate their momentum p as p_F . With these approximations eq. (3.30) becomes:

$$F = -2Ap_F \langle nv_g \rangle \exp\left(\frac{-p_F v}{k_B T}\right). \quad (3.31)$$

The total force on the paddle per unit area is then:

$$\frac{F}{A} = 2p_F \langle nv_g \rangle \left[1 - \exp\left(\frac{-p_F v}{k_B T}\right)\right]. \quad (3.32)$$

Note this force has both velocity and temperature components. A real world subtlety particularly for cylindrical wires is that they do not have a perfectly straight smooth face as assumed above. Quasiparticles hitting this surface will be scattered from surface roughness. In addition the superfluid velocity field about the oscillator is altered by the shape of the device itself. We introduce two dimensionless geometric fitting constants γ and λ to characterise these subtleties:

$$F = 2A\gamma p_F \langle nv_g \rangle \frac{1}{\lambda} \left[1 - \exp\left(\frac{-\lambda p_F v}{k_B T}\right)\right] \quad (3.33)$$

where A is now the surface area of the device. Recalling eq. (3.4) allows us to find the damping effect of ballistic quasiparticles in ^3He on an oscillator in terms of the width.

3.4 Helium-3 Thermometry

Equation (3.33) allows the use of oscillatory devices, such as forks[11] and wires[64], as secondary thermometers in superfluid ^3He in the ballistic regime. This use has the advantages that the temperature of the device does not matter (so there is no need for thermalisation) and that it is directly probing the fluid.

A thermometer is typically never strongly driven, this avoids pair breaking and also the effects of increased Andreev reflection from increased velocity. This allows us to simplify eq. (3.33) by taking a Taylor expansion of the exponential and with eq. (3.4) we find the thermal width Δf_2^T [67]:

$$\Delta f_2^T = \frac{d\gamma'}{\pi m_l} \frac{p_F^2}{k_B T} \langle n v_g \rangle, \quad (3.34)$$

where m_l is the mass per unit length and γ' has absorbed other geometric factors into one constant. Using eqs. (3.30) and (3.34) and we find that:

$$T = \frac{\Delta}{k_B \ln \left(\frac{d\gamma' p_F^2 g(p_F)}{\pi m_l \Delta f_2^T} \right)}. \quad (3.35)$$

The value of γ' is difficult to determine experimentally, because small variation in temperature cause large uncertainties in γ' . However bolometric experiments allow the value of γ' to be inferred to an acceptable accuracy[84]; for a 4.5 μm diameter wire it was found that γ' is 0.28. From here it is possible to then calibrate other devices against a device with a known value of γ' such as has been done with 32 kHz tuning forks[11].

The sensitivity of calibrated devices makes them ideal for use as thermometers in superfluid ^3He . They are limited though by the intrinsic width of the device, as the total measured width is:

$$\Delta f_2 = \Delta f_2^T + \Delta f_2^i. \quad (3.36)$$

As the thermal damping falls the intrinsic damping of the oscillator itself will eventually dominate and the device will lose sensitivity. For wires the intrinsic width can be quite small (about 0.03 Hz) which means even a small thermal width will dominate allowing for thermometry above about 100 μK .

Chapter 4

Refrigeration

In this chapter the methods of cooling the experiments described in this thesis are discussed. This is not a comprehensive review of the methods used but is intended as an introductory discussion of the physics of the methods involved. A full discussion of the actual designs and trade-offs can be found elsewhere[4, 85, 86].

The work in this thesis was performed on two refrigerators. The first was a ^4He immersion cryostat used for measurements in ^4He in chapter 5 and chapter 7. The ^3He - ^4He dilution refrigerator with an adiabatic demagnetisation stage was used for measurements in ^3He in chapters 6 and 7.

4.1 ^4He Cryostat

The cryostat was made out of two dewars. The outer dewar holds an insulating layer of liquid nitrogen at 77 K. While the inner dewar holds the liquid ^4He bath separated from the liquid nitrogen by the dewar's vacuum layer. The nitrogen layer at temperature T significantly reduces the heat radiation E from radiation from area A by Stefan-Boltzmann's law:

$$E = \epsilon\sigma AT^4, \quad (4.1)$$

where ϵ describes the emissivity of the area and σ is a constant. By having an insulating layer at 77 K as opposed to room temperature (~ 300 K) the heat flux is significantly reduced. Furthermore a reflective silvered surface has a low emissivity ($\epsilon \simeq 0.01$) and is used to decrease the radiative heat flow.

Inside the last dewar is the final vacuum and then the main helium bath. The experiment is held by a cryogenic insert directly connected to a room temperature plate. The insert is made of a steel tube (wall thickness about 0.1 mm) which restricts heat conduction. The steel is made of iron with impurities that scatter heat conducting phonons making thermal conduction slower. Along the tube a series of baffles are placed to reflect back radiation incoming from the room temperature plate.

The experiment has a number of measurement wires connected to instruments outside the cryostat. The wires are made of relatively pure copper that has little resistance to phonons. However the wires are so thin (about $50\ \mu\text{m}$) that any heat conduction is insignificant compared to other sources. Electrical ohmic heating is also low due to copper's low resistance. Where superconducting wires are used there is no ohmic heating.

For tuning fork measurements coaxial cables were used which have a larger heat flow. This is an acceptable trade-off since the experiment could still last about 6 hours which was sufficient for measurements.

To cool the experiment evaporative cooling of ^4He is used by pumping on the main bath. By decreasing the pressure of the helium its temperature decreases as it follows the liquid-vapour line shown on the phase diagram in fig. 2.1. The achievable temperature is dependent on how powerful the pump is and total heat leak. In this thesis we found that a rotary pump cooled the ^4He down to about 1.4 K at saturated vapour pressure while a Roots pump can cool further to about 1.2 K at saturated vapour pressure.

4.2 Dilution Refrigeration

Dilution refrigerators were first realised by Das *et al.* in 1965[87] and have since become the workhorse of modern low temperature physics. No other system has been found that can reliably obtain stable milli-kelvin scale temperatures for long periods of time and commercial variants are used in physics labs all over the world to cool down experiments. The work in this thesis was performed on a custom built Lancaster Advanced Dilution Refrigerator[86], and in this section we shall discuss the principles of its operation.

A dilution refrigerator achieves its cooling power by exploiting the phenomenon of phase separation in ^3He and ^4He mixtures[85]. We can see from fig. 4.1 that cooling a mixture of the two isotopes will cause the spontaneous separation of the mixture into two phases, a ^3He concentrated phase and a ^3He dilute phase[85]. This arises due to the inter-atomic attractive force between ^4He atoms being stronger than between ^3He and ^4He atoms.

Figure 4.2 shows a picture of the dilution refrigerator used. We manipulate the system when the two phases are in contact and in equilibrium in the mixing chamber. By removing ^3He atoms from the dilute phase in the still, the system recovers equilibrium by pulling ^3He across the phase boundary from the concentrated phase into the dilute phase. Pulling atoms across incurs an energy penalty and the system cools down, thus providing the cooling power of the refrigerator. The cooling power is proportional to the rate of ^3He flow through the phase boundary, assuming

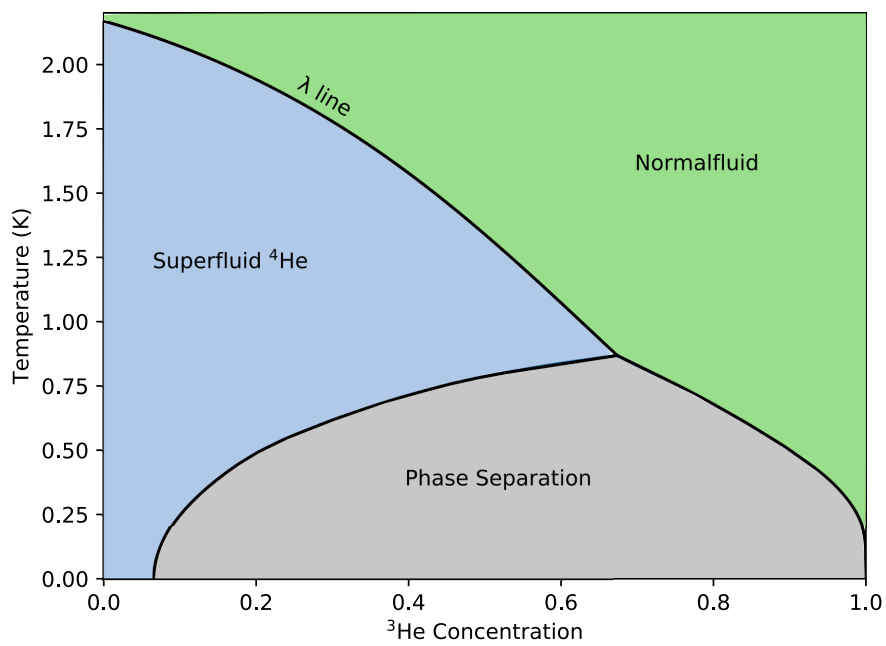


FIGURE 4.1: The phase diagram of a liquid ${}^3\text{He}$ - ${}^4\text{He}$ mixture showing the temperature vs the relative ${}^3\text{He}$ concentration at the saturated vapour pressure. The λ line shows a transition from normal fluid to Fermi liquid ${}^3\text{He}$ in superfluid ${}^4\text{He}$. From 0.87 K to 0 K the mixture phase separates into a ${}^3\text{He}$ rich and ${}^3\text{He}$ dilute phase (see text).

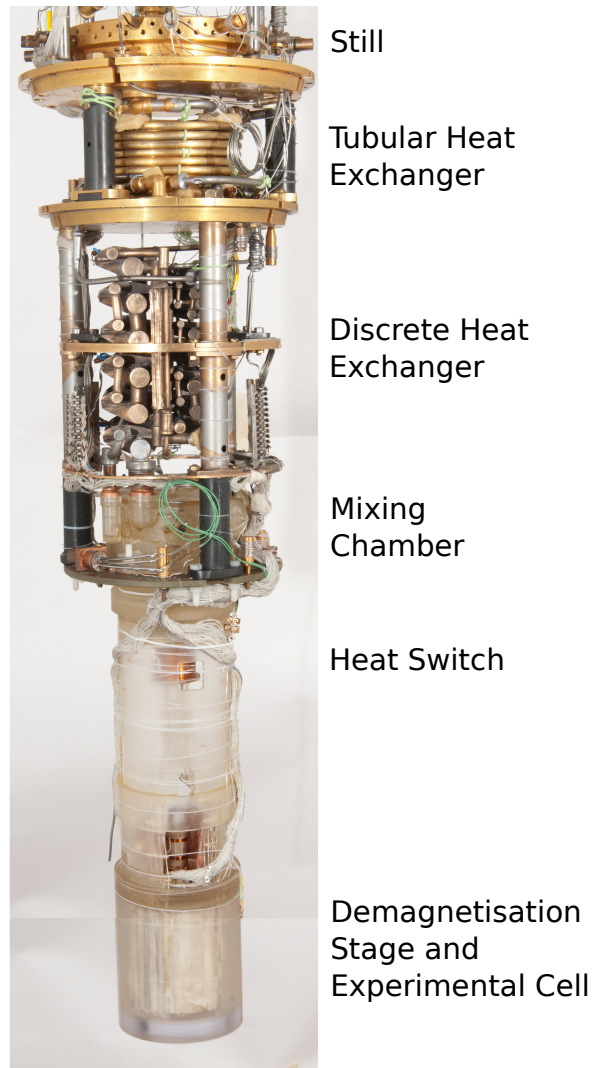


FIGURE 4.2: A photo of the dilution refrigerator and demagnetisation stage of the cryostat. Condensed ^3He is cooled as it flows through the tubular and discrete heat exchangers[86] into the mixing chamber. After crossing the phase boundary it flows back up through the heat exchangers and is evaporated in the still to repeat the cycle. An aluminium heat switch connects the mixing chamber to the demagnetisation stage and experimental cell.

both the dilute and concentrated phase have the same temperature the cooling power \dot{Q} can be derived as[85]:

$$\dot{Q} = 84\dot{n}_3 T^2. \quad (4.2)$$

where \dot{n}_3 is the molar flow rate of ^3He . Heat leaking into the refrigerator raises the base temperature and decreases the available cooling power for experiments.

To make the process continuous ^3He gas is returned and cooled and condensed into a liquid by heat exchangers with the already cooled ^3He rising from the mixing chamber. The cooled ^3He then enters the mixing chamber into the ^3He concentrated phase. Here the ^3He is pulled across into the dilute phase, cooling the mixing chamber down. After the ^3He is pulled across into the dilute phase it rises through heat exchangers into the still and is evaporated. The ^3He is actively pulled around the system by external pumps that make the process continuous.

The overall cryostat has a liquid nitrogen bath and a liquid ^4He bath at 4.2 K separated from the surroundings and each other by vacuum spaces. Inside the helium bath there is the inner vacuum chamber that holds the dilution unit and later stages. A '1 K pot' in the inner vacuum contains superfluid ^4He pumped down to about 1 K that starts the cooling of ^3He gas entering the refrigerator, the pot is continuously filled from the main ^4He bath.

With the experimental cell attached the lowest temperature achievable is about 4 mK to 5 mK. It takes the dilution refrigerator about 2 weeks to cool the experiment to this temperature. We require still lower temperatures for superfluid $^3\text{He-B}$ so a nuclear demagnetisation stage is staged below the mixing chamber to provide further cooling.

4.3 Adiabatic Nuclear Demagnetisation Refrigeration

At the bottom of the vacuum chamber in fig. 4.2 connected via an aluminium superconducting heat switch[85] to the mixing chamber is the experimental cell and coolant material. Adiabatic demagnetisation of a magnetic material can cause cooling in the material and systems in thermal contact with it. Here we discuss the use of this process to cool ^3He .

The coolant material used is copper which has the advantages of being readily available and having a low internal magnetic field, which if too high would limit the achievable temperature. Copper has a spin 3/2 nucleus and as fig. 4.3 shows, in the presence of a magnetic field, the nuclear energy levels split into four levels via Zeeman splitting[85]. At high temperatures the energy levels will be equally populated. As we decrease the temperature however, as fig. 4.3 illustrates, the lowest energy level will be energetically favourable and hold a high population of atoms.

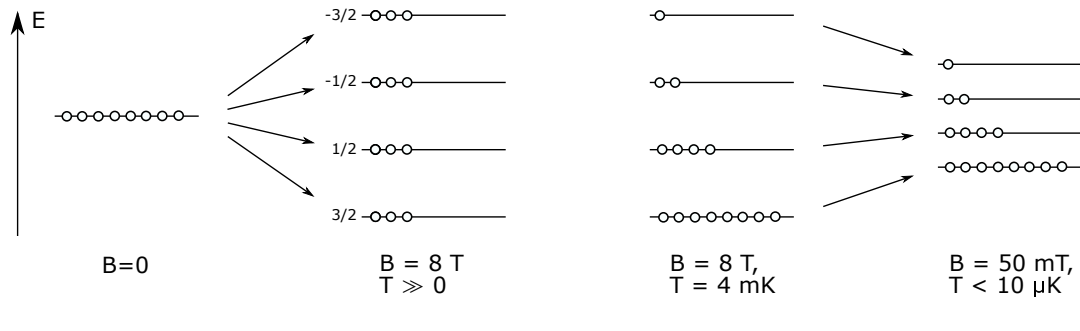


FIGURE 4.3: A simplified schematic of the nuclear energy levels of copper without a magnetic field, with a high field at high temperature and with a high field at a temperature close to absolute zero and a low field at a temperature close to absolute zero. The open circles represent the relative population levels of the levels in each circumstance.

The atomic spin of these atoms preferentially line up with the field in the same direction.

The magnetic field is ramped up to 6.6 T, which releases the heat of magnetisation corresponding to the energy difference between the ground energy at low field and the final field. Figure 4.4 shows the temperature of the cell from after the magnet's full magnetisation to the end of the cooling process. First the dilution refrigerator removes the excess heat over the course of a week or two and returns the cell to base temperature (compare the two middle most parts of fig. 4.3). The field is then reduced to about 50 mT over several hours raising the energy of the copper nuclei, and as a consequence cooling the nuclear temperature. If we have removed all the current in the magnet the final field is limited by the internal field of the copper. We chose a final field of about 50 mT, because that balances the need to run vibrating wires without using high driving voltages that could heat the experiment.

Figure 4.5 shows the entropy temperature curves of copper at the initial and final fields of 50 mT and 6.6 T respectively. After the precool from (A) to (B) the entropy and temperature is decreased. The demagnetisation from (B) to (C) raises the energy of the copper nuclei, while staying at constant entropy. As a consequence they have to cooldown as shown in fig. 4.5. The copper nuclei reach a final temperature in the micro-Kelvin regime[85].

The conduction electrons in the metal lattice provide the necessary thermal link to ^3He via lattice phonons and the atomic nuclei. The electrons conduct heat to the atomic nuclei by exchanging spins with the nucleus. This process, the Korringa mechanism, has a relatively long relaxation time. Which means the conduction electron temperature is separated from the nuclear temperature[85]. The lattice and conduction electrons are relatively well thermally linked and have the same temperature.

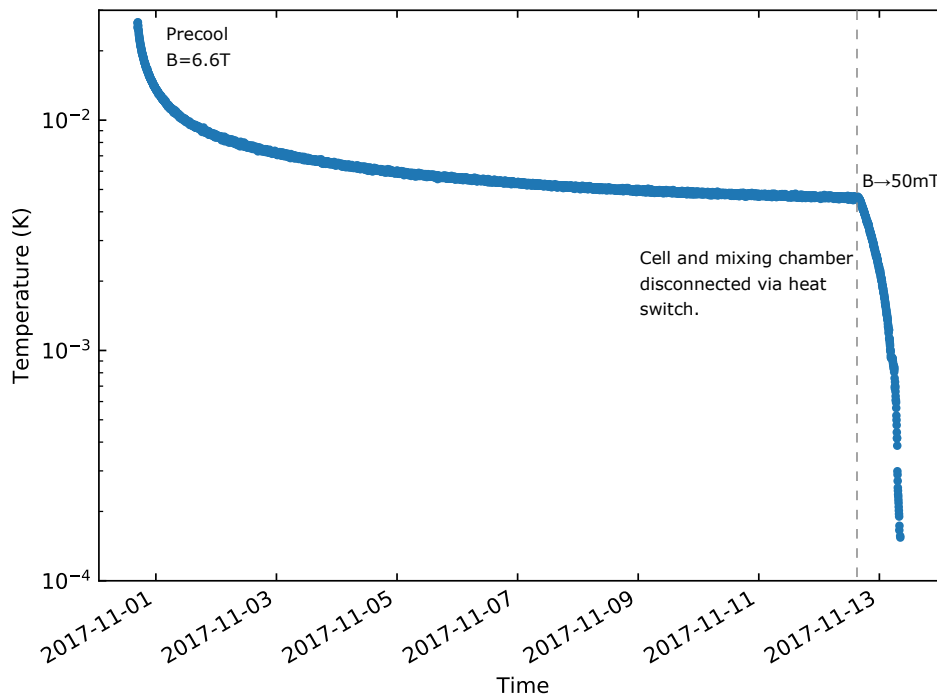


FIGURE 4.4: Semi-log plot of the measured ^3He temperature in the inner cell during the precool period of a typical demagnetisation run. On the left we see a higher temperature due to the magnetisation of the cell to high field. Over a two week period the dilution refrigerator cools the cell down to 4.6 mK. The cell was then demagnetised, indicated by the sharp turn down, cooling the cell further to about 150 μK .

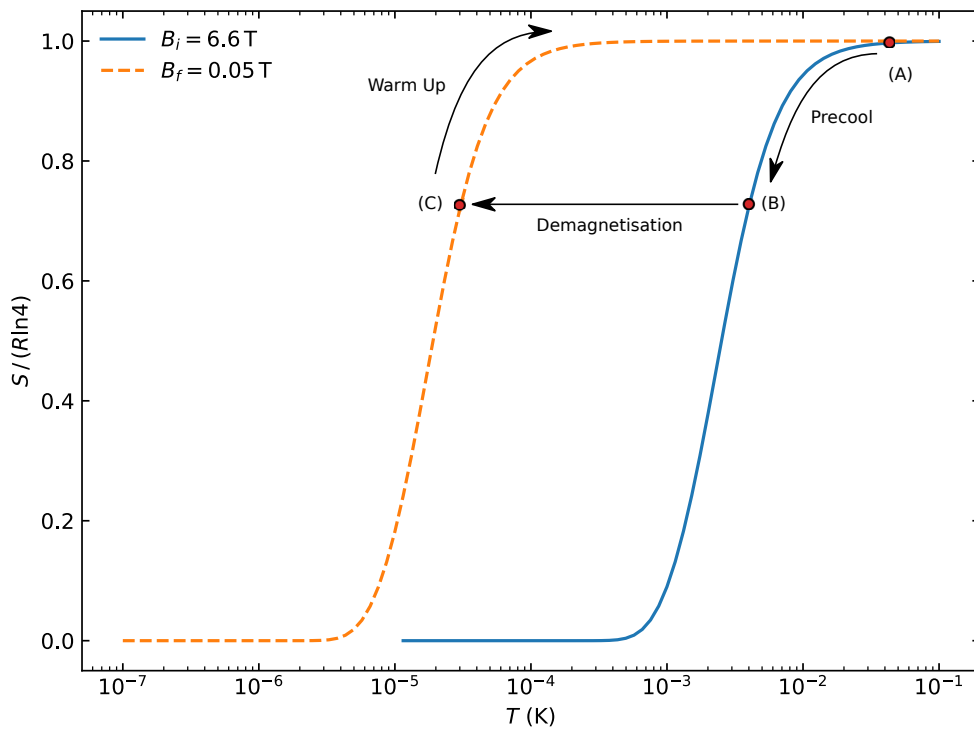


FIGURE 4.5: The entropy of copper as a function of temperature at a initial field B_i of 8 T and final field B_f of 0.05 T. After magnetisation at (A) the dilution refrigerator cools the system down to (B). At (B) the field is then reduced which cools the system to (C).

To cool liquid ^3He the lattice exchange phonons with the liquid. However the large sound velocity difference between the two systems leads to large Kapitza resistance which limits the cooling of the ^3He liquid. In practice we overcome the Kapitza resistance by plating the copper with silver sinter[85], which increases the thermal contact area. The final temperature of the ^3He liquid, balanced between the cooling power and a heat leak of about 2 nW, is around 100 μK to 150 μK and can be held for about 3 to 4 days depending on the heat generated by experiments.

4.4 Noise and Heat Leak Reduction

In the ultra low temperature regime many possible sources of noise and heating can interact with the cryostat and cause heating in the cell. Here we discuss some of these sources and the methods used to mitigate or decrease them.

Vibrations in the cryostat are an immediate source of noise that have to be mitigated since they cause eddy current heating from the magnetic fields used in operation[85]. Vibration can come from the nearby pumps necessary for operation and also nearby vehicle traffic on roads close to the building. To mitigate this pipes have high and low frequency noise breaks, and furthermore the whole cryostat assembly is raised on air-springs. Integral concrete blocks and lead provide the necessary mass to decrease the resonant frequency of the system to much below 1 Hz, again decreasing any vibrations.

Electromagnetic radiation can also cause heating on the cell. This is mostly reduced by having the whole cryostat placed in a shielded room acting as a Faraday cage. With this we stop mobile phone radio signals and the like disturbing the measurements. Radio frequency emissions from instruments inside the shielded room however can still affect the cell via pick-up by the measurement lines. Early measurements discovered that the new light emitting diode lights switching power supply caused excessive heating when the cell was demagnetised and it was necessary to turn these off. Investigation showed that the lights emitted high frequency radio noise that can be picked by the experimental wiring. After this discovery unnecessary instrumentation and leads were turned off and unplugged to further decrease the noise level and cell temperature.

Other sources of heat leaks include ionizing radiation from multiple sources. The likelihood of events was decreased by avoiding radioactive materials during construction. Likewise the concrete blocks and lead around the cryostat protect the cell by shielding it. However, it is of course impossible to completely block all sources of ionizing radiation and thermometry readings from the cell bolometer at ultra low temperatures regularly shows heating spikes like that in fig. 4.6 from the presumed

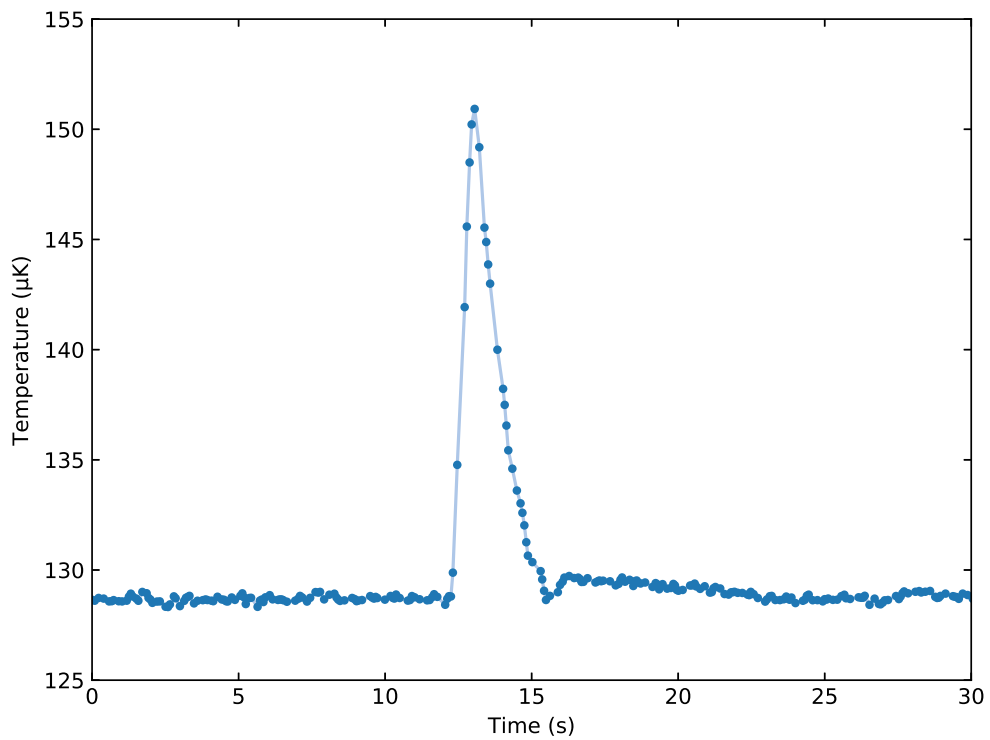


FIGURE 4.6: The temperature measurement of one of the thermometer wires during a heating spike from the presumed passage of radiation through the cell bolometer. Such events are a fairly regular occurrence during the course of measurements.

passage of radiation. In the bulk cell these events were not seen but will certainly cause background heating of the refrigerant.

Chapter 5

Multi-Frequency Measurements and Techniques

The standard setup to measure a resonance of an oscillatory device is to use a single frequency to sweep step by step through the response of the device with a signal generator and a lock-in amplifier. This method is well established and in addition to studying linear oscillators, it can be used to characterise strongly non-linear Duffing-like systems[88]. Recently researchers in the atomic force microscopy (AFM) community have found that using multi-frequency techniques can yield the phase-separated amplitude dependence of the non-linear forces on a resonator[19, 89, 90].

In AFM the resonance of a cantilever is used to detect the tip-surface force of a sample. Changes to the resonance characteristics (the height and phase) at a single frequency are used to detect non-linear atomic forces from the sample surface. To find more information about the properties of the sample material, researchers looked into exploiting the non-linear nature of the atomic force with multi-frequency methods[18]. These methods are specifically designed to measure non-linearity and improve the sensitivity of the device[18].

First of all it is possible to measure the device response at higher harmonics of the drive frequency[91]. However these harmonics do not usually coincide with the cantilever modes of the AFM tip, limiting the response. The cantilever can be engineered to have coincident modes or two driving tones at the first two harmonics of the resonator can be used in Bi-modal AFM[92]. Abandoning two-frequency excitations it is possible to synthesize a frequency band excitation and explore the Fourier transform of the response[93]. However this method is difficult to control and data heavy[18].

It is a well known effect that when two tones drive a non-linear resonator, extra frequency responses known as intermodulation or mixing products are produced. The measurement of these products characterises the signal distortion of a system. Recent research showed that these intermodulation products can then be used to find the non-linear forces that produced them[19].

To better find the non-linear forces *Intermodulation Products AB* custom-built an instrument to measure intermodulation products[94]. The instrument known as a Multifrequency Lock-in Amplifier (MLA) can produce excitation signals, or tones, at a number of frequencies simultaneously and then measure the response from a circuit. It achieves this by using an internal base tone f_b that is integer n multiplied to the measurement frequencies f_m , so that $f_m = n f_b$. Since the intermodulation products are produced at a fixed frequency separation this is an advantageous design for their measurement, since the measurement frequencies are separated by the fixed frequency f_b .

Quantum turbulence is also a non-linear force, so in principle a multi-frequency excitation in such a system would also generate intermodulation products. We will use the same techniques that have improved AFM sensitivity. These will hopefully elicit further information about the non-linear force of quantum turbulence.

This chapter will discuss measurements made with the MLA in liquid helium. In section 5.1 we will learn how to use it by taking measurements of a tuning fork in the linear regime of liquid ^4He . In section 5.2 we will pursue and discuss the MLA's primary purpose by using it to measure the non-linear forces of quantum turbulence in ^4He .

5.1 Multi-frequency effects in the Linear Regime

The response to a multi-frequency excitation spectrum for a purely linear device will be exactly the same as for the single frequency cases. The multi-frequency response is the superposition of all the single frequency responses at the frequencies of excitation. Here we will show that a tuning fork is a linear device and show the validity of using a multi-frequency technique in liquid helium to measure tuning fork resonators.

5.1.1 Multi-frequency Measurements of a Tuning fork

Quartz tuning forks as previously mentioned in chapter 3 intrinsically have a high quality factor. For the forks used in this work the intrinsic quality factor at low temperatures exceeds 100000. A further benefit is that they are strongly linear devices that have negligible intrinsic non-linear forces. We can expect, in the absence of any other source of non-linearity (such as turbulence), that multi-frequency measurements on a tuning fork will have the same results as for a single measurement. Figure 5.1 illustrates the differences between the two techniques. The MLA can measure the entire resonance curve simultaneously in a frequency comb. A Stanford Research Systems SR830 lock-in amplifier can only measure one frequency at a time however

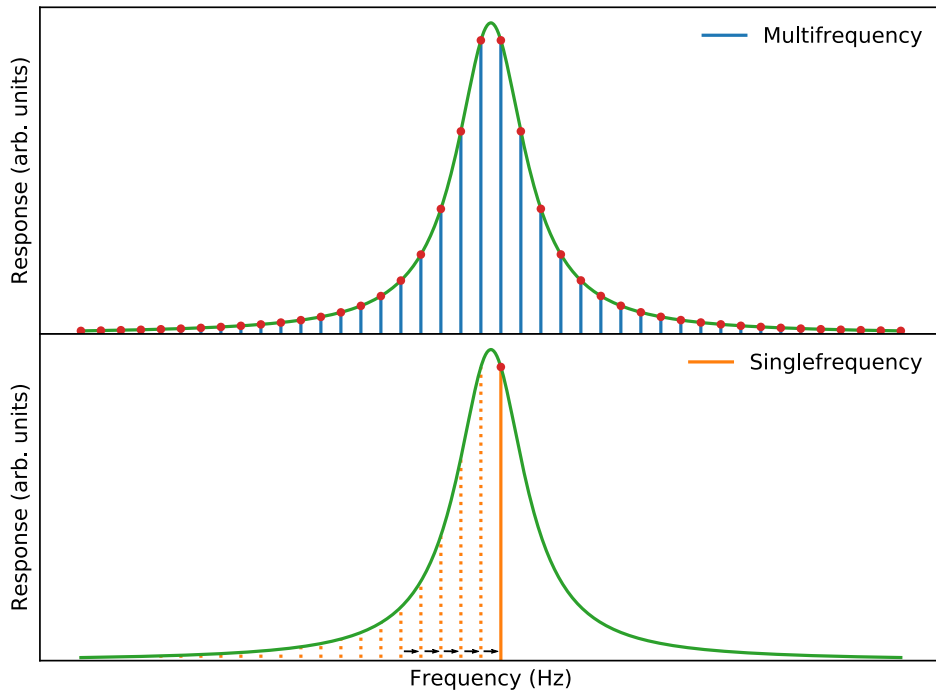


FIGURE 5.1: A comparison between the two measurement schemes been tested here. On top we see the MLA can measure the entire resonances curve simultaneously. On the bottom we see the single frequency method must map out the resonance by sweeping along the resonance curve.

so must sweep the measurement frequency across the resonance, recording data as it goes.

In order to test the MLA a quartz tuning fork was mounted and placed in a ^4He immersion cryostat[26]. The fork was then alternately connected to an Agilent Technologies signal generator and SR830 lock-in amplifier combination measuring at a single frequency, and then to the MLA that can generate and measure at up to 42 frequencies. This way the fork could be measured in a single frequency mode or a multi-frequency mode.

The tuning fork itself had a length of $2600\ \mu\text{m}$, a prong width $25\ \mu\text{m}$, a prong thickness $90\ \mu\text{m}$ and an inter-prong distance $25\ \mu\text{m}$; giving a corresponding resonance frequency of about $12\ \text{kHz}$. The input signal was attenuated by $20\ \text{dB}$, and a $1\ \text{MV A}^{-1}$ current voltage converter (transimpedance amplifier) stepped up the fork's output to the lock-in amplifier. The helium bath was cooled down to a temperature of $1.45\ \text{K}$ from $4.2\ \text{K}$, making the $^4\text{He-II}$ about 90% superfluid (see fig. 2.2).

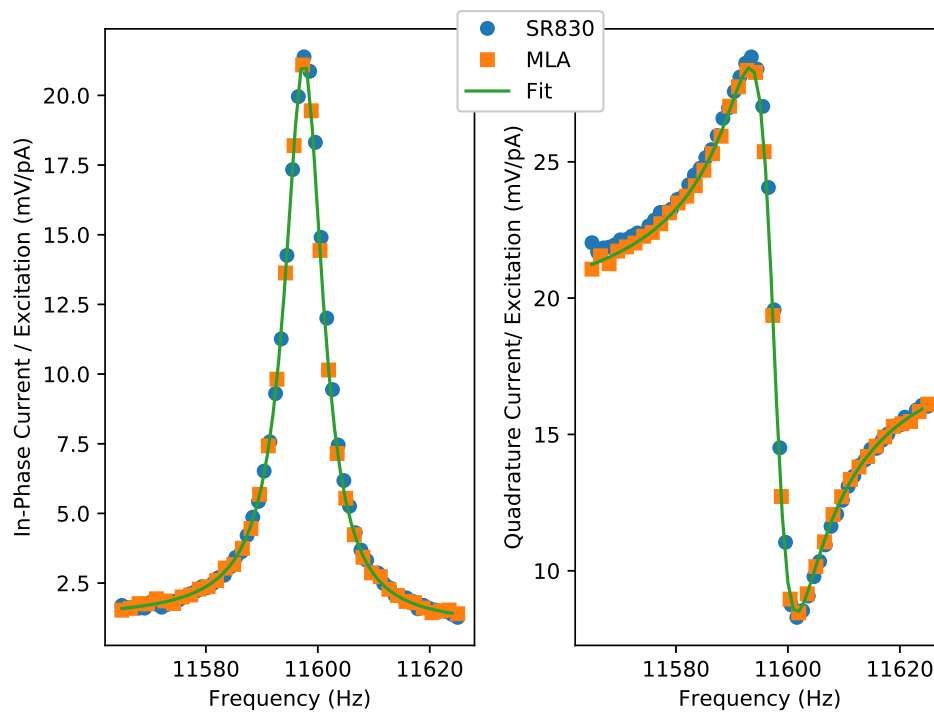


FIGURE 5.2: Single and multi-frequency measurements of a quartz tuning fork taken by a SR830 and the MLA respectively. The measurements agree with each other closely indicating linear behavior[20].

Figure 5.2 shows frequency sweeps of the fork taken by both by the single frequency SR830 in blue circles and the multifrequency MLA in orange squares. We normalise the results between the two instrument sets by dividing the measured current by the drive excitation. We can see both sets of measurements closely follow the Lorentzian fits shown by the green line for the in-phase and quadrature components.

The results shown in fig. 5.2 confirm that using the MLA in a multi-frequency mode in the linear regime is a valid method of measurement. If the system was non-linear we could expect to see the response of the MLA tones to be less than the single frequency measurements as energy goes into creating intermodulation products. Likewise the Lorentzian fit closely fits the data, further indicating a linear system.

5.1.2 Multi-frequency Measurements of a Fork Cooling in ^4He

We took further measurements while cooling down the tuning fork from He-I at 4.2 K to He-II at 1.45 K[26]. This allowed further comparison of the Lorentzian fits between the two instrument sets in similar conditions. Additionally this allowed us to test the 25 μm wide tuning fork against the existing hydrodynamic models.

The fork was measured by the single frequency method during a cooldown. The instrumentation was then swapped around and on the next cooldown the multi-frequency MLA was used. Unfortunately it was found that between the two cooldowns the resonances changed, most notably the width would always increase. Measurements of the frequency output of both the Agilent and the MLA showed negligible difference at a set frequency but not enough to explain what we observed. Furthermore, swapping both sets of instruments at 4.2 K found the same resonance.

A breakthrough came when we cleaned the fork with acetone and isopropanol (commonly known as IPA). We found that the fork's resonance was reset back to the width that it had before we started the liquid helium experiments. It is possible that the immersion fridge had oil and other dirt in it that attached to the fork (see fig. 3.4 for an example of this) and, considering the fork's exceptionally small size, strongly affected the resonance. Another cause of our observations could be bubbles from helium boil off, which could certainly explain measurement scatter in He-I; but the high thermal conductivity of He-II means bubbles can only be formed by cavitation which occurs at much higher velocities than were used here[95, 96]. Since the difference was also observed with He-II it is more likely that dirt was the issue.

After cleaning the forks we used both instruments to record the fork during a cooldown. The cooling process was paused during the measurements and instrumentation swapped so dirt could not effect the comparison.

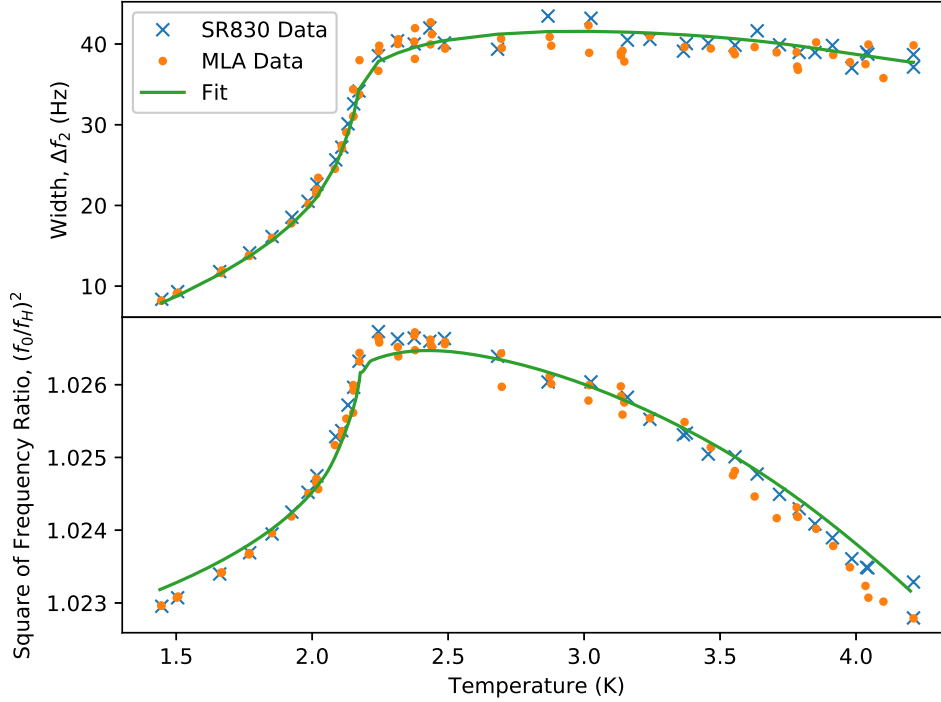


FIGURE 5.3: The changes of the resonant square of the frequency ratio (bottom) and width (top) for the 12 kHz fork in liquid ${}^4\text{He}$ as a function of temperature[20]. A fit to the hydrodynamic drag in eqs. (3.24) and (3.25) (green lines) is also shown. The data has been taken by both the SR830 (blue crosses) and the MLA (oranges dots).

Figure 5.3 shows the data taken during the cooldown comparing the two instruments, at each measurement temperature we would measure the resonance curve of the fork with each instrumentation set. We plot both the damping width and square of the frequency ratio against the helium temperature. We show both single-frequency measurements with blue crosses and multi-frequency as orange circles. We compare these together with a green line that is a least squares fit to the hydrodynamic drag using eqs. (3.24) and (3.25).

In fig. 5.3 we can see that measurements with both instruments show a similar trend. Above the superfluid transition temperature there is some scatter in the results which is probably due to bubbles in the helium effecting the fork. Immediately upon entering the superfluid the bubbles and the scatter disappear. The least squares fit to eqs. (3.24) and (3.25) found $\beta = 0.103$, $B = 0.236$ and $C = 0.411$ [20].

A better hydrodynamic fit can be obtained using the vacuum frequency as a fitting parameter to the least squares fit. The possible reason for the change of vacuum frequency is that dirt in the helium affected the resonance characteristic of the fork in

the initial immersion adding the additional mass. This further emphasises the effects of dirty helium on sensitive small devices such as these forks. A dedicated cell with a filter could prevent this being a problem in the future.

The agreement between the MLA and single frequency technique shows that multi-frequency measurements in the linear regime of helium are completely valid and agree with single frequency techniques.

5.2 Multi-frequency effects in the Non-Linear Regime

The success of the multi-frequency measurements in ^4He lead to the logical next step of measuring other effects in helium with the technique. Turbulence is a well known phenomena in helium and the use of quartz tuning forks to study it is also well documented[10–14]. However, turbulence is a non-linear effect and non-linear effects on multi-frequency excitations cause notable differences to the linear case.

Non-linear behavior in oscillators can be seen in the deviation from the idealised oscillator discussed in chapter 3 and section 5.1. A frequency sweep of the oscillator will no longer show an Lorentzian curve and changing the direction of the sweep may show hysteresis in the measured responses. Often a Duffing oscillator, which introduces a cubic dependence in addition to the standard Hooke's law, is used to model the behaviour of a device in these circumstances, but this can not explain all circumstances. In this section we derive how to extract information from the generation of intermodulation products as set out by Haviland *et al.*[21, 90]. We then apply these methods to new measurements taken for this thesis.

5.2.1 Intermodulation Products

A non-linear oscillator will not have a simple superposition of single frequency responses as a linear device. Instead some of the input energy goes into the creation of extra responses at additional frequencies, commonly known as intermodulation products.

Intermodulation products have been known about in another form for centuries. In music they are know as Tartini notes (or combination tones) after Giuseppe Tartini, who described them[97]. If two notes are played with frequencies f_1 and f_2 and they have sufficient intensity a third note at frequency f_3 will be heard at the difference of the two notes:

$$f_3 = |f_2 - f_1|. \quad (5.1)$$

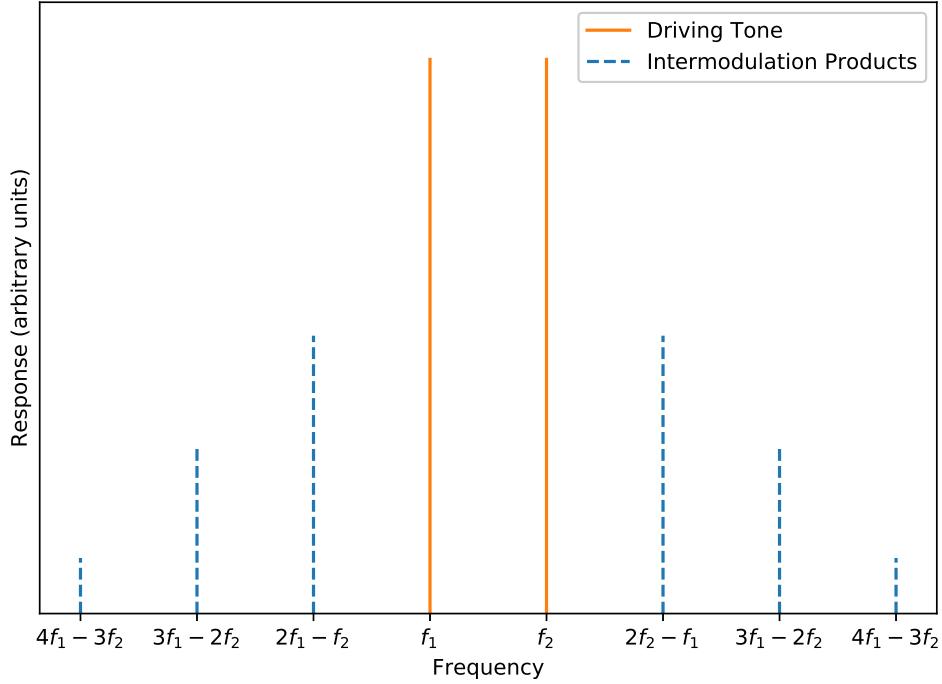


FIGURE 5.4: In a nonlinear system the two driving frequencies (orange lines) generate intermodulation products (dashed blue lines) around the driving tones at integer combinations of the two driving tones. Responses at high frequencies about $2f_1$ and above are not shown.

In addition to this note a careful listener would also pick up other notes whose frequencies are at integer combinations of the two original notes:

$$f_i = mf_2 \pm nf_1, \quad (5.2)$$

where m and n are any non zero integers, (see fig. 5.4). This curious effect has its roots in the non-linear workings of the inner ear, as well as psychoacoustic effects. A (linear) receiver recording in the same room as the listener would not be able to detect the intermodulated notes.

Inherently non-linear devices and linear devices introduced to a non-linear force will produce intermodulation products in multi-frequency excitations. We are interested in the case where a linear device is measuring a damping non-linear force $f_{nl}(\dot{x})$ as a function of velocity from quantum turbulence. To extract information about the non-linear force, and hence quantum turbulence, we start with the equation for a driven simple harmonic oscillator and add the non-linear damping force:

$$m\ddot{x} + \gamma\dot{x} + m\omega^2x = F + f_{nl}(\dot{x}), \quad (5.3)$$

where the dot notation indicates differential order with respect to the time t .

Considering the purely linear case we can take the the Fourier transform of eq. (3.1) and find:

$$\hat{\mathbf{x}} = \hat{\mathbf{G}}\hat{\mathbf{F}} \quad (5.4)$$

where $\hat{\mathbf{G}}$ is the linear transfer function of the oscillator; the hat on $\hat{\mathbf{x}}$, etc indicates it is now a function of frequency, bold indicates a vector or matrix variable. The linear transfer function transforms the drive spectrum into the oscillator's response and the components of the matrix \hat{G}_{kl} can be found as (see eq. (3.3)):

$$\hat{G}_{kl} = \begin{cases} \frac{1}{m(\omega_0^2 - \omega^2 + i\gamma\omega)} & \text{for } k = l \\ 0 & \text{for } k \neq l \end{cases}. \quad (5.5)$$

We can perform a Fourier transform on eq. (5.3), and using eq. (5.4) we can find that:

$$\hat{\mathbf{x}} = \hat{\mathbf{x}}^{(\text{free})} + \hat{\mathbf{G}}\hat{\mathbf{f}}_{\text{nl}} \quad (5.6)$$

where $\hat{\mathbf{x}}^{(\text{free})}$ is the response for the purely linear system from eq. (5.4) and $\hat{\mathbf{x}}$ is the response of the system in the presence of non-linear forces. This assumes that the non-linear force does not affect the driving spectrum, which in our case is true because the fork is driven electro-mechanically and has a high effective mass.

We know that the non-linear force will create intermodulation products in the response spectrum of $\hat{\mathbf{x}}$ at extra frequencies to that of the drive spectrum. Measuring these can now reveal the non-linear force through eq. (5.6):

$$\hat{\mathbf{f}}_{\text{nl}} = \hat{\mathbf{G}}^{-1}(\hat{\mathbf{x}} - \hat{\mathbf{x}}^{(\text{free})}) \quad (5.7)$$

The non-linear response will have intermodulation products due to the non-linear forces on the fork. Equation (5.7) gives the Fourier components of the non-linear force on the fork.

Figure 5.5 shows a visual example of eq. (5.7). In blue at the top we have measured the linear response spectrum $\hat{\mathbf{x}}^{(\text{free})}$ on the left, and calculated the corresponding Fourier transform to find $x(t)$ on the right. In the middle, in orange, we show the measured non-linear response $\hat{\mathbf{x}}$ in a similar manner-showing a couple of intermodulation products. At the bottom in green we find the difference of the above to get the non-linear force spectrum $\hat{\mathbf{f}}_{\text{nl}}$.

The next step is to downshift the frequency of the inverse Fourier transform of eq. (5.7) by a carrier frequency ω (typically chosen to be in the middle of the spectrum); which will reveal an envelope function of the oscillations of the non-linear force f_{nl} the slowly moving amplitude of the beat pattern. Taking the real and imaginary

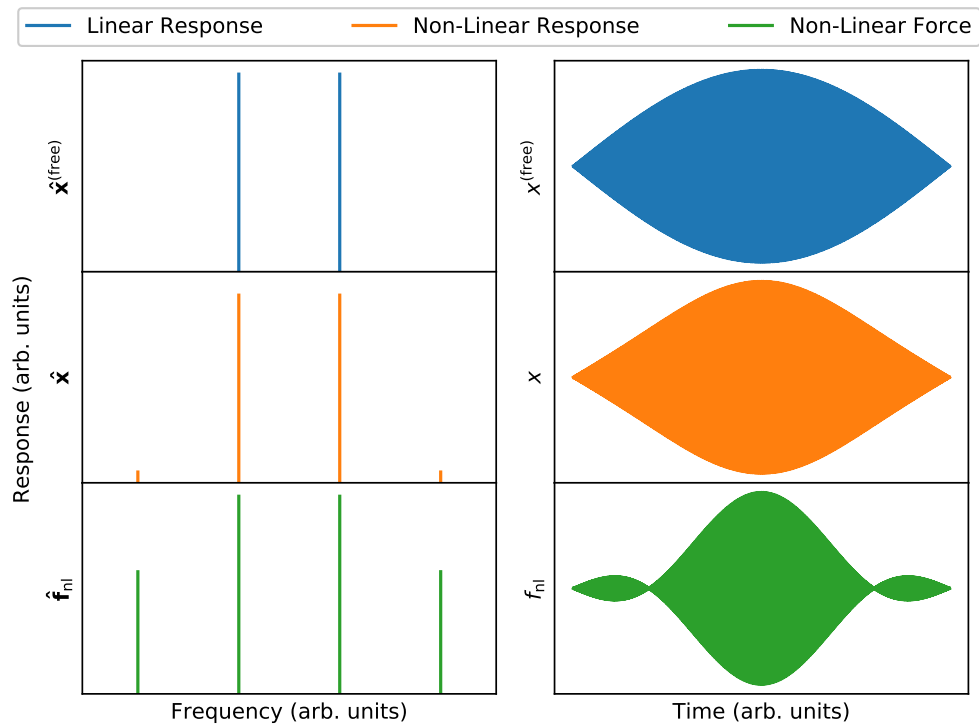


FIGURE 5.5: (Not to scale). A graph showing an example of the process in eq. (5.7). The left hand side shows the measured or derived spectrums while the right shows the corresponding Fourier transform (see text for details). The linear response, non-linear response and derived non-linear force are shown in blue, orange and green respectively.

components of f_{nl} will find the in-phase F_I and quadrature F_Q components of the non-linear force, which we compare to the envelope functions of the velocity amplitude to find the non-linear force as a function of the velocity amplitude $A(t)$ [98].

$$F_I(A) = \frac{1}{T} \int_0^T f_{nl} \cos(\omega t) dt \quad (5.8)$$

$$F_Q(A) = \frac{1}{T} \int_0^T f_{nl} \sin(\omega t) dt, \quad (5.9)$$

where T is the carrier oscillation period $T = 2\pi/\omega$.

The physical interpretation of F_I and F_Q is that they are the conservative and non-conservative non-linear forces respectively. The in-phase force F_I is related to the frequency shift of the oscillator[21]. A negative F_I would correspond to a retarding force on the fork's velocity, while positive would correspond to a force increasing the fork's speed. Negative F_Q corresponds to a to energy been lost by the fork to the force interaction and to energy storage if positive[21].

To easily compare the intermodulation amplitude sweeps to single frequency sweeps we will need to find the peak beat velocity. This can be calculated by summing the out of phase v_Q and in phase v_I measured components for each tone in quadrature:

$$v = \sum^n \sqrt{v_{In}^2 + v_{Qn}^2}. \quad (5.10)$$

The total force is calculated by summing the force at each tone:

$$F = \sum^n F_0 \cos \left[\arctan \left(\frac{v_{Qn}}{v_{In}} \right) \right], \quad (5.11)$$

where F_0 is the driving force amplitude.

5.2.2 Non-Linear Forces of Quantum Turbulence in ^4He

We demonstrated in section 5.1 that the tuning fork's response was linear at low velocities, but we did not show this at higher velocities. A key assumption of the intermodulation technique is that the device we use is linear in the range we observe intermodulation in. So in order to confirm that there are no intrinsic nonlinear effects in the range of velocities we used the fork for in turbulence, we placed the fork in a vacuum probe and immersed the probe in liquid ^4He at 4.2 K. The fork had a width of 50 μm , prong separation 90 μm , thickness 90 μm and prong length 1750 μm . After placing the fork in ^4He immersion fridge at 1.3 K we applied intermodulation techniques to the fork as well as a single frequency amplitude sweep.

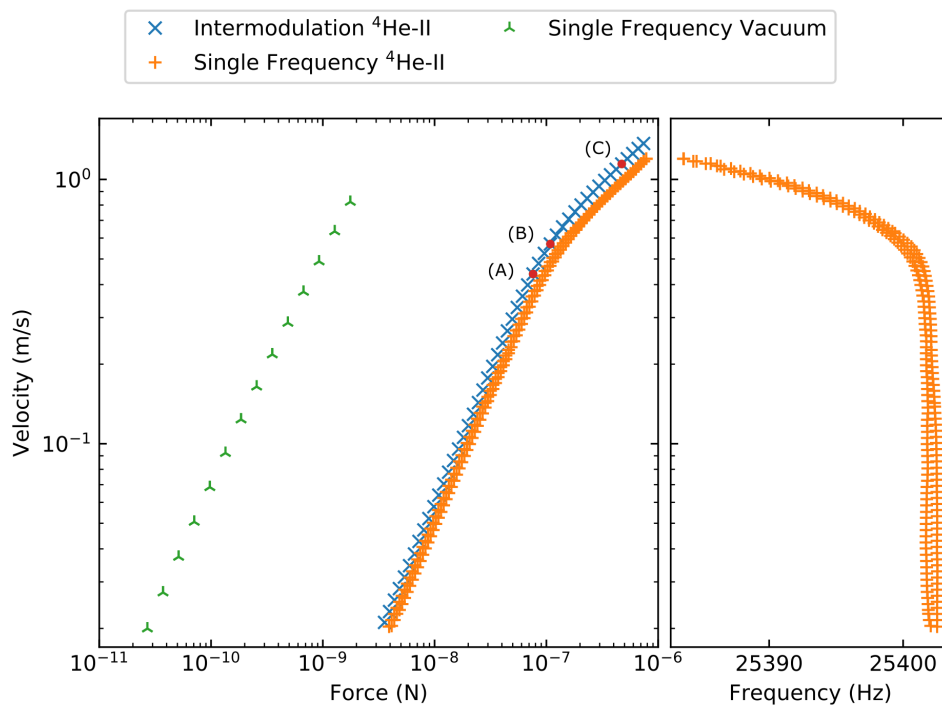


FIGURE 5.6: (Left) A log-log plot of the force velocity curve of the fork in He-II at 1.3 K. (Right) Velocity against frequency of the tuning fork from the same single frequency measurements as the left hand plot. Orange crosses show the single frequency excitation amplitude sweep, blue x's show the calculated force-velocity from the intermodulation sweep and the green tri-markers show the vacuum single frequency sweep. The red dots and letters show those sweeps that are analysed in detail later (see text).

The left plot of fig. 5.6 shows the force velocity curve for the fork in He-II at 1.3 K and in vacuum at 4.2 K, it shows the distinct transition from linear laminar damping to increased turbulent damping at about 40 cm s^{-1} . Both the intermodulation and single frequency sweeps are shown in the blue crosses and orange pluses respectively. Each intermodulation data point in fig. 5.6 was measured for 60 s by the MLA to reduce Fourier leakage. There is a slight difference in the two measurements that we ascribe to small change in temperature between the two measurements. The vacuum data in green show no significant intrinsic effects affecting the fork at these velocities.

The right hand side of fig. 5.6 shows the resonant frequencies of the fork as a function of the fork's velocity. The points were measured by the single frequency amplitude sweep on the left plot of fig. 5.6. Initially the data are fairly vertical before curving to the left where turbulence is generated by the fork. It was found in analysis that the raw data had a high degree of hysteresis and moved to high frequencies at high velocities, which is counter-intuitive to the expected behaviour. This maybe is the fault of the measurement program tracking the frequency with V_y/V_x within 1%. The program could be following one edge of the peak and then the other side on the reverse sweep. To correct the raw data a correction factor was used:

$$\Delta f_1 = 2\Delta f_2\phi \quad (5.12)$$

where Δf_1 is the frequency correction and ϕ the phase.

Here we present the main difference between single frequency methods and the MLA's measurements. While with single frequency sweeps we only use an average, the MLA allows nonlinear force extraction from a single measured point, provided the linear response of the device is known. Below we shall analyse in detail data points from fig. 5.6 showing the first evidence of turbulence (A), moderate turbulence (B) and a fully turbulent point (C). For ease we have marked these points in fig. 5.6 with red circles and letter respectively.

The method relies on been able to compare the linear and non-linear responses of the resonator at the same drive. In AFM this is easily achieved by exciting the resonator away from the sample's surface. In our experiments however we cannot remove turbulence to compare the linear and turbulent responses of the fork in helium. In order to find the linear response at turbulent velocities we extrapolate the linear regime data at lower velocities to higher drives. In practice we chose the first 20 sweeps from fig. 5.6 for this purpose. Because we know that the fork is linear in the range of velocities explored, this extrapolation should be a valid assumption.

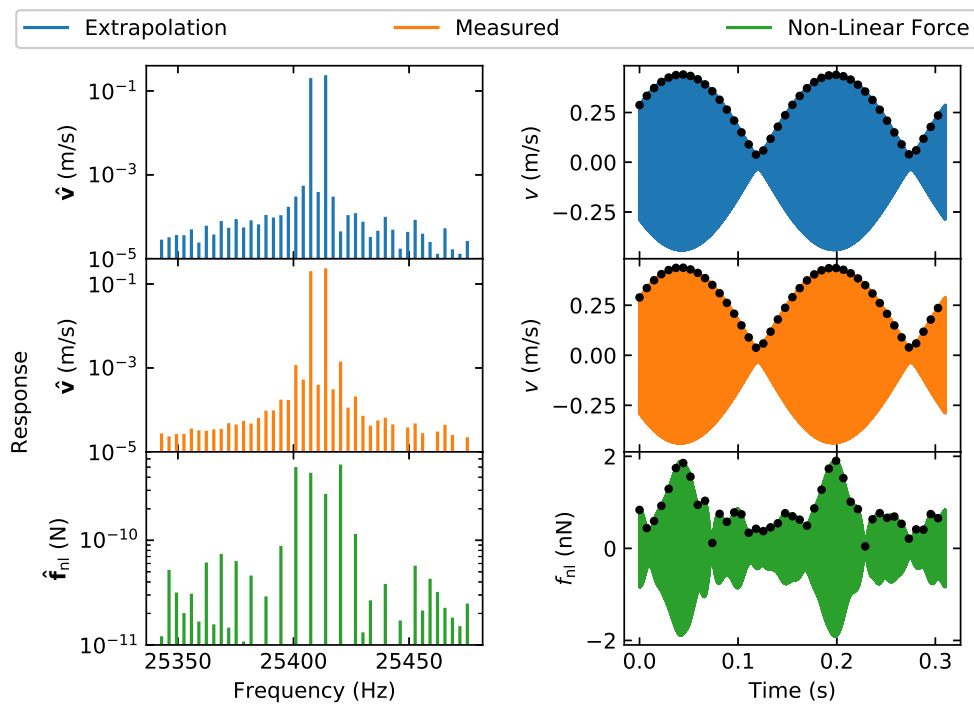


FIGURE 5.7: Measured and derived spectrums; and their inverse Fourier transforms at the critical velocity of 43.9 cm s^{-1} . The non-turbulent spectrum in blue was extrapolated from data taken before turbulence set in. The turbulent spectrum in orange was directly measured. The force spectrum in green was derived by comparing the other two (for the details see text).

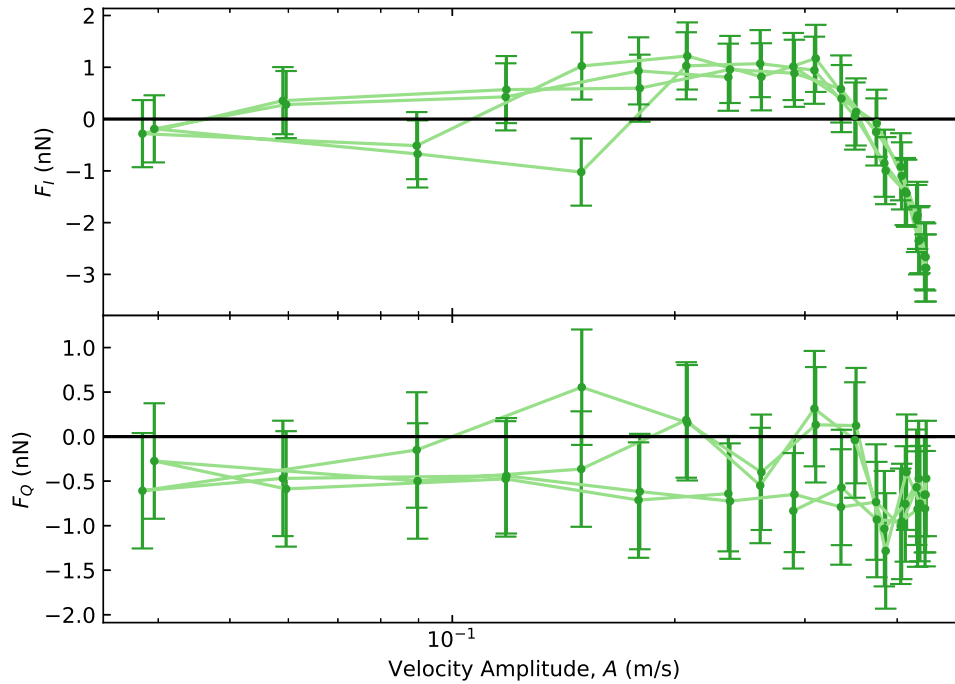


FIGURE 5.8: Semi-log graph of the non-linear force as a function of velocity amplitude at the critical velocity.

(A) Emergence of Turbulence

Figure 5.7 shows intermodulation analysis performing Fourier transforms on the data. The top row plots a linear extrapolated spectrum and beat pattern in blue extrapolated from the first 20 points in fig. 5.6. The middle row contains the actual measured spectrum and corresponding Fourier transform in orange. The bottom row has the calculated non-linear force spectrum in green found from eq. (5.7). The measured peak fork velocity was 43.9 cm s^{-1} with a corresponding peak force of 76.0 nN .

For the measurements shown in fig. 5.7 we chose to put measurement tones in-between the drive tones and the tones expected to measure intermodulation products. This was so we could easily see the effects of noise on the measurements. We can see from both the extrapolated and measured data in fig. 5.7 noise in those in-between background tones, in that they do not show a flat spectrum but rise towards the resonance. The force graphs in fig. 5.7 however do not see the effects of this noise because the extrapolation closely follows the measured data. This implies that the noise is linear in the drive. Fortunately the intermodulation products are larger than the noise so it seems reasonable to carry on the analysis.

In fig. 5.8 we show the calculated non-linear force curves as a function of the beat amplitude of the fork. The top and bottom graphs shows the in and out of phase force (F_I and F_Q) respectively. The top graph shows mostly noise between -1 nN and 1 nN until a velocity amplitude of 30 cm s^{-1} where it curves downwards beyond the noise. The bottom graph we describe completely as scatter.

The curve downwards of F_I indicates an conservative retarding force on the fork's motion. There is no evidence of any dissipative force in F_Q . It could be that remnant vortices attached to the fork are expanding outwards from the fork, increasing the drag the fork feels. Presumably these vortices do not bud off vortex rings in a significant manner and little energy is lost to the fluid so we do not see any evidence of dissipation above the noise.

(B) Just Above the Critical Velocity

The next sweep shown here in fig. 5.9 is at a peak velocity of 57.0 cm s^{-1} and peak force of 109 nN . We can still see the noise inbetween tones as discussed before. In the force spectrum we can see the appearance of four intermodulation products which gives a more developed non-linear force with a clear beat. The force looks symmetrical and is strongly dependent on the velocity: it peaks with the velocity and there is no force (apart from noise) if the velocity is too low.

Figure 5.10 shows the analysed non-linear force curves. The curve downwards in F_I is now more clearly developed with a deeper minimum. A slight hysteresis is observed with the ramp down of the beat so that the force stays higher for longer as compared to the velocity amplitude. F_Q has an upwards curve at a velocity amplitude of 45 cm s^{-1} . The spikes down in the curve seem unlikely to be physical in nature and are likely to be noise related. Again there seems to be hysteresis but here it falls to zero while staying at a high velocity amplitude.

The development of a positive out of phase force in fig. 5.10 would naively suggest that energy is being stored by the fork. However it is more likely that energy is going into the production of vorticity. This energy is then lost to the fluid as vortex rings bud off the remnant vortices attached to the fork in the so called vortex mill[99].

(C) Far Above the Critical Velocity

Figure 5.11 shows a sweep far into the turbulent regime. The fork's peak velocity in this sweep was 1.09 m s^{-1} and the force was 473 nN . We can see that at this stage the beat pattern for the measured data is asymmetrical and turbulence strongly limits the maximal velocity of the fork. The non-linear force beat rapidly increases with a longer tail which matches the slow decay of the velocity beat. The spectrums of the

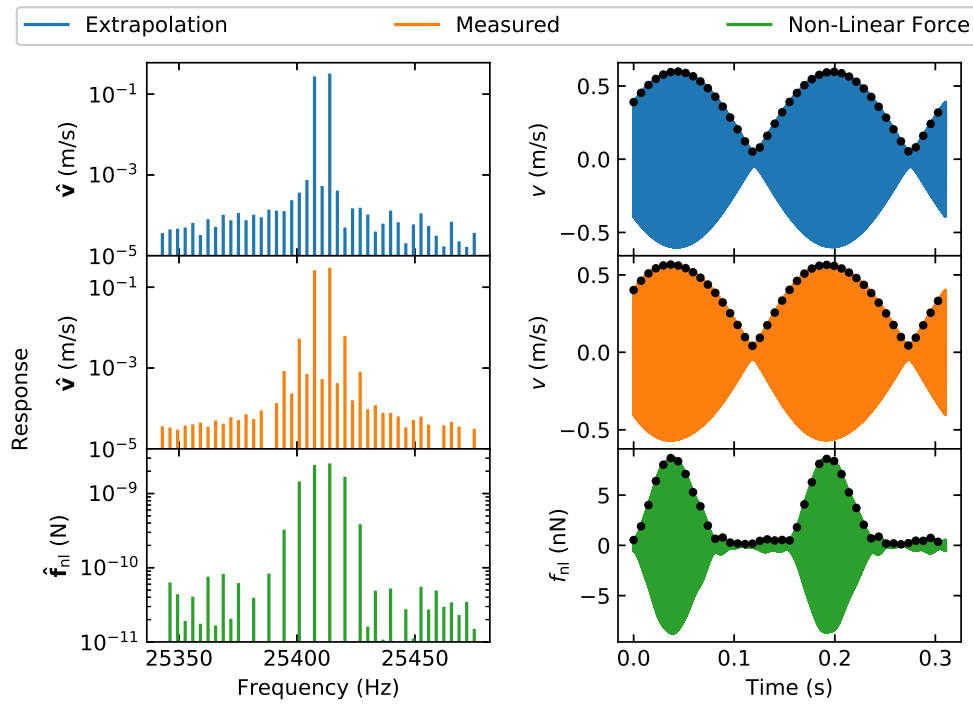


FIGURE 5.9: Measured and derived spectrums; and their inverse Fourier transforms just above the critical velocity. The non-turbulent spectrum in blue was extrapolated from data taken before turbulence set in. The turbulent spectrum in orange was directly measured. Lastly the force spectrum in green was derived by comparing the other two (see text).

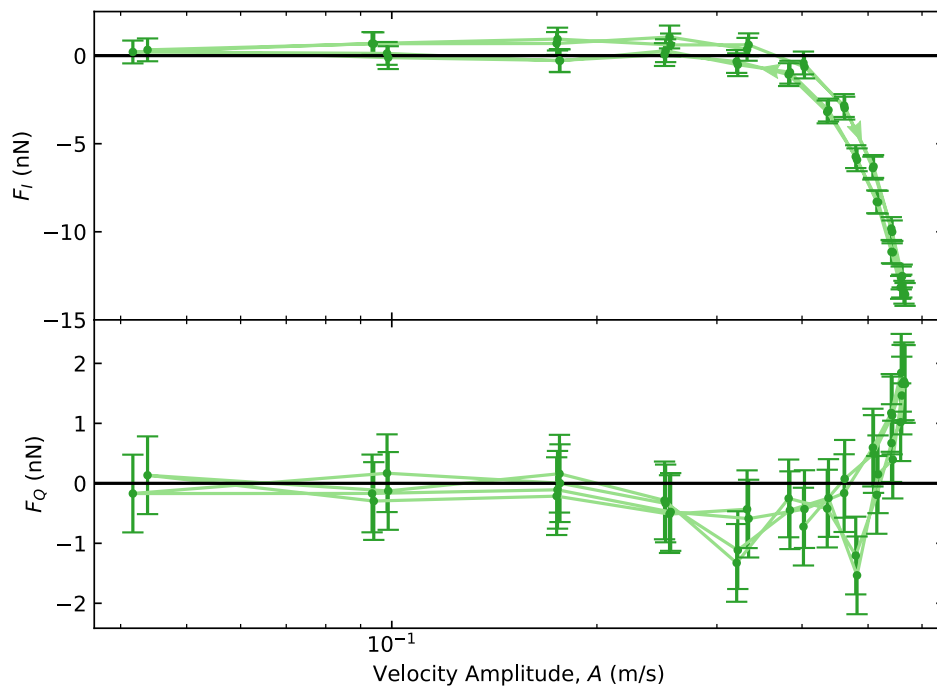


FIGURE 5.10: Semi-log graph of the non-linear force as a function of the velocity amplitude just above the critical velocity. The arrows indicate the direction of hysteresis.

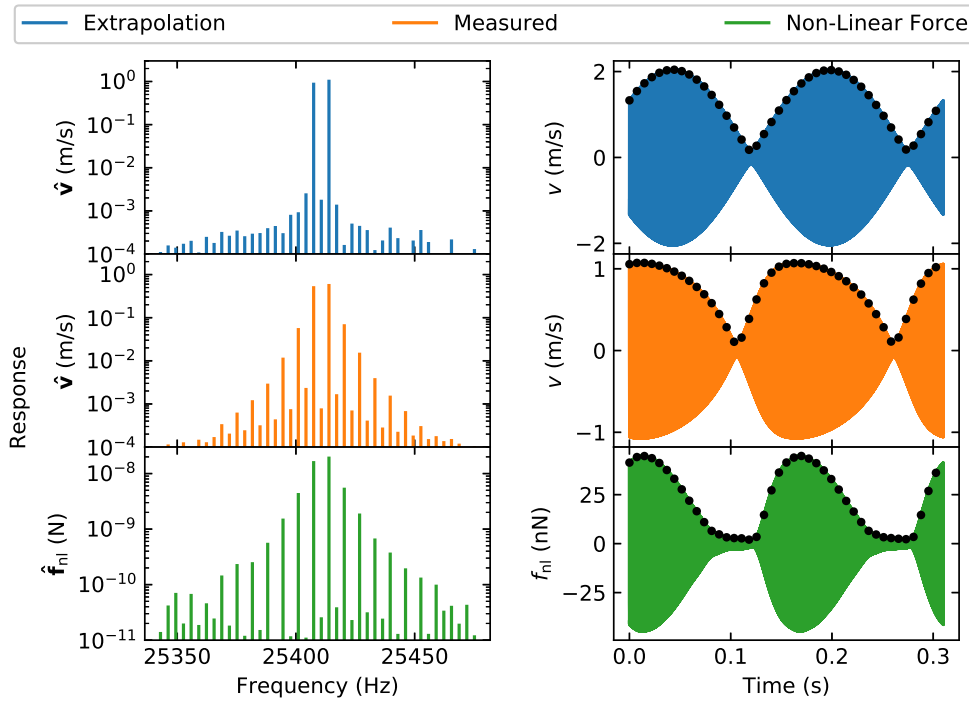


FIGURE 5.11: Measured and derived spectrums; and their inverse Fourier transforms far above the critical velocity. The non-turbulent spectrum in blue was extrapolated from data taken before turbulence set in. The turbulent spectrum in orange was directly measured. Lastly the force spectrum in green was derived by comparing the other two (see text).

measured velocity and the calculated force show well developed intermodulation products.

The non-linear force curves are plotted in fig. 5.12 where we see further development of the trends started in the last sweep. Unsurprisingly, given that the non-linear force beat is non-symmetric in fig. 5.11, both the curves show clear hysteresis. F_I again shows a slower decay in the velocity amplitude. F_Q shows stronger hysteresis but decays quickly in the velocity amplitude compared to the ramp up.

5.2.3 Discussion

Figure 5.13 shows a plot of data from figs. 5.8, 5.10 and 5.12 as well as sweeps not shown previously, allowing us to see the evolution of turbulence more easily. In F_I we can see that all three plots mostly follow the same dependence. While the biggest changes are seen in F_Q , which when fully pushed shows a degree of hysteresis. Though note that the velocity dependence on the rise is similar for both.

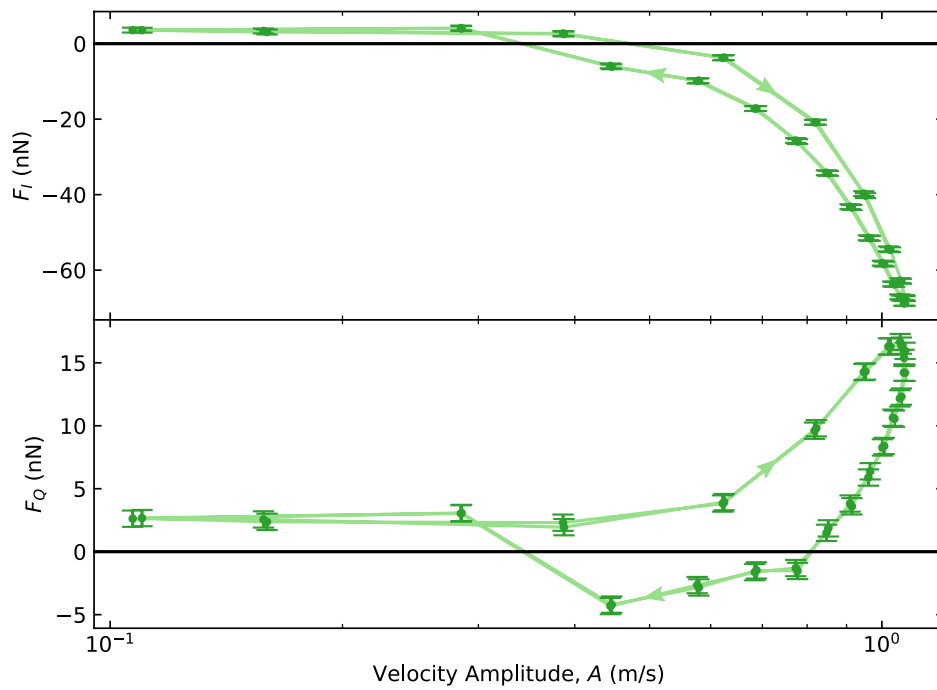


FIGURE 5.12: Semi-log graph of the non-linear force as a function of velocity amplitude far above the critical velocity. The arrows indicate the direction of hysteresis.

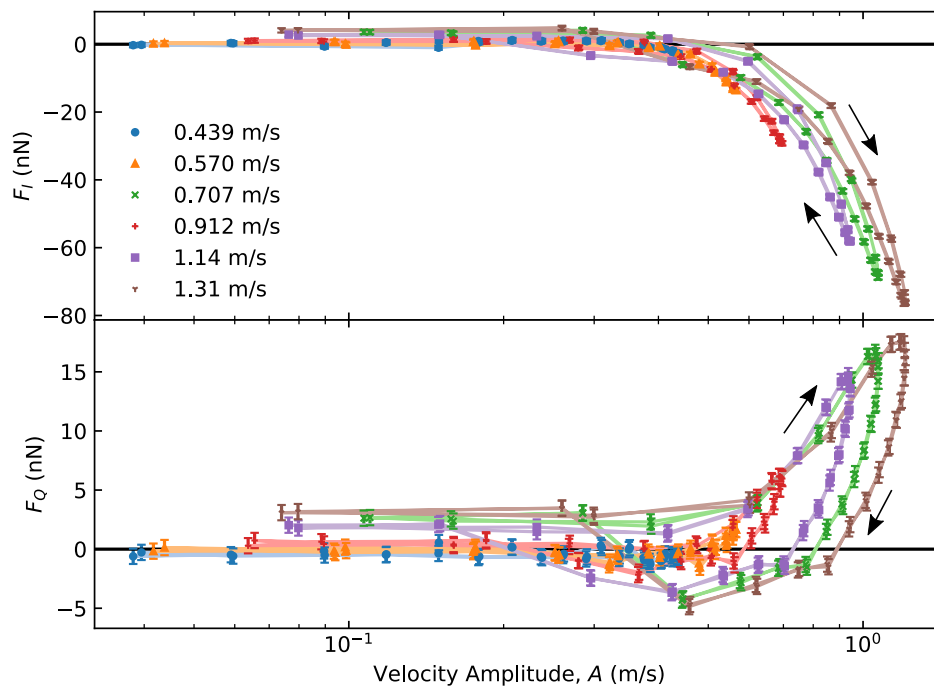


FIGURE 5.13: The non-linear force as a function of velocity amplitude with the data from figs. 5.8, 5.10 and 5.12 in blue circles, orange triangles and green squares respectively. Further sweeps have also been included at the indicated peak velocities. The arrows indicate the direction of hysteresis.

The in-phase non-linear force F_I we attribute to the damping effect of the boundary layer of vorticity[100] about the tuning fork. Mutual friction with the normal fluid adds to the effect of the layer. Naturally higher speeds will cause the vortex density to rise[100] causing a rise in F_I .

How do we physically interpret F_Q ? In AFM a positive F_Q is seen as energy storage by the oscillator, which in this system seems non-physical. A far more likely interpretation is that we are seeing energy dissipation instead. This would come from the loss of nucleated vortex rings into the bulk, the energy loss from re-connections into phonons and mutual frictional interactions between the two fluids. Elsewhere evidence of two critical velocities of quantum turbulence on quartz tuning forks has been seen in the turbulent drag force[101–103]. The suggestion in the literature, that this work supports, is that the first critical velocity corresponds to the expansion of remnant vortices on the fork and second is where vortex ring are budded off into the bulk[102–105].

Comparing the forces we see that F_I is around four times more than F_Q at the maximum. This suggests that the boundary layer around the fork has a larger effect than the loss of vorticity into the bulk. Looking deeper we see that F_Q is rising faster than F_I which could suggest a fully developed boundary layer steadily losing more and more vortex rings from the vortex mill to bulk as the velocity rises[100].

5.3 Summary

In this chapter we compared a multi-frequency measurement technique to a single frequency measurement technique and obtained the same results from both. We then further developed the multi-frequency technique to look at the non-linear forces in quantum turbulence.

In the linear regime we found that the MLA and SR830 lock-in amplifiers find the same results for a fork at low excitation velocities in ^4He . We also did a comparison of frequency sweeps as we cooled ^4He down from 4.2 K to 1.5 K and the results showed that single frequency sweeps and multi-frequency methods obtain the same results. We can conclude that single and multi-frequency methods obtain the same results in helium which opens up multi-frequency methods to fork measurement and also possibly multiplexing sweeps across multiple devices.

To further exploit the MLA we applied intermodulation AFM techniques to study quantum turbulence in He-II. Using low velocity measures to extrapolate a linear frequency spectrum we found we could successfully measure intermodulation products produced by quantum turbulence and find the non-linear force spectrum. Further analysis allowed us to find the in and out of phase components of the non-linear force as a function of the velocity amplitude of the beat.

To find the linear response of the fork in helium at turbulent velocities we extrapolated data from the linear regime at lower velocities. It would be far better to be able to confirm the non-turbulent response with the turbulent response directly. With careful cell design this might be possible by avoiding the creation of remnant vortices during the transition to He-II from He-I, such as has been done for wires[106].

The ability to resolve the in and out of phase force should allow us explore the nature of the effects of turbulence on the fork. The method is ideal for intrinsically linear devices such as tuning forks. Future work can look into how the nature of the non-linear forces change in ^3He turbulence and pure quantum turbulence at lower temperatures.

Chapter 6

A Quasiparticle Camera in $^3\text{He-B}$

The visualisation of quantum turbulence is an active research topic. In classical systems there is a wealth of information about velocity flows, boundary layers etc. By designing and operating experiments for quantum turbulence we should find equally valuable information for comparison with classical turbulence. In ^4He researchers have used tracer molecules (typically helium excimers[107] and solid hydrogen[108]) to trace vortex lines[7]. Oscillatory devices are naturally able to feel the effects of turbulence. However so far it is not possible to image the tangle about the device with itself. In essence we can think of the devices more like a switch, as soon as they detect turbulence they create turbulence. However the ultra-low temperature group at Lancaster has developed a new visualisation method in superfluid $^3\text{He-B}$ to exploit these switches[24, 109, 110].

Quasiparticles in ^3He are inherent to the fluid and at ultra low temperatures have ballistic trajectories. By creating a beam of these particles and directing them at a vortex tangle created by a wire, rotating the cryostat or neutron capture we should be able to detect changes in the flux from interactions with the turbulence. The ability to switch excess excitations on and off will allow us to compare images to find the effects of turbulence.

This chapter is split into two sections. Firstly, in section 6.1 we will explain how we create a quasiparticle beam in $^3\text{He-B}$, and then how we use a camera to detect it. We will use theoretical models and simulations to discuss the properties and physics of the beam made by the camera. In section 6.2 we will then use the camera and quasiparticle beam to image quantum turbulence generated by a vibrating wire.

6.1 Imaging a Quasiparticle Beam

6.1.1 Generating Light - The Quasiparticle Source

The principles of any camera is fairly simple, a source of light illuminates an object so that a camera can then image the object. The camera can detect the object by

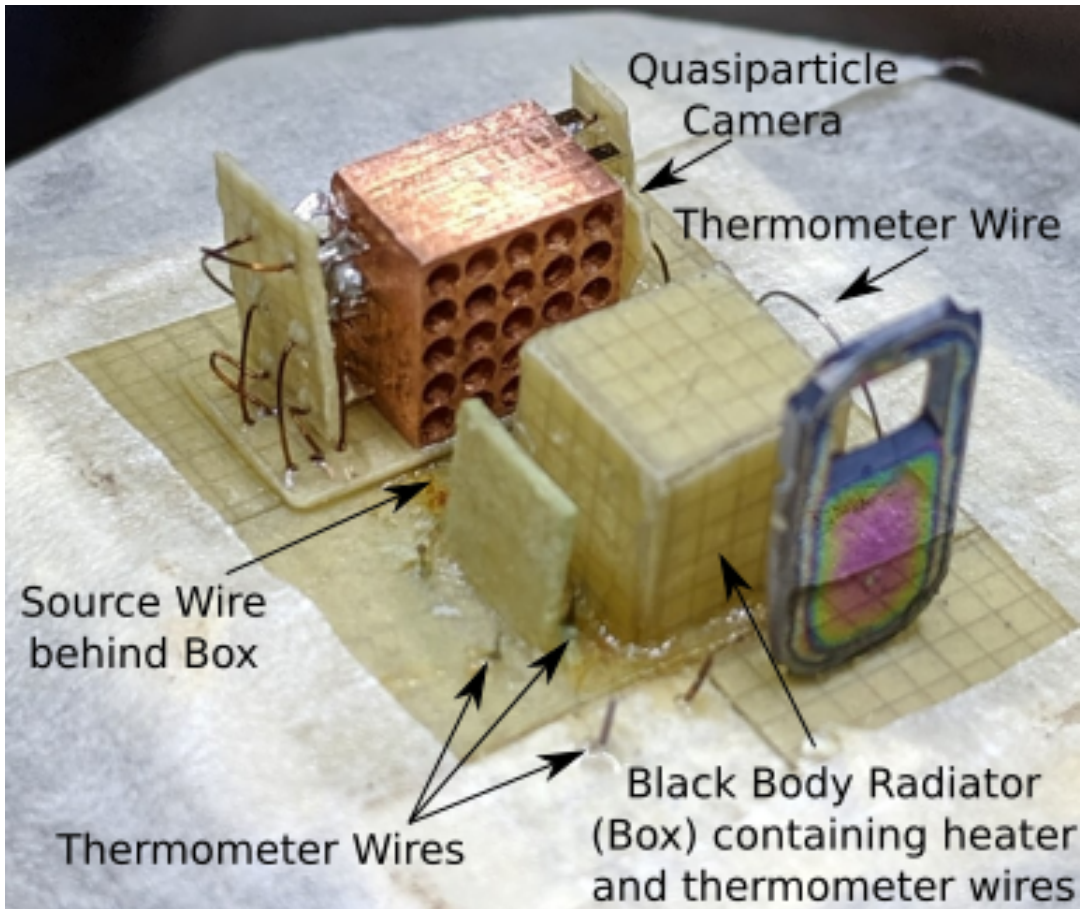


FIGURE 6.1: A picture of the experimental cell. The quasiparticle camera is on the upper centre with the blackbody radiator in front of it. A source wire is used to create turbulence for experiments and a heater wire to heat the box. Other wires are used for thermometry.

recording the light reflected from the object, or by observing the shadow of light from the object. In $^3\text{He-B}$ the process of getting a 'light' source and recording the picture is more complicated but the basic principle remains the same.

The actual 'light' source in superfluid $^3\text{He-B}$ is a black box radiator (BBR) that can emit a stream of quasiparticles[22, 111, 112]. The box, shown in fig. 6.1, is made of stycast impregnated paper. At $150\ \mu\text{K}$ the walls hardly produce excitations into $^3\text{He-B}$ and can be considered as a thermal vacuum. Inside the box there are two vibrating wires that operate as a heater and thermometer respectively. The heater wire is excited so that it moves at a sufficient speed to break Cooper pairs and creates quasiparticles in the fluid. These are reflected around the box and thermalise before eventually reaching a small orifice of diameter $0.3\ \text{mm}$ and escaping the box as a beam towards the camera located $2\ \text{mm}$ away.

The power of the beam exiting the box can be deduced from[22]:

$$\dot{Q}_B = 2(\langle nv_g \rangle / 4) \tilde{E} A \quad (6.1)$$

where the factor of two accounts for the hole and quasiparticle branches, $\langle nv_g \rangle$ is the quasiparticle flux from section 3.3.2, A is the area of the orifice and $\tilde{E} = k_B T + \Delta$ is the average energy of the quasiparticles. In the steady state the power exiting the box is equal to the sum of the powers entering from the heater wire \dot{Q}_{hw} , through the orifice and the heat leak from the walls. In practice we assume that the heat entering through the orifice is negligible. The damping width of the thermometry wire can be found from eq. (3.34) which we can combine with eq. (6.1) to find:

$$\Delta f_2 T \tilde{E} = \gamma' \frac{2dp_F^2}{\pi m A k_B} \dot{Q}_B \quad (6.2)$$

If we then subtract the measured value of $\Delta f_2 T \tilde{E}$ at zero heating from $\Delta f_2 T \tilde{E}$ with heating, we find the width parameter W that has no contribution from ambient heat leaks. Thus the width parameter for the box is:

$$W_B = (\Delta f_2 T \tilde{E}) - (\Delta f_2 T \tilde{E})_0 \quad (6.3)$$

$$= \gamma' \frac{2dp_F^2}{\pi m A k_B} \dot{Q}_{hw} \quad (6.4)$$

which shows that W is linear with the power; so that we can write:

$$\dot{Q}_B = c_B W_B \quad (6.5)$$

where c_B is the constant of proportionality for the box which is a combination of the above constants. The value of c_B can be found for the BBR by measuring the applied power against the measured width parameter W_B .

6.1.2 A Quasiparticle Camera

Figure 6.1 shows the camera in front of the box, with the source wire capable of generating turbulence and quasiparticles between them (discussed below). A photograph of the camera is shown in fig. 6.2. It is made up from a square copper block with five tuning fork arrays (A to E) of five tuning forks (1 to 5) each which make up 25 pixels. Each fork in a array has dimensions $D = 90 \mu\text{m}$, $W = 50 \mu\text{m}$ and $T = 90 \mu\text{m}$ and length L . The lengths of each fork in the arrays (picture shown in fig. 3.3) are slightly different along the array, chosen so that the resonances of the forks are well separated. Likewise the arrays are identical except for the fork lengths so that all 25 forks have

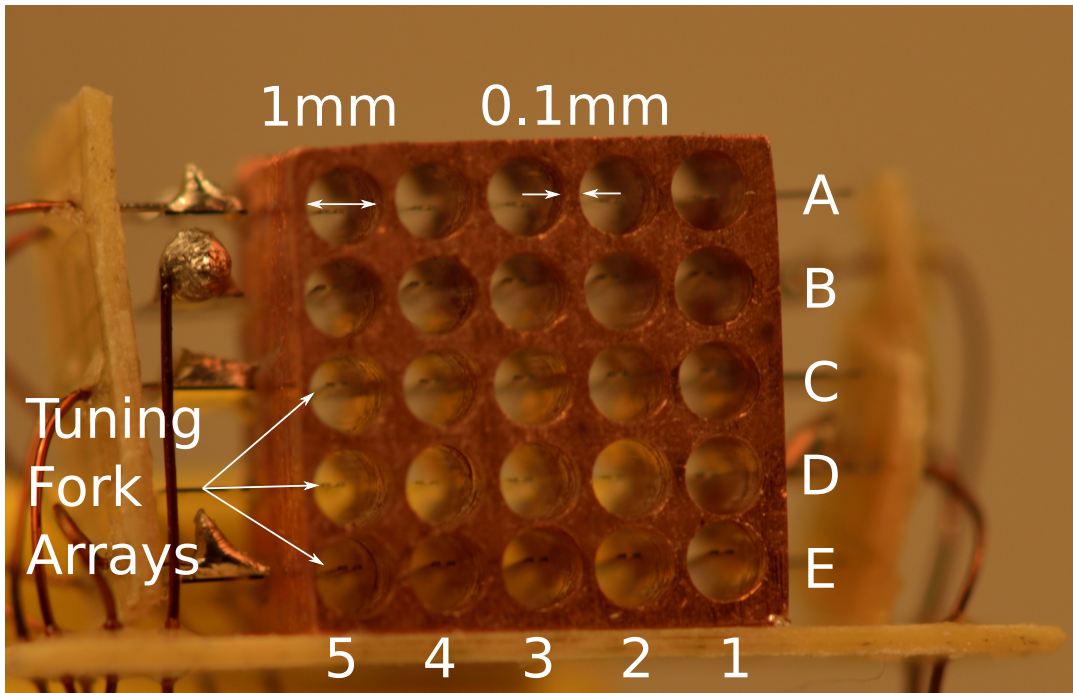


FIGURE 6.2: A picture of the camera before being mounted in the cell, with indicated rows and columns.

distinct resonances to prevent cross-talk between the forks and experimental wiring. The fundamental resonances of the forks range from 20 kHz to 40 kHz.

The fork centres are separated along the arrays by a distance of 1.1 mm. They are placed in a 5.7 mm by 5.7 mm by 4.0 mm copper block. The block has 25 drilled through cylindrical cavities of 1.0 mm diameter. Inside each cavity there is a fork from one of the arrays.

Unfortunately arrays B and C are shorted at low temperatures so can only be operated one at a time. A total of 20 SR830 lock-in amplifiers and 20 Agilent signal generators excite and measure the forks in the manner shown in fig. 6.3. Groups of five signal generators have their signals added together by a summation amplifier with active attenuation (typically 60 dB or 80 dB) before exciting one of the arrays. The signal of the array can then be picked up by a bank of 5 lock-in amplifiers after a 1 MVA^{-1} current voltage converter steps up the response. A NI PXIe-1073 data acquisition instrument (DAQ) is used to measure the demodulated in-phase and quadrature components from the lock-in amplifiers for real time measurements.

While cooling down the fridge the forks were first swept in vacuum at 4.2 K to find the vacuum frequency and intrinsic widths at low temperature. After condensing ^3He into the experimental cell the forks were frequency swept at each successive temperature step. This checked that the forks were not broken during the cooldown

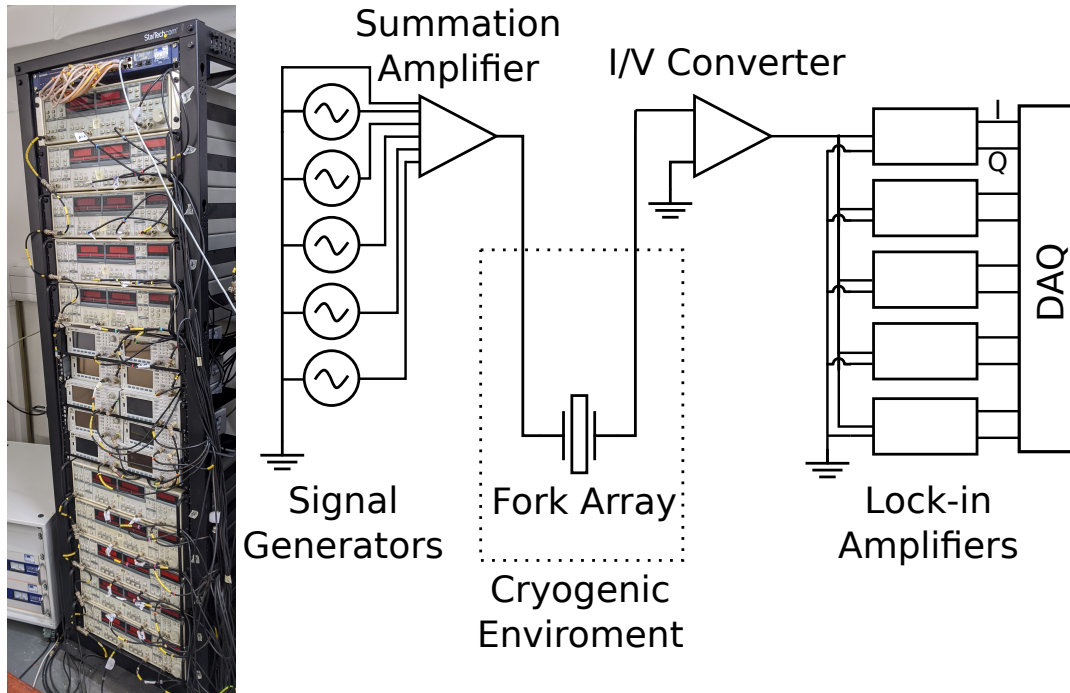


FIGURE 6.3: A picture of one of the two equipment racks used to measure the fork arrays. On the right an electronic schematic shows the complete setup for one fork array. Five signal generators emit signals which are combined by the summation amplifier with active attenuation of 60 dB or 80 dB. The signals then drive all 5 forks along the array. The responses are then amplified by an I/V converter and then measured by 5 lock-in amplifiers. The lock-in amplifiers output the demodulated signal into in-phase I and quadrature Q components into a data acquisition instrument (DAQ) for real time measurements. Note the reference signals are not shown, for further details read section 3.1.2.

and provided data for other experiments.

As discussed in section 3.3.2 the velocity field about the forks causes Andreev reflection of quasiparticles. The force of the quasiparticle flux on the fork can be described by eq. (3.33). The forks can be operated at high and low velocity modes. At low velocities we have already seen from eq. (3.34) that the damping from the quasiparticle flux is linear. At higher velocities the damping becomes non-linear as more quasiparticles are shielded by the flow field. In this regime the forks are highly sensitive to small changes in the quasiparticle flux, increasing their effective sensitivity. Typically in measurements we used high velocities to exploit the enhanced sensitivity of the non-linear damping regime.

In superfluid $^3\text{He-B}$ we can derive the power received at a pixel in a similar manner for the black box radiator power distribution. Each pixel works as a BBR in its own right. By using the width of the pixel's tuning fork we obtain:

$$\dot{Q}_p = c_p W_p \quad (6.6)$$

where \dot{Q}_p is the received power at the pixel, c_p the pixel's constant of proportionality and W_p the width parameter for the pixel measured by the tuning fork. Note that with no independent heater and thermometer it is impossible to independently measure the inputted power and width parameter of the pixel, so there is no direct measurement of c_p . We however expect that c_p is a constant and so it can be deduced from the ratio of \dot{Q}_p to \dot{Q}_B using the width parameters.

6.1.3 Theoretical Prediction of the Black Box Radiator Beam

For an ideal box a theoretical predication for the power of the beam carried to the pixels can be found by considering the cosine law for a light emitting disk. For a central pixel the flux ratio of the power received to the emitted beam power is:

$$\frac{\dot{Q}_P}{\dot{Q}_B} = \frac{1}{\pi} \int_0^{2\pi} \int_0^{\arcsin(\frac{a}{R})} \cos \phi \sin \phi \, d\phi \, d\theta = \left(\frac{a}{R}\right)^2 \quad (6.7)$$

where R is the distance from the BBR to the camera and a the pixel radius shown schematically in fig. 6.4.

At a non-central pixel the quasiparticle fraction becomes:

$$\frac{\dot{Q}_P}{\dot{Q}_B} = \frac{c_P W_P}{c_B W_B} = \left(\frac{a}{r_p}\right)^2 \cos^2 \phi_p = \left(\frac{a}{R}\right)^2 \cos^4 \phi_p \quad (6.8)$$

where r_p is distance from the pixel's face centre to the black box orifice centre, ϕ_p the angle subtended by the centre of the pixel's face to the centre of the orifice's face.

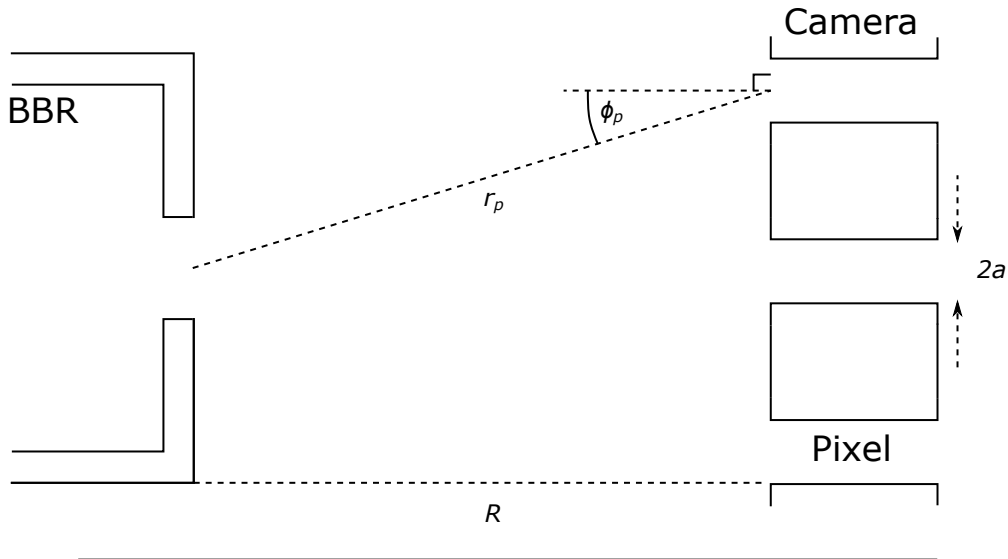


FIGURE 6.4: A schematic of the camera and BBR (not to scale). Important dimensions are highlighted.

Figure 6.5 shows the prediction of eq. (6.8) for our camera.

Of course only a small fraction of the emitted quasiparticles will be incident on a fork. Some hit the cooper matrix inbetween the holes and are effectively lost when reflected off. At a central pixel eq. (6.7) it is estimated that 6.2% of emitted quasiparticles are incident. A fraction of these will be able to travel through the tube geometry and will not be detected by the fork. Furthermore some will hit the fork behind the sensitive tip and also will not contribute to the damping. We can conclude that the central pixels will under estimate the incident flux.

At outer pixels the situation is simpler. Even if the incident quasiparticles do not hit the fork immediately the incident angle is such that they can be expected to contribute to the fork's damping from the reflection(s) off the pixel's walls. So eq. (6.8) should give a better estimation of the beam's power than at the central pixels.

6.1.4 Simulations of the Quasiparticle Beam

In the theoretical prediction of the quasiparticle beam we assume that the BBR emission can be approximated as a disk source of light. In order to further test this hypothesis against the measurements we simulated the behaviour of 10^6 quasiparticles placed in the cylindrical geometry of the orifice. They were evenly distributed across the inlet of the orifice as independent point-sources. The simulation included the scattering of the quasiparticles off the orifice walls. We then assumed that if the quasiparticles scattered off a pixel wall within a certain distance from the front face of the camera they would be detected by that pixel's tuning fork.

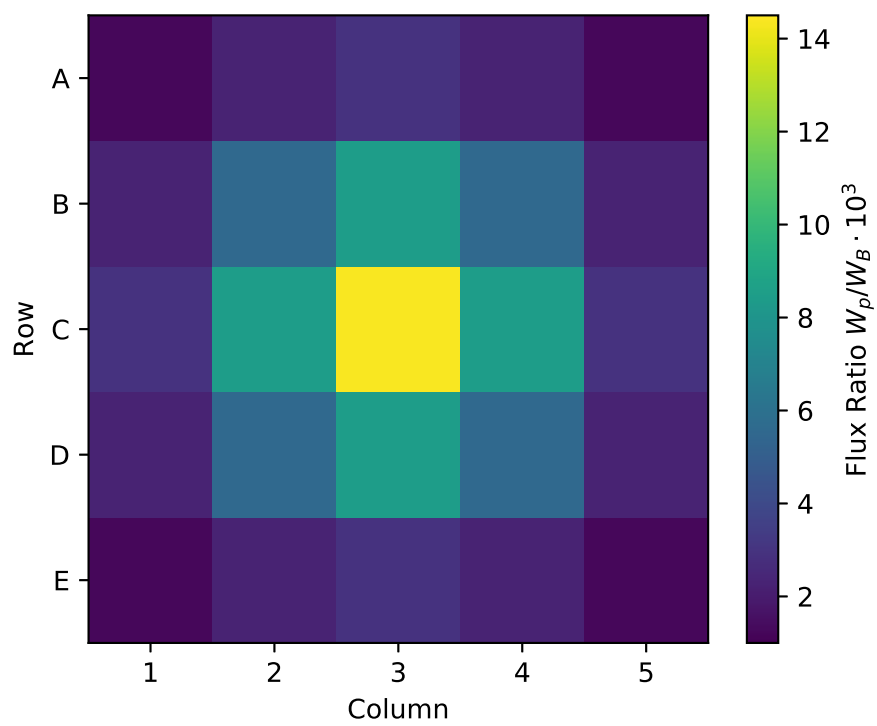


FIGURE 6.5: Analytical prediction of the beam's quasiparticle flux profile on the camera from eq. (6.8).

The scattering mechanism could be changed to simulate completely specular, diffuse or inbetween scenarios. The post-scatter trajectory was modelled by randomly deciding the direction within a solid angle (centred along the specular reflection angle) determined by a specularity coefficient. A coefficient of 1 would give completely specular reflections while 0 gave the diffuse case. Values inbetween would control the size of the scattering solid angle. No attempt was made to model the surface roughness and this may affect the scattering. Figure 6.9 shows the results of the simulation, and the results are compared against measurements in section 6.1.6.

6.1.5 Measurement Scheme

For actual measurements a resonance tracker program would monitor the resonances of the forks and thermometry wires simultaneously. The program would then record the resonant frequency, width and height of the resonators for later analysis. Since arrays B and C could not be simultaneously operated measurements would be repeated twice after swapping B to C or vice versa.

While the resonance tracker was running, experiments could be performed on the source wire or the BBR heater wire as described below. This would be either an amplitude sweep as described in section 3.2.2 or a pulsed sweep.

Pulsed sweeps are similar to amplitude sweeps except that at each drive the resonator would be held at the specific excitation for a longer time, such as 50 s, while amplitude sweeps stay at a single drive for a few seconds. After each pulse the drive was dropped down to 0 V and the cell would be allowed to relax for a while (100 s or so) to return to base temperature before the next pulse is applied. The pulsed sweeps allowed measurements to be averaged to decrease the scatter compared to an amplitude sweep. Furthermore pulsed measurements offer a distinct advantage in that they allow direct comparison with the beam on and off one after another. This meant that esoteric heating, an example of which is shown in fig. 4.6, to the cell during a sweep could be effectively accounted for by averaging or discarding heating spikes from radiation.

Data Corrections and Calibrations

To accurately measure the flux at each pixel the damping width of the pixel's tuning fork resonance must be known accurately. The tracking program uses a measured HWD value to find the width from the measured height of the fork. In analysis we can remove the intrinsic width of the fork to find the thermal width and hence the power received at that pixel. High velocity data requires a non-linear correction to account for the reduction of damping due to Andreev reflection (see section section 3.3.2) to find the true thermal width.

We can deduce the value of γ for the fork using the known value for a wire γ . If we find the ratio of the thermal width for the fork Δf_2^F and wire Δf_2^W we see that:

$$\Delta f_2^F = \frac{W}{d} \frac{m_W}{m_F} \frac{\gamma_F}{\gamma_W} \Delta f_2^W \quad (6.9)$$

where m_W and m_F is the mass of the wire and fork respectively and W here is the fork's tine width; γ_W and γ_F is the value of γ constant for the wire and fork respectively. A plot of thermal widths of the fork against the wire then allows us to find the ratio of γ_W to γ_F and then calibrate γ_F .

After the experimental run during data analysis we noticed that localised overheating of the forks caused the thermal widths of the forks to be wrongly calculated. We corrected this by looking at eq. (3.34), from which we see that high velocities shield the fork from thermal quasiparticles, causing a fall in the measured width (for a velocity below Landau's velocity) despite the temperature of the fluid remaining constant throughout. We can recover the true temperature with the correct values of λ and the intrinsic width. The constant λ has been pre-calibrated for the forks from previous work by fitting force velocity curves for the fork[23]. This then allows us to fit the intrinsic width of the fork by comparing the calculated temperature of the forks against velocity. For the ideal calibration the temperature remains constant for all measured velocities of the fork.

6.1.6 Measurements of the Quasiparticle Beam

To perform the measurements of the profile of quasiparticle beam as a function of the emitted power the heater wire in the BBR was swept, first with an amplitude sweep and then a pulsed sweep. In analysis, the width parameters for each pixel and the BBR thermometer were calculated, and the flux found via the ratio of W_p/W_B for each pixel.

Figure 6.6 shows the results for the quasiparticle beam plotting the ratio of width parameters for pixels and the BBR from eqs. (6.5) and (6.6) against the power deposited into the box by the heater wire ($\dot{Q}_B = Fv$). We can see that the flux ratios hold constant against the BBR power over a few orders of magnitude until a power of 80 pW is reached. Below 10 pW value the signal level becomes comparable to experimental noise and the ratios appear to be no longer constant.

Figure 6.7 shows similar measurements to fig. 6.6 but the heater wire was pulsed instead. Likewise we can see that the width parameter ratio holds constant over few orders of magnitude verifying the method. The improved averaging of the pulsed sweep however allows us to see that the flux ratios hold constant for a further order of magnitude until about 2 pW as compared to the amplitude sweep data in fig. 6.6.

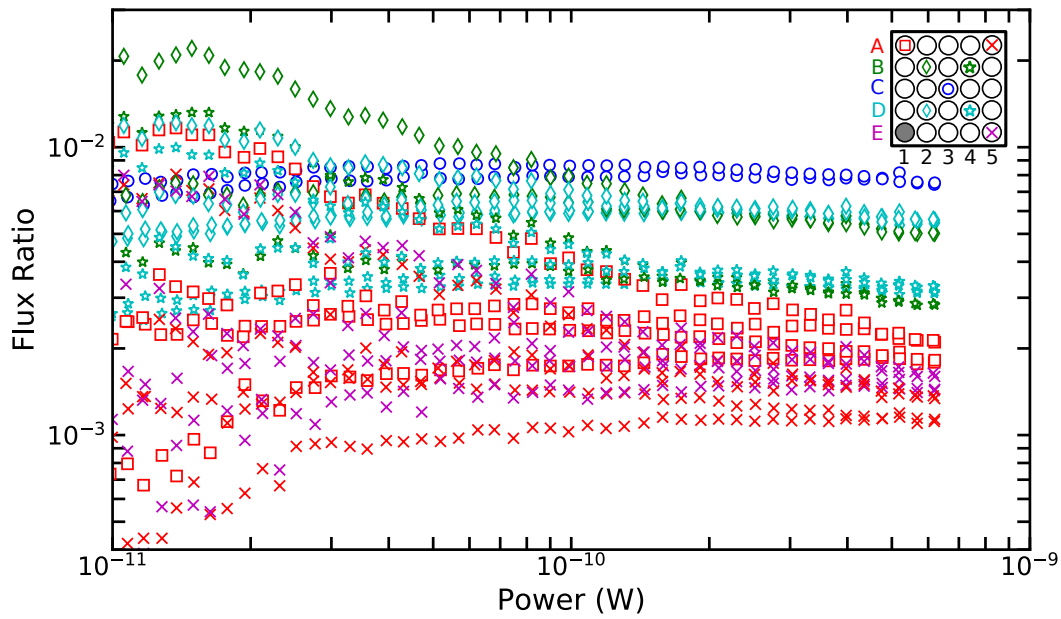


FIGURE 6.6: A semi-log plot of the ratio of the pixel and BBR width parameters against the BBR power. In this data the heater wire in the BBR was amplitude swept. Different colours represent different camera rows while different symbols represent different columns.

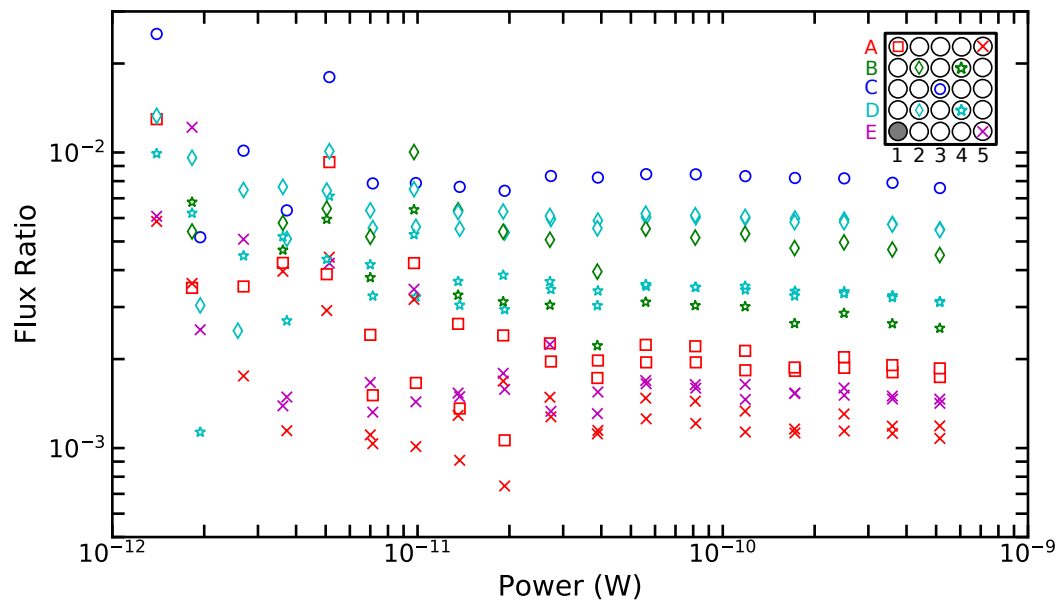


FIGURE 6.7: A semi-log plot of the ratio of the pixel and BBR width parameters against the BBR power. A pulse sweep was used to drive the BBR heater wire

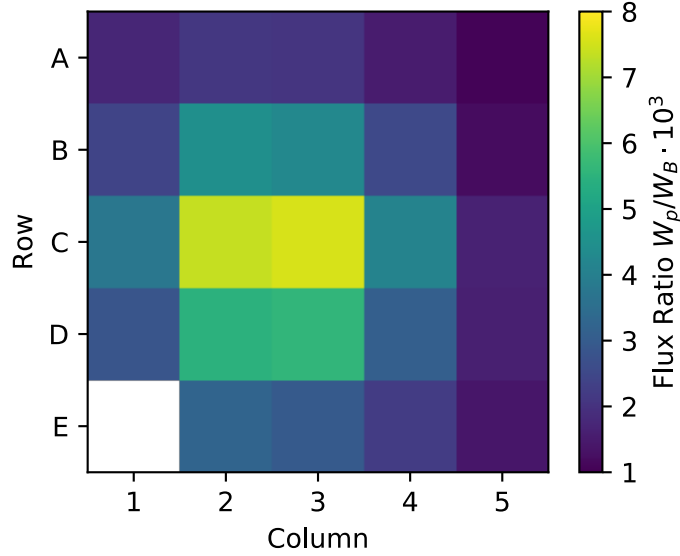


FIGURE 6.8: An image of the quasiparticle beam using the data in fig. 6.7.

The essentially constant relationship between the received and emitted ratios means that the beam source can be largely treated like a black-body radiator, in that the beam's power and direction are independent of each other. It is likely that this relationship would continue to lower powers but we are hitting the experimental limits of noise due to the comparatively low fraction of beam power received at each pixel. Longer averaging times for the pulsed sweeps would decrease the experimental scatter in the data.

Using the data in fig. 6.7 we can image the quasiparticle BBR beam in fig. 6.8 as a heat graph and plot by column in fig. 6.9. We can see using both of these plots that the beam is symmetrical and offset from the center of the camera, being aligned slightly to the left by 0.47 mm, and down by 0.23 mm, as we look at the data. Figure 6.9 also shows analytical prediction from eq. (6.8) and simulated prediction of the beam for comparison.

From the analytical model in section 6.1.3 we see that rows A and E are in reasonable agreement with the prediction with $c_p/c_B = 0.23$. With $c_p/c_B = 0.23$ we expect 1.4% of the quasiparticles to be detected by the central pixels down from 6.2% incident. The measured flux is about a factor of two lower than the expected ratio which we ascribe to quasiparticles travelling straight through the pixels undetected as we discussed.

The simulation gives a better agreement to both the outer and central pixels. It

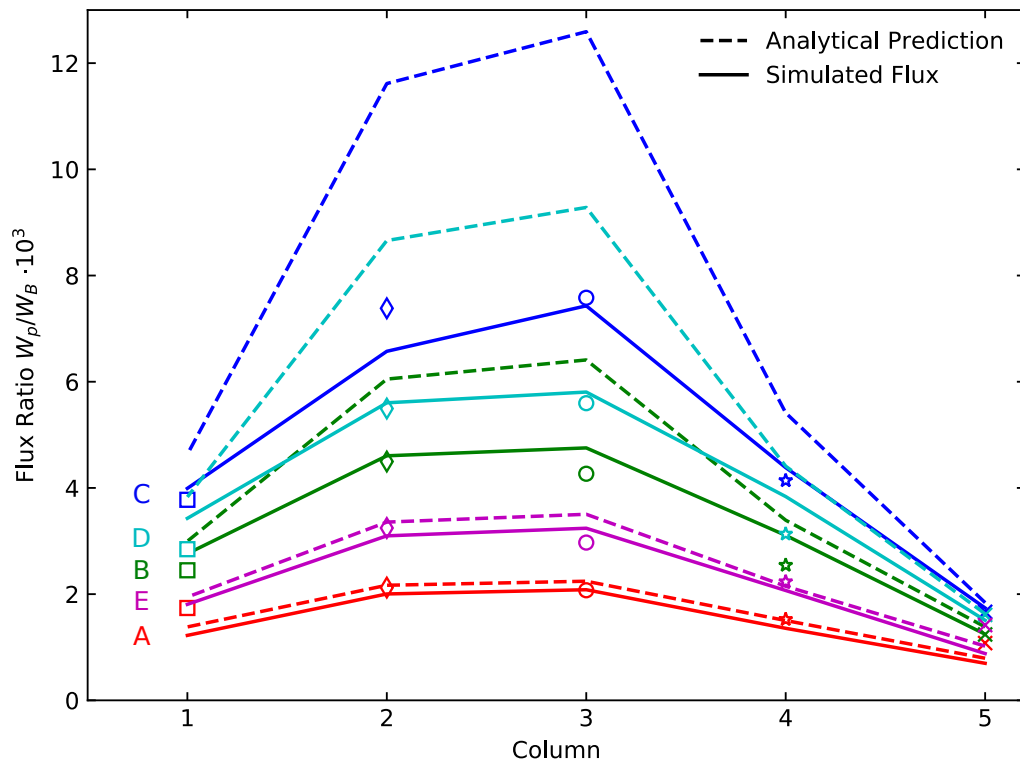


FIGURE 6.9: The quasiparticle flux by column for the different rows of the camera from the data in fig. 6.7. The solid lines show the results of a simulation of the quasiparticle flux with $c_p/c_B = 0.19$ while the dashed lines show an analytical prediction using eq. (6.8) and $c_p/c_B = 0.23$.

is worth noting that both fully diffuse and specular simulations were tested against the data. It was found that the specular simulation was similar to the analytical model and described the outer pixels well but not the central pixels. Conversely the diffuse scattering model described the central pixels well but was low on the periphery. Hence in fig. 6.9 we plot the simulation with scattering in between the two extremes with specular coefficient of 0.77 and $c_p/c_B = 0.19$. This simulation describes both the central and outer pixels fairly well. This suggests that the measured data supports that quasiparticle scattering at walls in $^3\text{He-B}$ is neither fully diffuse or specular. Also worth considering is that the walls will be coated with a 3 atomic layer thick film of ^3He , that will likely effect the scattering properties of the wall. A future experiment could investigate this property by using ^4He to plate the walls and change the scattering properties.

6.2 Imaging Quantum Turbulence with Quasiparticles

6.2.1 Detecting and Creating Vortices

Though the camera can take a picture of the light source and it is instructive and necessary to do so, the source wire can provide something to picture. Firstly moving a wire through $^3\text{He-B}$ will break Cooper pairs and create quasiparticles. It will also create vortices in the superfluid that create a vortex tangle of quantum turbulence[15].

Figure 6.10 shows a typical force velocity curve for the source wire. At low velocities we see a linear relationship between the force and velocity. From a velocity of about 1 mm s^{-1} the behaviour becomes noticeably non-linear and a step in the force elicits a larger increase in velocity. This is due to the superflow about the wire causing the Andreev reflection of thermal quasiparticles, effectively shielding the wire, decreasing the damping (see section 3.3.2). After this feature at a velocity of about 7 mm s^{-1} we see that the line rapidly flattens off due to massively increased damping from the creation of quantum vorticity and pair breaking.

The wire's velocity for pair breaking is quite different from Landau's velocity in ^3He , which is 27 mm s^{-1} . This is because potential flow about a cylinder causes a factor of 2 flow enhancement at the two lines that are perpendicular to the motion[62]. The wire causes pair breaking into the normally bound states about the wire and as long as there is an available energy state in the bulk these are emitted. In the wire's frame these excitations have an energy $2p_F v$ and are emitted at an angle θ compared to the velocity. The minimum energy of the bulk states are then given by $\Delta - p_F v \cos \theta$ [22]. The minimum energy then occurs where $\cos \theta = 1$, and by setting

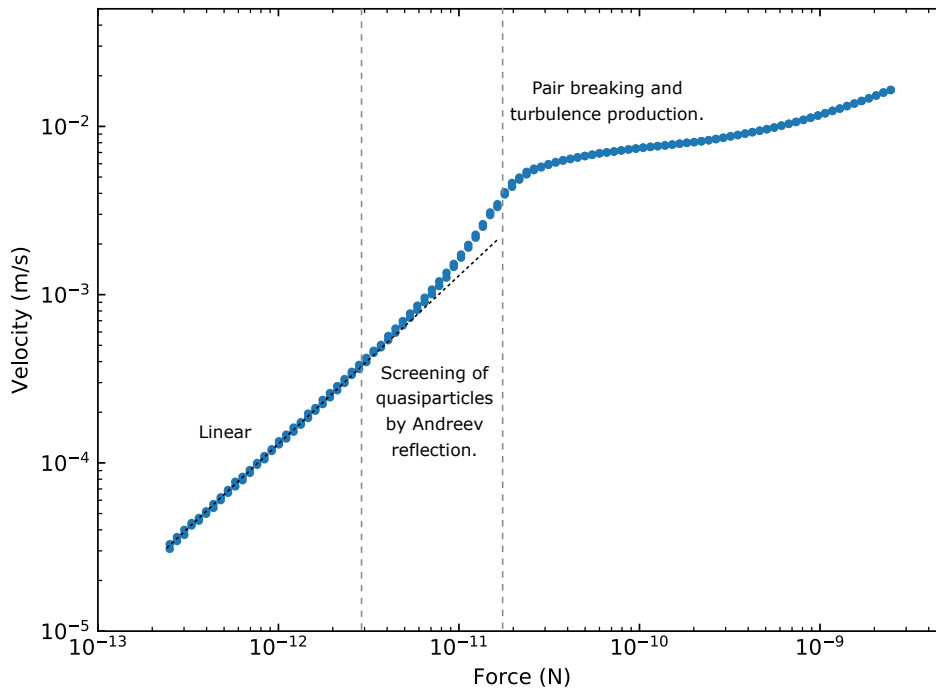


FIGURE 6.10: A log-log plot of a force velocity curve for the source wire at a base temperature of $150\ \mu\text{K}$. At the lowest velocity the curve is linear and then gently curves upwards due the shielding of quasiparticles by Andreev's reflection. Finally at about $7\ \text{mm s}^{-1}$ the curve's gradient massively decreases due to damping from quantum turbulence and pair breaking.

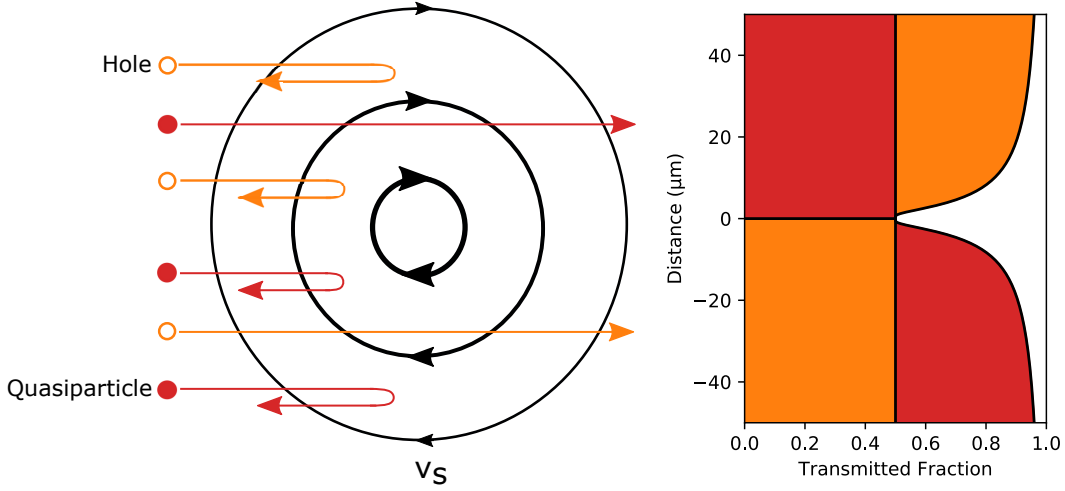


FIGURE 6.11: (Left) An illustration of how incoming quasiparticles (holes in orange open circles and quasiparticles in red circles) are Andreev reflected by the superflow about a vortex. (Right) Transmitted fraction of quasiparticles by a quantum vortex from eq. (6.14) relative to the center of the vortex. On the top half of the vortex holes are retro-reflected into quasiparticles while quasiparticle can travel unimpeded, and vice versa on the bottom half of the vortex. Behind the vortex there is a ‘shadow’ of quasiparticles.

the excitation energy equal to the minimum bulk energy we find[22]:

$$v_c = \frac{\Delta}{3p_F} = \frac{v_L}{3} \quad (6.10)$$

where v_c is the critical velocity to create an excitation.

The vortices created by the wire are topological defects in the wavefunction of the fluid. It is currently poorly understood how or if the quasiparticles interact with a vortex core. We do know that a quasiparticle can interact with a velocity field, such as the superflow around a vortex. Using eq. (2.19) we can find the velocity about a vortex as:

$$v_s(r) = \frac{\hbar}{2m_3r}. \quad (6.11)$$

As discussed in section 3.3.2 a superfluid velocity field shifts the dispersion curve of $^3\text{He-B}$. Shifting the dispersion curve causes the retro-reflection of quasiparticles and holes by Andreev reflection about the vortex as illustrated by fig. 6.11. Quasiparticles travelling anti-parallel to the flow are unimpeded while holes can be reflected if they have insufficient energy to travel through. On the other side of the vortex the process works vice-versa with holes being unimpeded and quasiparticles getting retro-reflected.

Figure 6.11 also shows the flux shadow of quasiparticles behind the vortex. We can work out the fraction of quasiparticles that passes through, by considering similar arguments to chapter 2. We need to integrate over the total allowed states with energy above $\Delta + p_F v_s$ [113]. Therefore the transmitted flux of particles is:

$$\langle n v_g \rangle_t = \frac{1}{2} \langle n v_g \rangle_i \int_{\Delta + p_F v_s}^{\infty} f(E) g(E) v_g(E) dE \quad (6.12)$$

$$\langle n v_g \rangle_t = g(p_F) k_B T \exp\left(-\frac{\Delta + p_F v_s}{k_B T}\right) \quad (6.13)$$

The fraction of quasiparticles that are transmitted can be found from the incident flux as:

$$f = 1 - \frac{\langle n v_g \rangle_t}{\langle n v_g \rangle_i} = 1 - \exp\left(-\frac{\hbar p_F}{2m_3 r k_B T}\right). \quad (6.14)$$

and is plotted on right hand side of fig. 6.11. Reflected quasiparticles will then retrace their path back to the BBR [114].

The right hand side of fig. 6.11 shows that there is still an appreciable drop of about 5% in the flux about 50 μm away from the core. Quantum turbulence is made up of a tangle of vortex lines. The larger the vortex line density the more likely that a quasiparticle will be reflected, further reducing the flux of particles. By then comparing the images with and without turbulence the shadow of turbulence can be identified and we can image quantum turbulence.

6.2.2 Measurements of the Source Wire Beam

The next measurement was the beam of quasiparticles created by the source wire itself. The BBR heater was left off and the source wire was swept with amplitude sweeps and the new pulsed sweep methods. This measurement is necessary so that we can account for the beam during later turbulence measurements with the BBR and source wire switched on.

Figure 6.12 shows the width parameter of the pixels plotted against the measured velocity of the source wire during an amplitude sweep. We can see that all the pixels are flat until a velocity about 6 mm s^{-1} where the central pixels notice an appreciable flux. Initially the beam is fairly narrow with pixels around the periphery remaining mostly unmoved until about 11 mm s^{-1} where they too start to increase. We note a large amount of noise due to the low tuning fork velocity used decreasing the relative sensitivity of the forks to the quasiparticle flux.

We did measure the B array to include in the data, unfortunately the B array data was not comparable to the C array data. With the measurements between the other arrays (A, D and E) showing different heights, albeit with the same trends. We

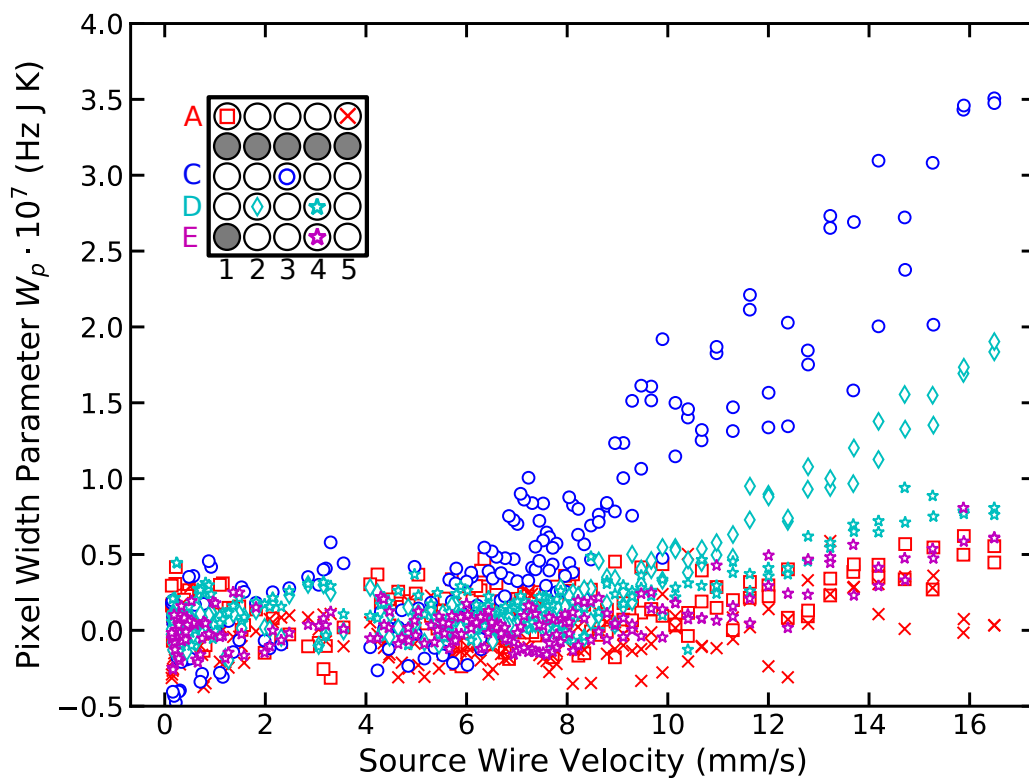


FIGURE 6.12: Dependence of the measured width parameter of camera pixels against the velocity of the source wire while the BBR beam was off. In these measurements an amplitude sweep was used to drive the source wire.

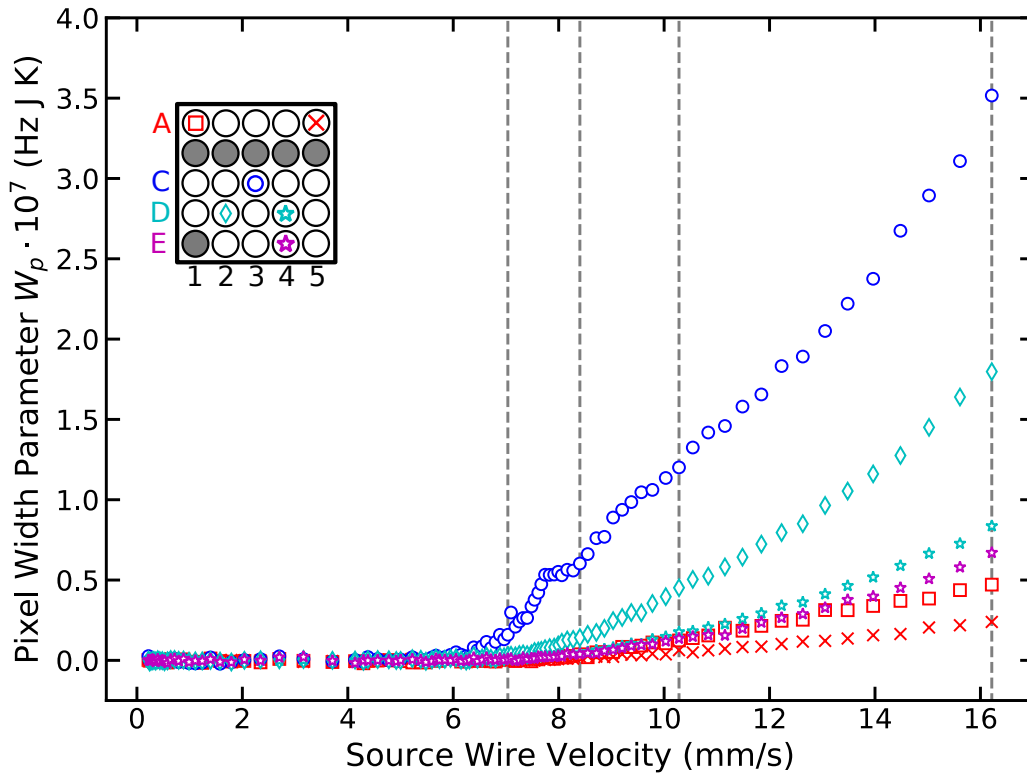


FIGURE 6.13: The dependence of the measured width parameter of the camera pixels against the velocity of the source wire while the BBR beam was off. In these measurements a pulsed sweep was used to drive the source wire. The grey dashed lines indicate the velocities used to for the creation of colour map graph based images of the beam in fig. 6.14.

suspect this was due to localised overheating during this measurement from a yet unidentified source. This did not affect other measurements involving the B array. It is also pertinent to note that connecting the B array to the lock-in amplifiers and signal generators causes the temperature to rise on all cell thermometers.

Figure 6.13 again shows the width parameter versus the source wire velocity but for a pulsed sweep. The main features are essentially similar to fig. 6.12 but we can note some differences due to the pulsed sweep at a high tuning fork velocity vastly increasing the sensitivity of the device. The peripheral pixels see a noticeably increased quasiparticle flux at a velocity of 8 mm s^{-1} , much lower than is seen in fig. 6.12. This is probably due to significantly decreased noise in the measurements allowing finer details to be visible.

We can see a plateau region on C3 where the the width parameter stops rising and holds steady from 7.7 mm s^{-1} to 8.3 mm s^{-1} before continuing with the trend. One

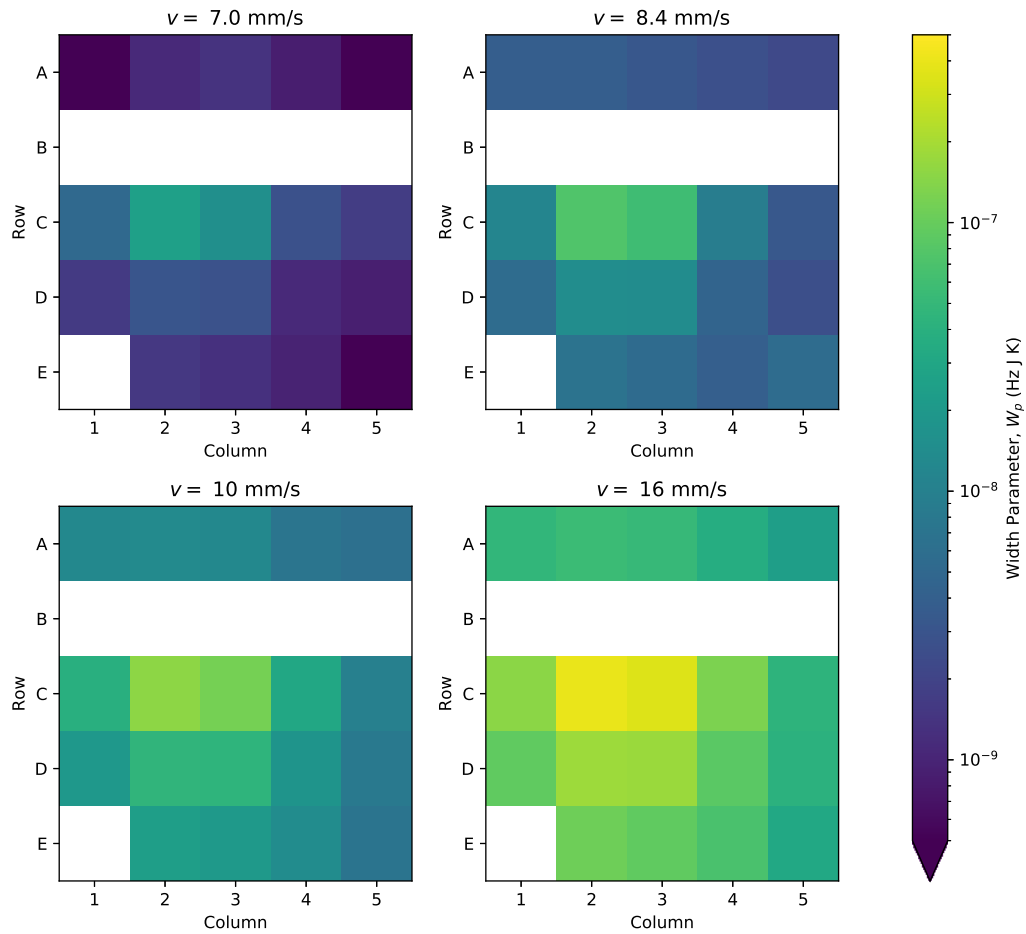


FIGURE 6.14: Heat graph based camera pictures on a log scale of the measured pixel width parameters of the source wire beam while the BBR beam was off at selected velocities. The data was taken from the pulsed sweep shown in fig. 6.13 at the grey dashed lines. Note that B array and E1 were not measured (see text).

might not expect such behaviour, and would instead expect a steady increase in the emitted beam power as the source wire velocity increases. Before the plateau we also note that the gradient is increased compared with the regular trend of the data. It is unknown what effect might cause this, although it could be related to vortex ring production on the source wire[115] where a vibrating wire can jump between two velocities.

Figure 6.14 shows colour map graph based plots of the source wire beam at selected velocities of the pulsed sweep data from fig. 6.13. We can now clearly see that the two central pixels receive the vast majority of the quasiparticle flux at all velocities. The beam is initially narrow on the two central pixels but broadens out at

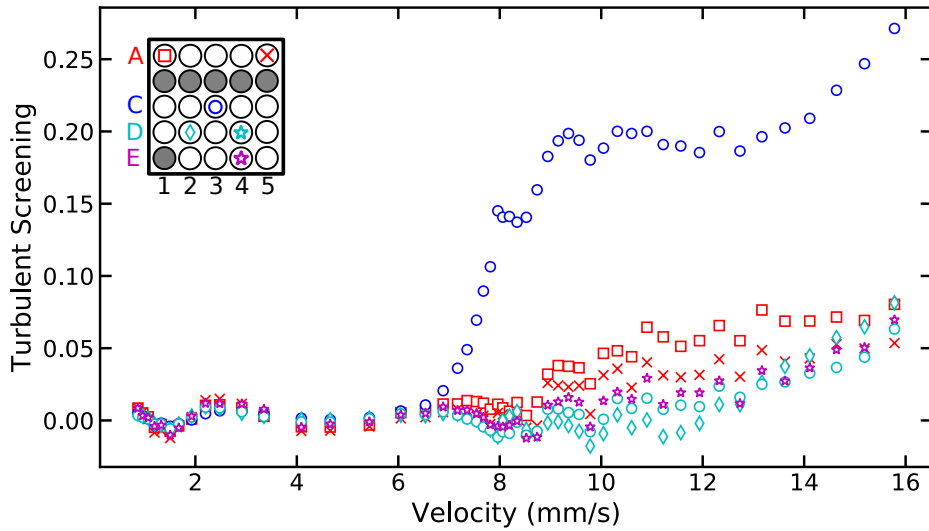


FIGURE 6.15: Fractional shielding of quasiparticles against the velocity of the source wire. The source wire was driven by an amplitude sweep.

higher velocities to the periphery which agrees with previous measurements[22].

6.2.3 Measurements of Quantum Turbulence

Here both the heater wire in the black box and the turbulent source wire were used. The beam of quasiparticle would then be incident on the vortex tangle and then the camera. In measurements the BBR heater was left on at a constant excitation to provide a constant beam. In the beam the source wire was swept by amplitude and pulsed sweeps again.

Figure 6.15 shows the fractional shielding of the pixels against the source wire velocity during an amplitude sweep of the wire. The pixels are flat until a source wire velocity of about 7 mm s^{-1} is reached. At which point the central pixels start to show a quasiparticle shadow developing. Shortly after 9 mm s^{-1} most pixels in the A and C arrays shows evidence of screening. The forks D2 however does not show screening. At about 12 mm s^{-1} peripheral pixels outside the wire loop in arrays D and E begin to as well. The pixels within the loop however show no evidence of screening until they also rise at a velocity of about 15 mm s^{-1} .

Figure 6.16 shows similar behaviour to fig. 6.15. The data however are improved by the averaging and better comparison of the data by the pulsed sweep.

Figure 6.17 shows colour map graph images of the fractional screening of the pixels by quantum turbulence at selected source wire velocities. We can now clearly

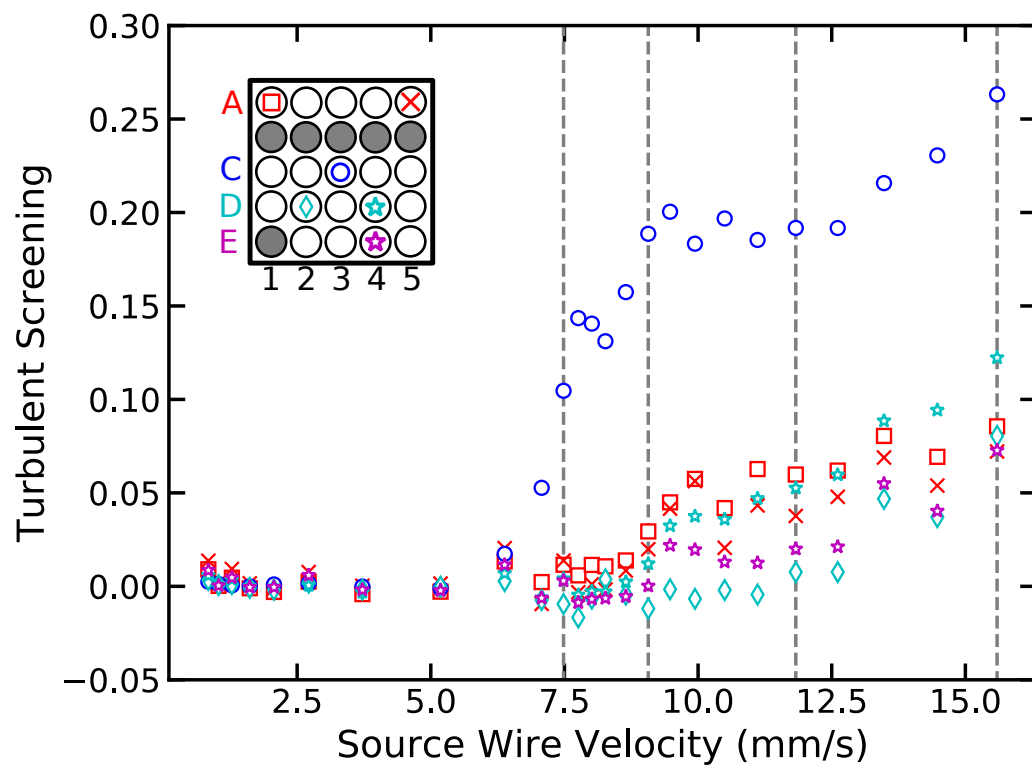


FIGURE 6.16: Fractional shielding of quasiparticles against the velocity of the source wire. The source wire was driven by a pulsed sweep. The grey dashed lines indicate the velocities used to for the creation of colour map graph based images of the beam in fig. 6.17

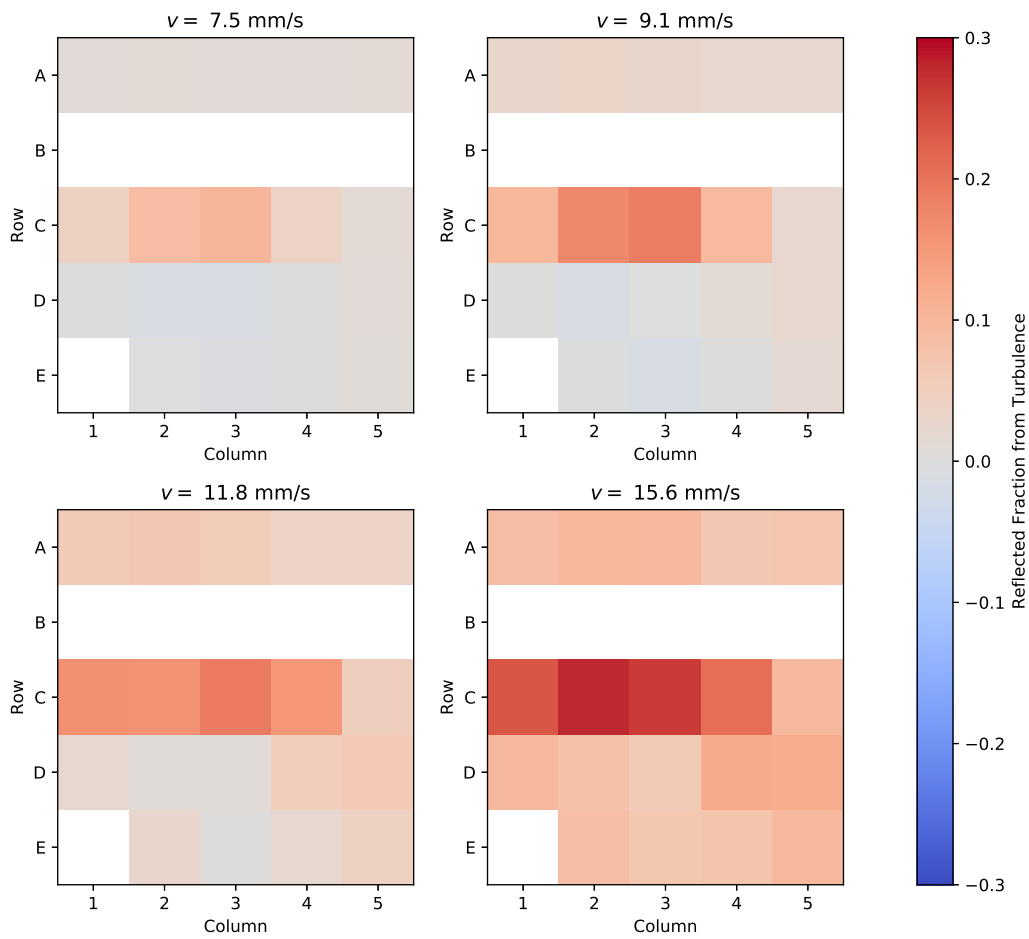


FIGURE 6.17: A series of heat map like images of the fractional screening of the quasiparticle flux by quantum turbulence. The data was taken from the pulsed sweep shown in fig. 6.16 at the grey dashed lines.

see the behaviour just discussed, in that the turbulence initially forms above the wire and does not appear below the wire until much higher velocities ($>15 \text{ mm s}^{-1}$) are reached.

The reason that turbulence appears above the wire as seen in fig. 6.17 is not forthcoming. One would expect that turbulence would be homogeneous about the wire since the whole wire moves at the same velocity. It could be that the vortex mill production sites are mainly situated on top of the wire, although one would expect the roughness to be approximately constant all about the wire.

6.3 Conclusions

We have demonstrated the successful imaging of a quantum vortices in superfluid ^3He by using ballistic quasiparticles inherent to the fluid. Furthermore we have shown we can picture images of the quasiparticle beam from a BBR and the source wire. This shows that in the ballistic regime of superfluid ^3He quasiparticles travel with photon like trajectories.

The use of a pulsed sweep measurements has decreased the effects of noise on the data. This allows reliable measurements to be taken at lower powers than possible with amplitude sweeps. Pulsed sweeps will be a useful tool for future measurements where comparisons between the base temperature of the cell and excited state are vital.

The images have shown that the quantum vortex tangle produced by a vibrating wire appears above the wire. This shows that quantum turbulence is not homogeneous about the wire as we would have expected. We currently do not understand why this is the case and it provides an interesting avenue for further investigation. This could be the effects of surface roughness of the wire on the nucleation of turbulence into the fluid.

We have demonstrated the ability to picture quantum vorticity and this offers up a whole world of further investigation of phenomena in ^3He superfluids. Vortices are not the only topological defects that can imaged in superfluid ^3He . For example, a future device might be designed to image the phase boundary between the A and B phases.

Of course 25 (or fewer in practice) pixels does not offer high resolution. With careful design it would be possible to scale up the number of forks in the camera and place them closer together. However the amount of wiring would have to increase proportionally, causing further heat leaks into the cell. NEMS offer a potential step up improvement in almost all areas[20, 27, 71], they can be placed closer together and, as long as multiplexing of the devices is achievable, to keep the amount of wiring limited. With finer resolution a future camera could image a single vortex, perhaps even the

double core structure. Furthermore simulations of quantum turbulence in $^4\text{He-II}$ at low temperature show the formation of a boundary layer of quantum vorticity forming at the wire's surface[100]. Study of this layer with a higher resolution camera would allow comparisons with the turbulent layer found in classical turbulence.

Chapter 7

Acoustic Damping of Quartz Tuning Forks in ^3He

Acoustic emission is a mode of damping observed on tuning forks in ^4He [12, 25, 116] and ^3He - ^4He mixtures[65, 117, 118]. Sound emission of the forks is strongly frequency dependent and typically becomes significant at about 80 kHz to 100 kHz[25], although this is size dependent; with bigger forks this figure would change[12]. Acoustic emission can also affect lower frequency devices when standing waves are present[12, 103, 119]. In this chapter we will first discuss the model of acoustic emission in helium liquids and then present new experimental results in normal and superfluid ^3He .

7.1 Overall Damping Model

A fork resonating in liquid helium will feel the effects of a number of damping sources. We have already discussed hydrodynamic damping accompanying viscosity in section 3.3.1 and ballistic damping from quasiparticles in section 3.3.2. If the fork has sufficient velocity, turbulence and pair breaking can also contribute to the damping. The total damping on the fork Δf_2 will then be the sum of contributions from all damping sources:

$$\Delta f_2 = \Delta f_2^i + \Delta f_2^H(T) + \Delta f_2^A(f) + \Delta f_2^v(v), \quad (7.1)$$

the intrinsic damping Δf_2^i of the fork, the hydrodynamic damping Δf_2^H discussed previously in section 3.3.1, acoustic damping Δf_2^A and velocity dependent damping Δf_2^v . Intrinsic damping corresponds to the low temperature vacuum damping and we assume it to be a constant. It will typically vary, however, for different forks of different masses.

At low temperatures, the normal fluid component of the two fluid model becomes negligible at about 950 mK in ^4He and 250 μK in ^3He . Instead of hydrodynamic factors, the damping becomes dominated by the scattering of thermal excitations in

the regime known as ballistic damping. It has no frequency dependence in ^3He [11] or ^4He [82]; and the transition from hydrodynamic drag can be noted by a lack of frequency dependence[70, 120]. Since here we are considering the damping as function of frequency, we will therefore neglect ballistic drag as it can be approximated by a constant value.

Turbulence, as previously discussed, has a critical velocity of creation at which a resonator will feel increased damping from the creation of vorticity in both normal fluids and superfluids. In superfluid $^3\text{He-B}$ at ultra-low temperatures it has a critical velocity of about 7 mm s^{-1} [15] while in ^4He it is typically higher.

Landau's velocity is the critical velocity needed to create excitations in a superfluid (see section 2.1.1). In ^4He it is so high ($>50 \text{ m s}^{-1}$) as to be unobtainable by our resonators, because the fork's tips would touch each other at about 2 m s^{-1} . Landau's velocity in ^3He is much lower at 27 mm s^{-1} since the fermionic condensate has a smaller energy gap. However due to flow enhancement of the velocity field about a fork it is seen at 9 mm s^{-1} . All the measurements described below avoid any critical velocity by using a tuning fork velocity below 1 mm s^{-1} .

7.1.1 Acoustic Damping

There are two approaches developed by the Prague group[12] for modelling the acoustic emission of a fork and hence the damping. The first model considers the two prongs as infinite cylinders emitting cylindrical acoustic waves. This reduces the dimension of the problem, giving the model's name as the "2D model". An alternative approach considers that the fork's prongs have the highest velocity at the tips and naturally this will be the point of maximum emittance. The rest of the prong is disregarded and only the tips are considered as emitters of sound waves. This solution is fully 3 dimensional so is called the "3D model". Both these models were compared by the Lancaster group in ^4He at 4.2 K and 1.5 K[25]. The results showed that the 3D model gave the best approximation to the damping measured on the fork and so we will discuss and use this model for ^3He acoustic damping.

The 3D model starts with the velocity potential Φ for a point source monopole emitting spherical acoustic waves:

$$\Phi = \frac{1}{4\pi} \frac{B}{r} e^{i(kr - \omega t)} \quad (7.2)$$

where k is the wave number of the acoustic wave, ω is the angular frequency of sound, r is the distance from the monopole, B is the source strength that is equal to the emitting area times the velocity amplitude v , $B = WL_e v$; where L_e is the effective emission length. The effective emission length is related to the length L of the fork

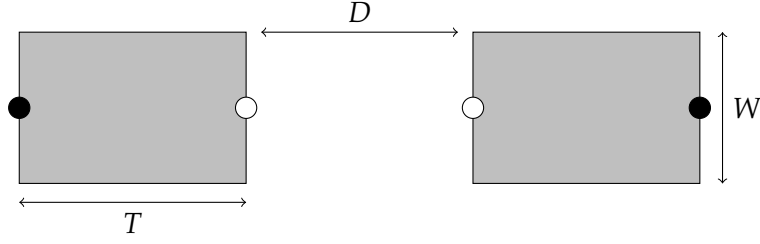


FIGURE 7.1: The positions of acoustic monopoles shown as circles in the 3D model. The tips of the fork prongs are shown along with the monopole nodes (black circles) and anti-nodes (open circles); with fork dimensions thickness T , width W and tine (or tip) separation D .

and takes into account the velocity profile of the fork along the prong and at the fundamental resonance is $L_e = 0.3915L$ [25].

To model the fork tips' sound emission the 3D model places four acoustic monopoles along a straight line as shown in fig. 7.1. The two outermost poles move sinusoidally in anti-phase with the two innermost poles. Hence the two outermost poles have equal strength B and the inner poles have strength $-B$. From here it is possible to find the velocity profile of the whole system:

$$\Phi_{3D} = \frac{iBke^{i\omega t}}{2\pi} \sum_{\substack{m=0 \\ \text{even}}}^{\infty} (2m+1) P_m(\cos(\theta)) h_m(kr) \left[j_m\left(\frac{k(D+2T)}{2}\right) - j_m\left(\frac{kD}{2}\right) \right] \quad (7.3)$$

where P_m are Legendre polynomials, h_m are spherical Hankel functions and j_m are spherical Bessel functions of the first kind. We can derive the emission power of the quadrupole as:

$$P_{3D} = \frac{\rho\omega W^2 L_e^2 v^2}{2\sqrt{2\pi(D/2)(D/2+T)}} \sum_{\substack{m=0 \\ \text{even}}}^{\infty} (2m+1) \left[j_m\left(\frac{k(D+2T)}{2}\right) - j_m\left(\frac{kD}{2}\right) \right]^2. \quad (7.4)$$

For the fork we can use the following definition[25] to find the damping on the fork in terms of the power dissipation $\dot{Q} = P_{3D} = Fv$ and eq. (3.4):

$$\Delta f_2 = \frac{\dot{Q}}{2\pi m_{\text{eff}} v^2}. \quad (7.5)$$

Using equation 7.4 and recalling $k = 2\pi\omega/c$ where c is the speed of sound we can find the fork damping due to acoustic emission as:

$$\Delta f_2 = C_{3D} \frac{\rho}{c} \frac{W^2 L_e^2 f_H^2}{m_{\text{eff}}} \left(\frac{f_H}{f_0} \right)^2 \sum_{\substack{m=0 \\ \text{even}}}^{\infty} (2m+1) \left[j_m \left(\frac{\pi f_H (2T+D)}{c} \right) - j_m \left(\frac{\pi f_H D}{c} \right) \right]^2, \quad (7.6)$$

where C_{3D} is a constant that we will treat as a fitting parameter.

In the long wavelength limit where the wavelength of emitted sound is more than the relevant fork dimension it is possible to simplify eq. (7.6) by using a Taylor expansion of the Bessel functions giving[25]:

$$\Delta f_2 = C_{3D} \frac{64\pi^4 0.3915^2 (T+D)^2}{5} \frac{\rho}{\rho_q^2} \frac{1}{c^5} \left(\frac{f_H}{f_0} \right)^2 m_{\text{eff}} f_H^6, \quad (7.7)$$

where ρ_q is the density of quartz. The fork's mass m_{eff} is proportional to the prong length L which itself varies with the resonant frequency as $f^{-0.5}$. The ratio of the resonant frequencies in helium and vacuum is close to unity. We can now see acoustic damping rises in the frequency as a power law of $f^{5.5}$.

In general the model makes a few assumptions. Firstly that there is an axial symmetry about the line of the quadrupole, this is naturally not the case for an actual fork. The material of the fork will absorb or reflect some of the waves and the quadrupole is already a simplification of a much richer system. Secondly we assume that the sound energy is completely lost. In the confines of an actual experimental cell standing waves can be set up between the fork and its surroundings. Standing waves are much more effective at dissipating power from the fork and result in a massive increase in the fork's width or even double resonances[12]. Standing waves and all other sound emission can be suppressed by placing the fork in a container with a characteristic size less than the wavelength of sound. Lastly an implied assumption is that the wavelength of sound is much less than the characteristic sizes of the fork i.e. $L, W \ll \lambda$. It actually turns out that the wavelength of sound in helium is of the order of the fork dimensions[12]. This will mean the power is underestimated by the model. However this discrepancy, as well as other imperfections, should be compensated for by the fitting parameter C_{3D} .

7.2 Acoustic Damping Measurements in ^4He

Figure 7.2 shows measurements of the damping width of the mechanical resonance as a function of frequency for forks with a width of $75 \mu\text{m}$. The measurements at 4.2 K and 1.5 K were taken at saturated vapour pressure in an immersion fridge, and

have been previously reported[25]. Further measurements taken at a temperature of 450 mK and pressure of 22 bar are also shown. These measurements were performed in a dilution refrigerator unit to achieve temperatures below 1 K[14].

Fits to the hydrodynamic damping in eq. (3.25) are also shown in fig. 7.2. In the hydrodynamic regime at 4.2 K and 1.5 K the hydrodynamic model well describes the fork damping up to 100 kHz as a slow rise in the damping as the frequency increases. We use the fitting parameters previously found for the hydrodynamic model of $\beta = 0.2603$, $B = 0.28$ and $C = 0.542$ [25]. At 450 mK there is negligible normal fluid and the damping regime is ballistic so we see no hydrodynamic damping and therefore there is no frequency dependence in the damping.

Finally fig. 7.2 shows the full damping model from eq. (7.1). Above about 80 kHz to 100 kHz there is a sharp rise in the frequency dependence due to sound emission becoming the dominant damping factor on the forks at all three temperatures. The values of the first sound velocity at saturated vapour pressure are well known and can be looked up from reference tables[121] to be 190 m s^{-1} at 4.2 K and 235 m s^{-1} at 1.5 K. The sound velocity is sensitive to the pressure of helium and the sound velocity value for the higher pressure data was estimated using reference [122] to be 355 m s^{-1} . For the acoustic parameter C_{3D} we again used the previously determined value of $C_{3D} = 2.17$ [25] at all temperatures.

At higher temperatures the models well describe the damping on the forks and there is little scatter. At lower temperatures there is a notable scatter that we attribute to variations in the intrinsic damping in the forks. Nevertheless despite changes in pressure, experiment setup and temperature between the results the fitting parameters hold and successfully describe the variations in the three discussed regimes. This is thanks to the custom manufacturing of the forks that controls the surface roughness to a finer degree and allows for this type of systematic study. The forks here have a surface roughness of about $1 \mu\text{m}$ compared to $5 \mu\text{m}$ of commercially available forks[10]. Thus we can conclude that the model is a successful description of the damping forces on quartz tuning forks in ^4He liquids.

Sound in a superfluid has a number of extra modes not normally encountered in everyday nature. He-II has 4 modes: *first sound* that is the normal pressure-density wave of everyday life and that we have observed; *second sound* that is an entropy-temperature wave¹; *third sound* that is superfluid ripples on thin films[4, 123]; and lastly *fourth sound* that is temperature-density waves in superleaks and narrow channels[4, 123]. The experiments here are performed in bulk helium and so third and fourth sound are not supported. Second sound is a bulk mode but it is believed to

¹In the two fluid model one can equally treat second sound as a wave in the superfluid and normal-fluid densities.

couple poorly to tuning forks[12] and furthermore is frozen out at low temperatures in the ballistic regime.

Lastly an implicit assumption in the data analysis is that the effective emission length L_e is unchanged from the fundamental to the first overtone mode. There is no particular reason why this should be the case. However fig. 7.2 shows that data points on the fundamental and overtone modes have a similar dependence in the acoustic regime, validating the assumption.

7.3 Measurements in ^3He

Figure 7.2 shows measurements of tuning fork damping against resonant frequency in ^3He , the forks had a width of $W = 50 \mu\text{m}$ and are part of the quasiparticle camera described in chapter 6. The camera allowed measurements on 25 tuning forks at their fundamental and overtone modes in ^3He at a range of temperatures achieved during the course of cooling and running the fridge.

The first measurements were taken in vacuum when the cryostat was cooled to 4.2 K. The forks themselves are cooled by the heat conduction of the electrical leads. It is entirely possible that the forks are at a higher temperature than the surrounding cryostat during these measurements which could explain some of the scatter in the vacuum data of fig. 7.2. In addition flexural modes of the array body could contribute to the damping. Measurements in normal fluid ^3He were taken at temperatures of 1.5 K, 115 mK and 10 mK. After the necessary precooling period the cell was demagnetised and measurement temperature of 150 μK in $^3\text{He-B}$ was used for measurements.

The top graph of fig. 7.2 shows no initial frequency dependence that we would expect from the ballistic regime. The data then appears to rise far more steeply than the expected power law dependence. Furthermore in contrast to the ^4He data the rise gives the impression of starting later.

The normal fluid data in the bottom graph of fig. 7.2 shows that there is weak frequency dependence initially in the fundamental resonances. In the 10 mK data this weak dependence continues to the overtone data at higher frequencies. The 115 mK and 1.50 K data shows a frequency dependence which like the superfluid data appears to start at a higher frequency than the ^4He data.

Fits to the hydrodynamic model are shown in fig. 7.2. In ^3He the viscosity of the Fermi liquid increases as T^2 at low temperatures[50] and at 10 mK the viscosity is comparable to oil. The mean free path has the same dependence and this means that the approximations used for the hydrodynamic model in eq. (3.25) break down. In particular the fork's small size and the high viscosity of low temperature Fermi fluid ^3He violates the $W \gg \delta$ assumption of the earlier model (see section 3.3.1). In order to

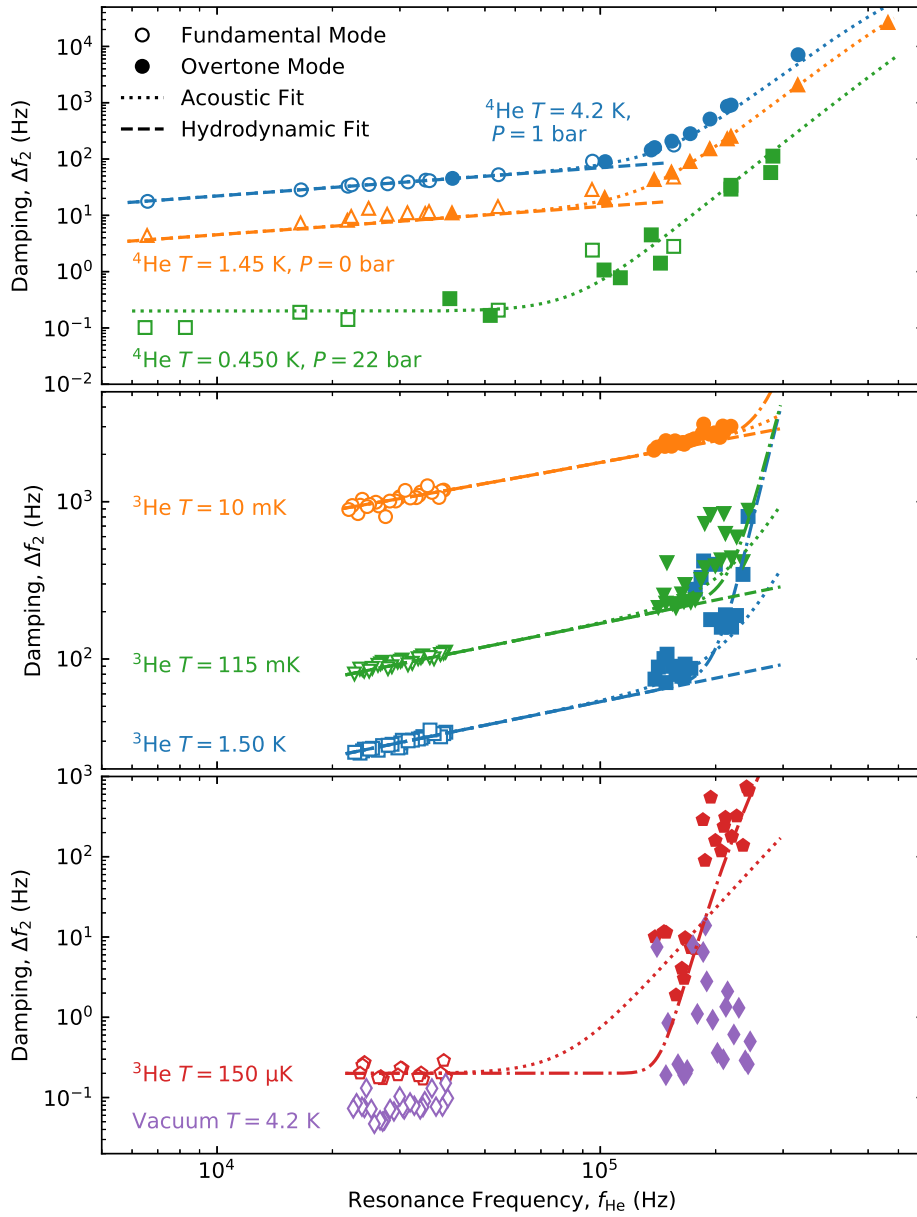


FIGURE 7.2: A log log plot of the damping width of the forks plotted against their resonant frequency at the fundamental (open symbols) and first overtone (closed symbols) resonances. (Top) acoustic damping measurements in ^4He at multiple temperatures[25], (middle) the measured data in normal fluid ^3He , (bottom) the measured data in superfluid ^3He and vacuum. The dotted lines shows a fit to the full acoustic model in eq. (7.1) while the dashed lines shows purely the hydrodynamic contribution from eq. (3.25) and the dotted dashed lines shows an exponential fit from eq. (7.8) (see text).

model the hydrodynamic damping we therefore used a full Stokes theory calculation to find the damping on the fork[124]. We multiplied the characteristic size, or fork width W , by $3/2$ in the Stokes theory calculations of the damping, which was found during the calibration of the 10 mK data against vibrating wire thermometers.

In fig. 7.2 we also fit the full damping model from equation eq. (7.1) (suitably modified to include Stokes theory for the hydrodynamic contribution). The sound velocity was found to be 169 m s^{-1} at 1.5 K increasing to 184 m s^{-1} at 115 mK and 10 mK[125]. In the superfluid the sound mode has crossed over to zero sound and the velocity increases slightly to 190 m s^{-1} [4]. The fitting constants used are discussed in detail in below sub-sections.

Figure 7.3 shows frequency sweeps at the fundamental resonance of one of the forks at all the measured temperatures. The overtone resonances is about 6.3 times higher than the fundamental resonance and are not shown in fig. 7.3. These sweeps were used to find each fork's damping and resonant frequency at both the fundamental and first overtone modes of the fork. We can see how the resonance changes as the temperature of the fork's decreases. In the vacuum the fork's resonance is narrowest which then naturally increases with the addition of ^3He . As the helium cools down the resonant damping increases as ^3He 's viscosity increases. In the superfluid there is practically no normal fluid component and the width is narrow again.

Fundamental mode measurements were measured using a SR830 lock-in amplifier and signal generator combination as for the quasi-particle camera. Overtone measurements which are not shown used a SR844 high frequency lock-in amplifier and signal generator combination which could operate in the range of frequencies the fork overtones lie in. Where possible the fits for multiple sweeps on the forks were used to find a mean for the resonant frequency and width of the forks. By taking the average for the sweep the standard error in the mean could be used to provide an uncertainty value. The uncertainties were found to be relatively small as compared to the width and are not shown in the figures.

For the normal fluid thermometry we used the forks themselves as thermometers, which is possible up to about 1.6 K[50]. In order to do so we calibrated the forks against vibrating wire thermometers at 10 mK. This then allowed us to find the temperature of the forks at the other measurement temperatures in ^3He by comparing the measured damping against the expected damping as a function of viscosity. The validity of this method is supported by the 1.5 K measurements, with which the temperature agrees closely with the estimated temperature of the 1 K pot (from saturated vapour pressure recordings) the only cooling mechanism in operation at the time.

Helium-3 (normal and superfluid) introduces a further mode, in addition to those already mentioned, that is known as zeroth (collision-less) sound discussed

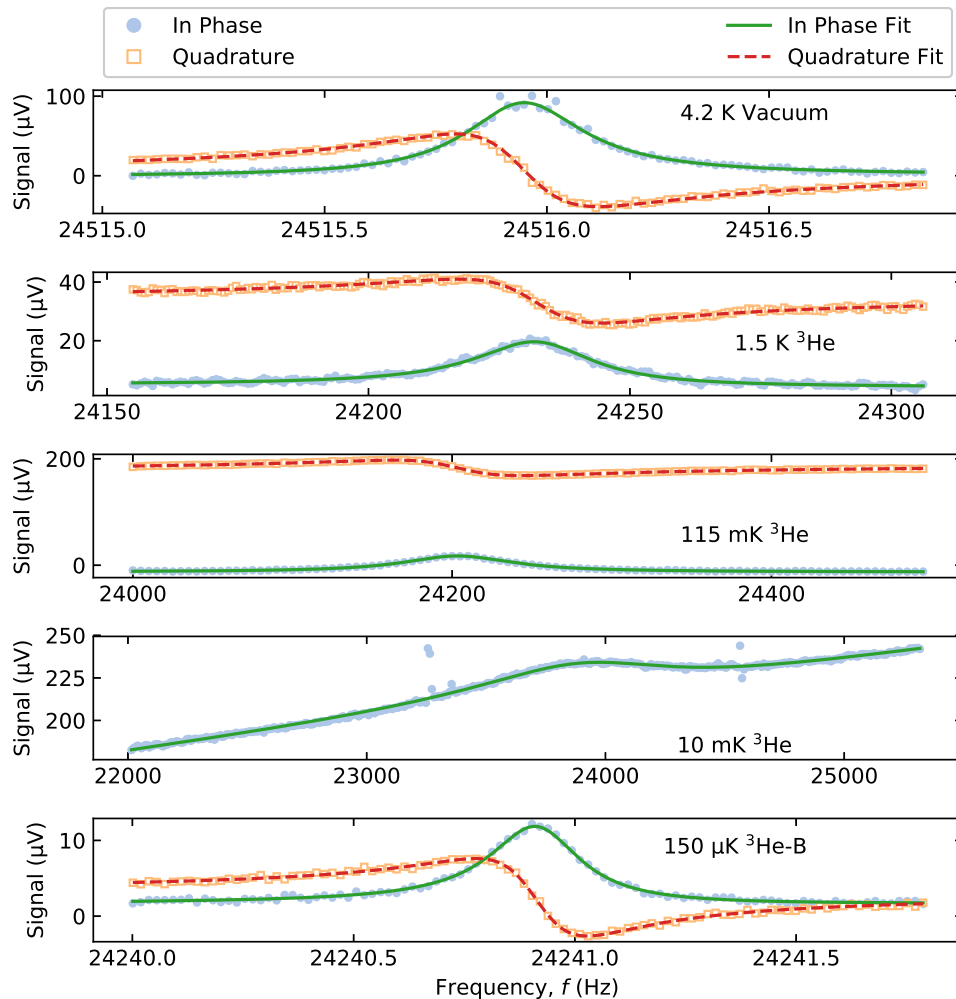


FIGURE 7.3: The measured in phase (blue circles) and out of phase (orange open squares) responses as a function of frequency for one of the tuning forks at indicated temperatures at the fundamental resonance. Also shown are Lorentzian fits to the responses for in phase and out phase components (green line and red dashed line respectively). For clarity only the in phase response is shown at 10 mK because the background signal between the two is large.

in section 2.2.2. It has a similar dispersion curve to first sound[4] so the crossover should not significantly effect the sound emission of the forks, despite a small velocity difference[4].

7.3.1 Initial Fitting Attempts

In fig. 7.2 we initially fitted to the bottom edge of the data, in the belief that the data points higher than this were affected by acoustic standing waves causing higher damping. The superfluid data's gradient was much steeper than the damping model in eq. (7.1) and it was then very hard to fit the data with the acoustic model without changing the values the values of C_{3D} . Specifically in fig. 7.2 we used $C_{3D} = 0.3$ at temperatures of 1.5 K and 150 μK ; and $C_{3D} = 1.0$ at 115 mK and 10 mK. For the ^4He across different forks, temperatures and pressures the acoustic constant C_{3D} was constant, so it seemed unlikely that it changed in ^3He . Also we see that the transition to higher damping apparently occurred at a higher frequency than in ^4He .

The acoustic model's fits as discussed were unsatisfactory, which lead to the fitting of other types of dependence to the data. In particular we concentrated on the superfluid data which showed the most clear dependence. A polynomial order of around 14 successfully described the data, however such a high order is clearly un-physical because it fits no known model or excitation. Another fit shown in fig. 7.2 as dotted lines was found by using an exponential to model the data:

$$\Delta f_2(f) = a \exp\left(\frac{-b}{f}\right) + \Delta f_2^H(f) + \Delta f_2^i \quad (7.8)$$

where a and b are fitting constants. The fit closely follows the data points and it was found that for all temperatures $a = 50$ MHz and $b = 2.8$ MHz.

This leaves open the question of the physical nature of the exponential. Such dependencies imply an energy gap or barrier in the creation of the excitation carrying the energy packet. Because we do not see such a dependence in ^4He the excitation needed to be unique to ^3He and exist in both the normal and superfluid states where the dependence is seen. This excludes the aforementioned zero sound that has no energy gap and is known to have a similar dispersion curve to first sound. Unique gaped superfluid ^3He modes such as clapping and squashing are also rejected[4].

The first candidate is spin waves carried by magnons discussed in section 2.2.2. It has recently been found that forks resonating at the Larmor frequency can feel an extra damping force[126] in certain conditions in $^3\text{He-B}$. Possibly the constants a and b could relate to the Larmor frequency. However, the different temperature data sets were taken at vastly different fields from 0.03 T to 6.2 T. So a relation between a and

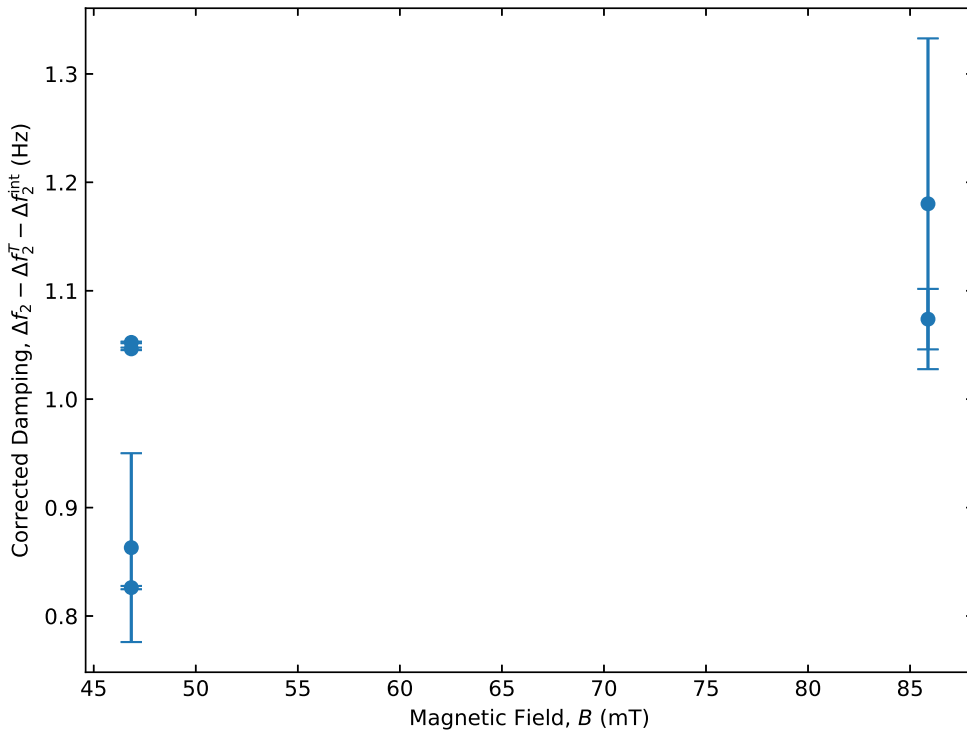


FIGURE 7.4: The temperature corrected damping as a function of the magnetic field strength for the overtone resonance of one of the forks in superfluid $^3\text{He-B}$.

b , which both stay constant at all measured fields and temperatures, with the Larmor frequency is non-existent.

It is known however that surfaces in that are immersed in liquid ^3He typically have a solid layer of ^3He clamped to the surface that is three atoms thick and the magnetisation increases strongly at low temperatures[127]. Moving the magnetisation vector will apply a damping force to the fork as has been observed[126]. In our geometry however, assuming the magnetisation vector lines up with the external field, there would be no change in the magnetisation direction. We have only taken measurements at a few fields and have not done a systematic study.

Figure 7.4 summarises the available data on one of the forks and shows the temperature independent damping as a function of the magnetic field in $^3\text{He-B}$. No clear magnetic field dependence is seen in fig. 7.4 despite a doubling in the field strength over the values measured at temperatures where the solid magnetisation of ^3He is strong[127]. Higher fields in $^3\text{He-B}$ are hard to achieve since the magnetic field is used for cooling and as the field increases the B phase becomes distorted.

An absence of a magnetic field dependence could be explained by the presence of a surface magnetic field created by the chrome electrical contacts on the forks.

Speculating we could say this chrome would interact with the bulk field and affect the magnetisation in the solid layer of ^3He attached to the fork. However the Larmor frequency at the lowest measured fields is 1.46 MHz, far above any measured resonances of the tuning forks. All in all, we do not see any magnetic dependent damping on the tuning forks here.

Lastly we note that the effect seen in ref [126] was only seen with one fork out of two, and on a fork with a rougher surface suggesting the surface roughness has a strong effect. The forks used in this work are likely to be considerably smoother thanks to the custom manufacturing process. This suggests that the effect might not be seen on our forks, but this remains an open question.

7.3.2 The Effects of Fork Confinement

Having exhausted known ^3He excitations, next we looked at the effects of the camera itself on the forks. It is well known that cavities suppress acoustic emission and despite the open pipe nature of the camera there could still be an effect on the forks[116]. Here we use a practice camera in ^4He to find the confinement effects of the camera on the forks and compare with the ^3He results. The ^4He camera has an identical geometry to the camera in ^3He but only one fork array.

Figure 7.5 shows the measured damping against the resonant frequency of the forks in the practice camera at temperatures of 4.2 K, 1.5 K and 1.2 K at saturated vapour pressure in ^4He . Fits to hydrodynamic and full damping models in eqs. (3.25) and (7.1) as dashed and dotted lines respectively are also shown. All fits use the same fitting parameters found previously for ^4He in section 7.2.

The low temperature data from fig. 7.5 shows that fork sound emission is suppressed by the practice camera in ^4He , while the 4.2 K data shows only suppression of the first three forks overtone resonances. The two highest frequency forks do emit sound and have corresponding damping increase to show for it. Clearly we can conclude the camera does have an effect on sound emission by blocking sound waves that have a wavelength above the cavity size of the camera. Variations in the sound velocity in helium mean the effect is not clear due to the resultant frequency variations. Therefore we plot the wavelength of emitted sound to compare the ^4He and ^3He camera measurements from figs. 7.2 and 7.5 in fig. 7.6 by plotting the measured damping as a function of wavelength.

Figure 7.6 shows that wavelengths higher than about 1 mm are suppressed in both ^3He and ^4He . A fork placed in a cavity like we have here would only be able to excite waves with wavelengths up to the size of the cavity. Neatly fig. 7.6 shows that the cutoff wavelength for acoustic suppression and the camera cavity size of 1 mm agree with each other. Full suppression to the hydrodynamic damping fit line

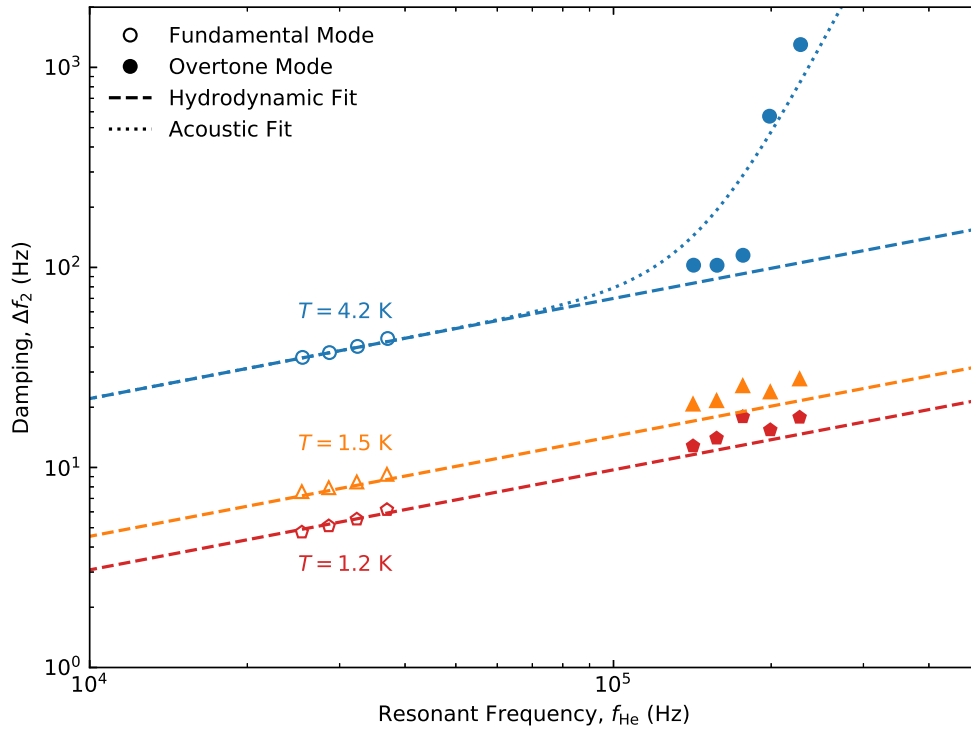


FIGURE 7.5: A log log plot showing measurements of the fork damping against the fork frequency at the fundamental (open symbols) and overtone resonances (closed symbols) of the fork at temperatures of 4.2 K, 1.5 K and 1.2 K. Fits to the hydrodynamic model (dashed lines) in eq. (3.25) and full damping model (dotted lines) in eq. (7.1) are also shown. All the fits use the same fitting constants: the hydrodynamic constants $\beta = 0.2603$, $B = 0.28$, $C = 0.542$; and acoustic constant $C_{3D} = 2.17$. Here the forks are placed in a practice quasiparticle camera with a cavity diameter of 1 mm.

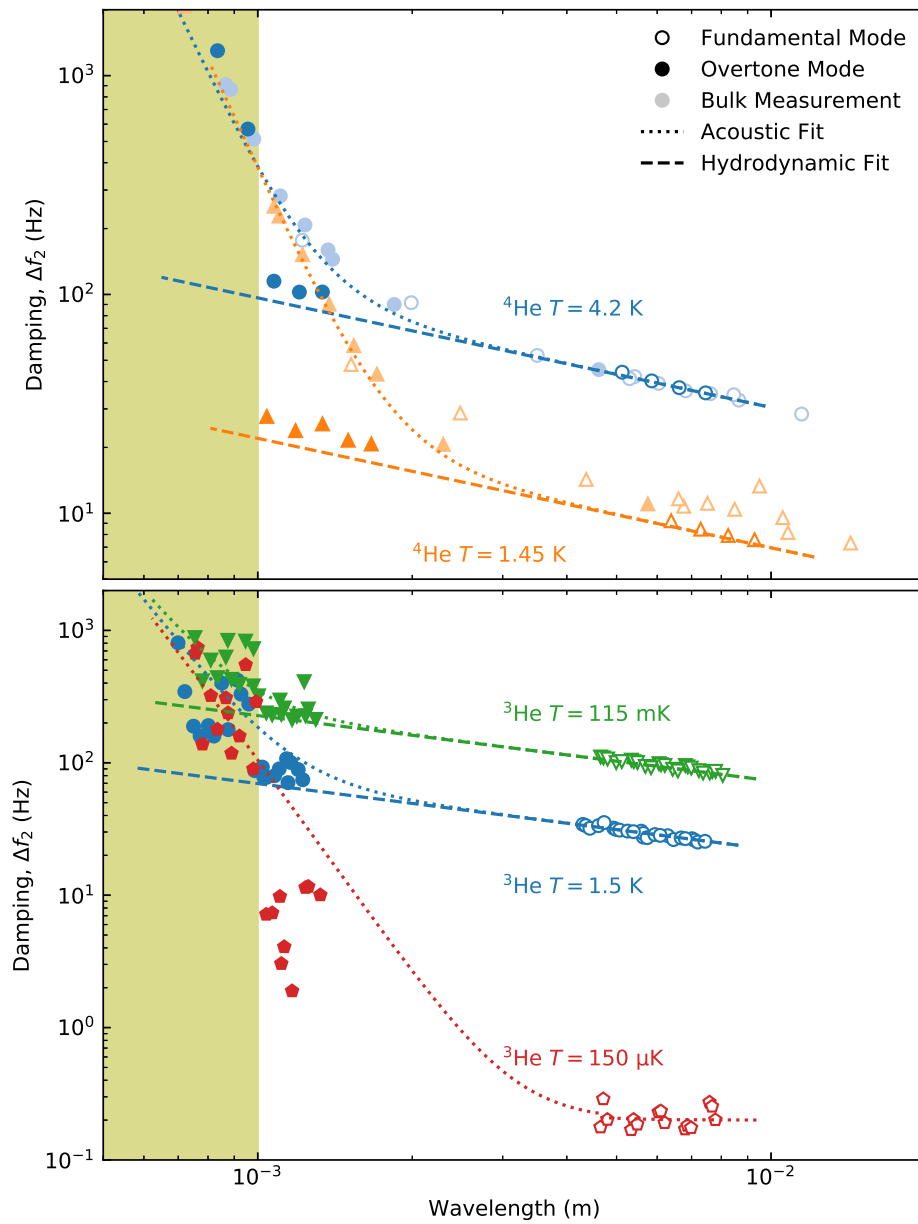


FIGURE 7.6: A log log graph of the measured damping of forks at fundamental (open symbols) and overtone (closed symbols) resonances in ^4He (top) and ^3He (bottom) against the wavelength of emitted sound. Grayed out points show bulk measurements in ^4He for comparison. Dotted and dashed lines show the full damping model and the pure hydrodynamic component from eqs. (3.25) and (7.1) respectively. The filled in area shows where sound emission is unsuppressed by the camera cavity size of 1 mm

does not appear to occur however, which is presumably due to the open nature of the cavity, allowing some sound waves of higher wavelengths out. We note that the almost complete suppression however probably shows that the main direction of tuning fork sound emission is in the camera face plane not towards the openings of the pipe.

7.3.3 Present Understanding

We can now fit the acoustic damping for the forks in ^3He , with the knowledge that some forks have their acoustic damping suppressed[128]. As in ^4He we used the same acoustic fitting parameters for all temperatures measured in ^3He . Furthermore we assume that the acoustic emission strength is the same in both isotopes.

Figure 7.7 shows damping against frequency for the same measured points and hydrodynamic fits as fig. 7.2 but with a different acoustic strengths in the full damping model (the same fit is also shown in fig. 7.6). The acoustic fit uses fitting parameter $C_{3D} = 2.17$, the same as used in ^4He .

The data in fig. 7.7 is not quite as clear as it was in ^4He camera measurements due to large scatter in both the superfluid and 1.5 K normal fluid data. This could be due to an off center camera cavity alignment for the forks which can be seen in fig. 6.2; two arrays in particular are noticeably off-center and it is conceivable that this would have an effect on the fork's emission profile[116], and hence the damping. Furthermore there is noticeable noise still in the overtone data that could be due to temperature fluctuations during measurements or perhaps standing acoustics waves. The intrinsic damping is much too small to be able to explain the observed scatter of results. Despite this though the data points still seem to follow the trend suggested by the full damping model in eq. (7.1) suggesting that we are seeing acoustic emission in ^3He .

7.4 Conclusions

We investigated the frequency dependent damping of tuning forks in ^3He and ^4He and found that the damping increases significantly above about 100 kHz. This rise can be explained by the 3D model of acoustic damping along with hydrodynamic damping or ballistic damping depending on the temperature of helium. We found that despite changes in pressure, cell and helium isotope the 3D model of acoustic damping successfully describes the acoustic damping felt by quartz tuning forks.

Any further experimental study of sound emission work should use forks in bulk fluid to avoid cavity effects seen here in a custom made cell. Furthermore a wider

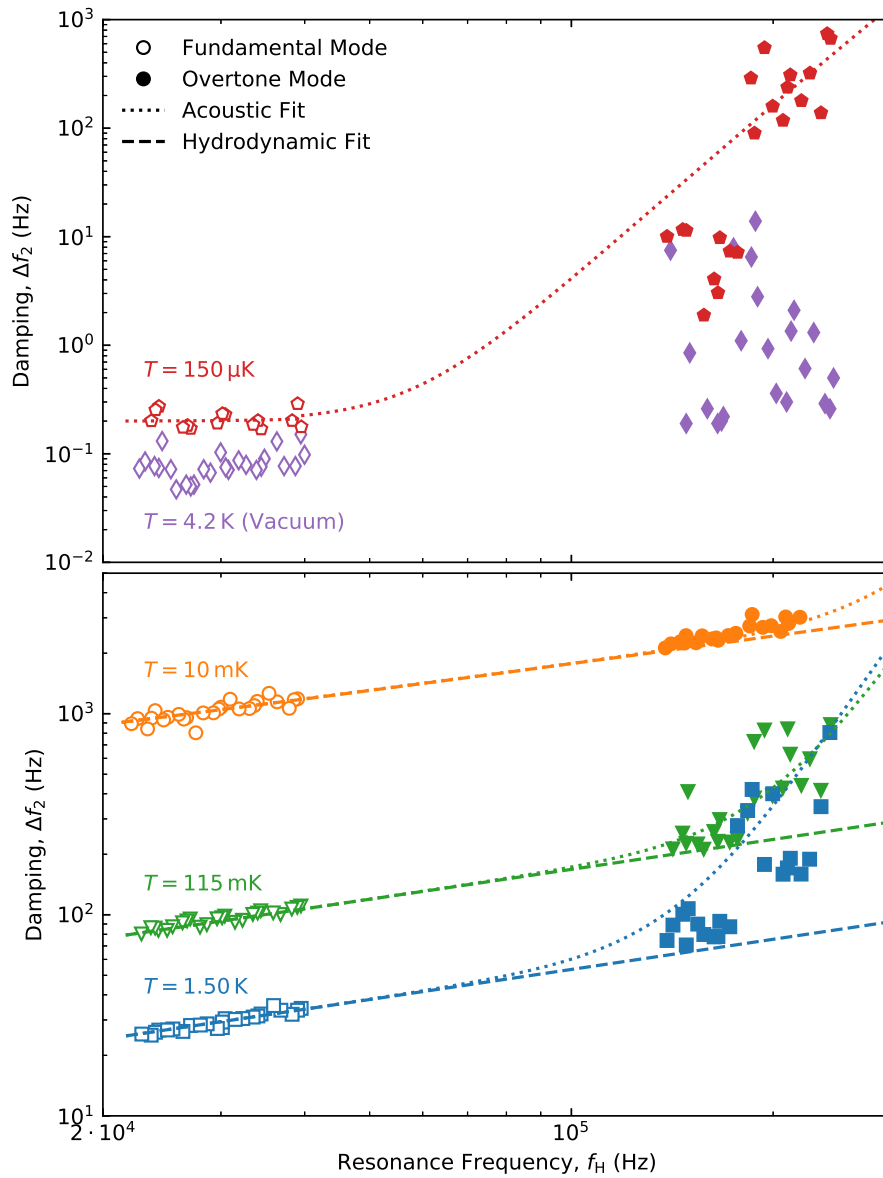


FIGURE 7.7: A log log plot of the fork damping vs resonant frequency at the fundamental and overtone resonances at a range of temperatures in ^3He . The dotted lines are fits to the full damping in eq. (7.1) while the dashed lines show the hydrodynamic damping contribution from eq. (3.25).

spread of frequencies should be used so that the gap in between the overtone and fundamental modes can be closed and higher frequencies investigated.

The nature of magnetic damping in ^3He is still an open question, with fork roughness apparently an important factor. A systematic study with the forks here would seem ideal to help answer these questions. To investigate any magnetic field effects it would be prudent to increase the fork's sensitivity to such effects by suppressing acoustic emission with a cavity.

In recent years researchers have developed NEMS devices of sizes approaching the coherence length of the superfluid particles themselves. Recent experiments with such devices have been performed in ^4He [26, 27, 71, 72] and the next logical step is to immerse these devices in ^3He to open up a new regime of study. High frequency devices placed in ^3He could experience acoustic damping as for the forks described above. However the use of cavities, be they cameras or tubes, can suppress acoustic damping as illustrated in the experiments above.

Chapter 8

Summary

This thesis presented work on: using multi-frequency methods to measure the non-linear forces of quantum turbulence in $^4\text{He-II}$; using a quasiparticle camera in $^3\text{He-B}$ to image a quasiparticle beam and quantum turbulence; and measuring acoustic damping in normal and superfluid ^3He and ^4He .

We found that multi-frequency methods can be successfully used to measure the resonance of a tuning fork in the linear regime. We directly compared multi-frequency and single frequency measurements finding that both agreed well with each other during the cooldown of the fork in ^4He . The results suggest the MLA can be used for fast and efficient measurements of other linear devices. In more elaborate setups it could be used to multiplex measurements across multiple devices.

In further multi-frequency measurements we exploited existing non-linearities in the system: while the fork was generating quantum turbulence we used a two frequency excitation to create intermodulation products in the response of the fork. The measurement of these intermodulation products allowed us to probe information about the non-linear forces of quantum turbulence. These measurements found that the in-phase component of non-linear force negatively increases after a critical velocity showing an increased retarding force on the fork. At a slightly higher critical velocity the quadrature component of the non-linear force increases, which we interpret as energy loss due to vortex ring emission by the fork.

To more fully make comparisons between quantum turbulence and classical turbulence we need to be able to see its spread about devices as well as its effects on devices. So in superfluid $^3\text{He-B}$, we used a quasiparticle camera comprised of a five by five array of quartz tuning forks to measure a beam of ballistic thermal excitations. The quasiparticle beam was created by breaking Cooper pairs inside a box (BBR), which escape the box via an orifice pointed toward the camera. The increased resonance width of the forks when the BBR was heated allowed us to find the fraction power deposited at each camera pixel. We compared the measured quasiparticle flux to a theoretical model where quasiparticles originate on a diffuse light emitting disk (the BBR orifice) and a simulation of quasiparticle behaviour. A

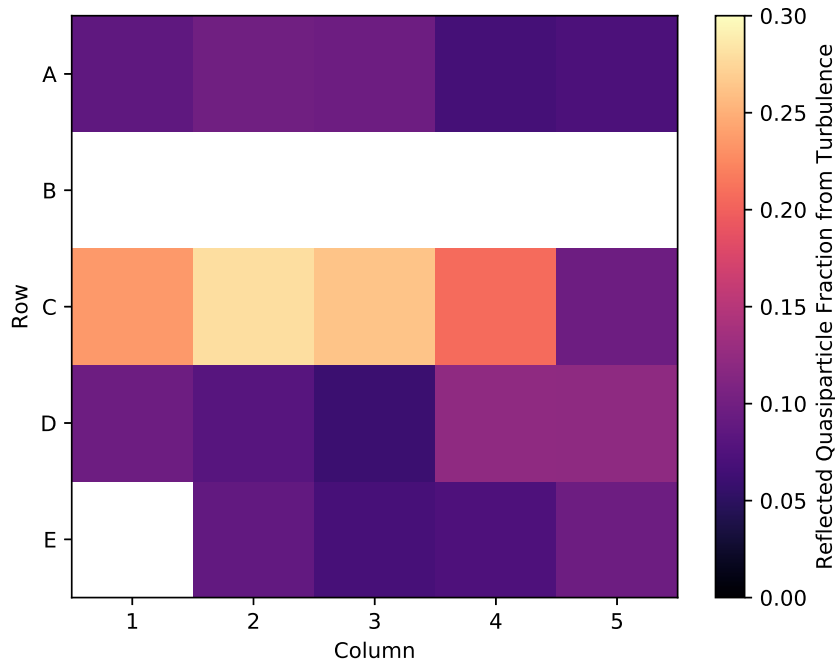


FIGURE 8.1: A heat map image of quantum turbulence while the source wire was moving at a speed of 15.6 mm s^{-1} .

comparison of the measurements and simulations showed that the quasiparticles as expected travel in the medium with light like trajectories. Our simulation accounted for the actual thickness of the BBR orifice and showed that quasiparticles in $^3\text{He-B}$ experience both diffuse and specular scattering in reflections off the orifice walls.

We created turbulence in between the BBR and the camera. A fraction of quasiparticles from the beam were blocked from reaching the camera by Andreev reflection from the flow field surrounding quantum vortices. By comparing the quasiparticle flux images of the heated and unheated BBR we found the fractional screening of quasiparticles by quantum turbulence, as shown in fig. 8.1. The measurements showed that quantum turbulence develops above the wire initially. The cause of this non-homogeneity is currently unknown, but is perhaps due to an excess of pinning sites on top of the wire.

The demonstration of operating a quasiparticle camera opens up further avenues of research in superfluid $^3\text{He-B}$. Images could be produced of other topological phenomena in other experiments, such as the collapse of A-B phase interfaces. Future cameras could increase the number of pixels and decrease the pixel size to allow for higher resolution images of turbulence. NEMS in particular have the potential to improve the camera in both regards.

To be able to plan experiments with NEMS effectively we need to understand the

dissipation mechanisms of helium. To this end we measured the effect of acoustic emission on quartz tuning forks in both ^4He and ^3He . In ^4He we observed that the accepted hydrodynamic and acoustic models describe the tuning fork data at different pressures, temperatures and in different experimental cells well. In ^3He we used the forks in the quasiparticle camera to explore the acoustic damping present. The measurements show clear evidence of acoustic emission at the temperatures of 1.5 K, 115 mK, 10 mK and 150 μK . Interestingly the camera cavities suppressed acoustic emission for sound wavelengths bigger than the camera cavity size of 1 mm, making the interpretation of the data challenging. We confirmed the suppression of sound emission with an identical camera in ^4He , illustrating that acoustic emission is responsible for the large observed fork damping at higher frequencies.

The work shows that acoustic emission in ^3He can be described by the models developed and tested in ^4He . Interestingly, using the same geometric constant for acoustic emission strength can be used in both isotopes despite the more complex nature of fermionic ^3He . It is even more remarkable due to the cross over from normal to zero sound in ^3He . This shows that the custom made forks are ideal for systematic measurements in helium liquids. Also we see little evidence of any of any unique Fermi-liquid excitations affecting the forks in the regions measured. Finally our work shows that existing models can be used to predict the acoustic behaviour of devices in ^3He after measurements in ^4He providing the operating frequency does not exceed the superfluid gap.

Future work with resonating devices, such as NEMS, in ^3He and ^4He should be designed to account for the affects of acoustic emission on the quality factor using acoustic models. Designing cavities surrounding the resonator may offer partial suppression of acoustic damping. Better still devices could be designed to operate at frequencies below the threshold for a significant increase in the damping, and so avoid the problem entirely. This way the sensitivity of the resonating device can be upheld for future experiments such as NEMS based quasiparticle cameras.

Bibliography

- ¹P. Kapitza, “Viscosity of liquid helium below the λ -point”, *Nature* **141**, 74 (1938).
- ²J. F. Allen and A. D. Misener, “Flow of Liquid Helium II”, *Nature* **141**, 75 (1938).
- ³D. V. Osborne, “The Rotation of Liquid Helium II”, *Proceedings of the Physical Society. Section A* **63**, 909 (1950).
- ⁴C. Enns and S. Hunklinger, *Low-Temperature Physics* (Springer, 2005).
- ⁵W. F. Vinen, “Classical character of turbulence in a quantum liquid”, *Physical Review B* **61**, 1410–1420 (2000).
- ⁶W. F. Vinen and L. Skrbek, “Quantum turbulence generated by oscillating structures”, *Proceedings of the National Academy of Sciences of the United States of America* **111**, 4699–4706 (2014).
- ⁷G. P. Bewley, D. P. Lathrop, and K. R. Sreenivasan, “Visualization of quantized vortices”, *Nature* **441**, 588 (2006).
- ⁸W. Guo, M. La Mantia, D. P. Lathrop, and S. W. Van Sciver, “Visualization of two-fluid flows of superfluid helium-4”, *Proceedings of the National Academy of Sciences* **111**, 4653–4658 (2014).
- ⁹A. Marakov, J. Gao, W. Guo, S. W. Van Sciver, G. G. Ihas, D. N. McKinsey, and W. F. Vinen, “Visualization of the normal-fluid turbulence in counterflowing superfluid ^4He ”, *Physical Review B* **91**, 094503 (2015).
- ¹⁰D. Schmoranzner, M. J. Jackson, Š. Midlik, M. Skyba, J. Bahyl, T. Skokánková, V. Tsepelin, and L. Skrbek, “Dynamical similarity and instabilities in high-Stokes-number oscillatory flows of superfluid helium”, *Physical Review B* **99**, 054511 (2019).
- ¹¹D. I. Bradley, P. Crookston, S. N. Fisher, A. Ganshin, A. M. Guénault, R. P. Haley, M. J. Jackson, G. R. Pickett, R. Schanen, and V. Tsepelin, “The Damping of a Quartz Tuning Fork in Superfluid $^3\text{He-B}$ at Low Temperatures”, *Journal of Low Temperature Physics* **157**, 476–501 (2009).

- ¹²D. Schmoranzer, M. La Mantia, G. Sheshin, I. Gritsenko, A. Zadorozhko, M. Rotter, and L. Skrbek, "Acoustic Emission by Quartz Tuning Forks and Other Oscillating Structures in Cryogenic ^4He Liquids", *Journal of Low Temperature Physics* **163**, 317–344 (2011).
- ¹³J. J. Hosio, V. B. Eltsov, M. Krusius, and J. T. Mäkinen, "Quasiparticle-scattering measurements of laminar and turbulent vortex flow in the spin-down of superfluid $^3\text{He-B}$ ", *Physical Review B* **85**, 224526 (2012).
- ¹⁴D. I. Bradley, M. J. Fear, S. N. Fisher, A. M. Guénault, R. P. Haley, C. R. Lawson, G. R. Pickett, R. Schanen, V. Tsepelin, and L. A. Wheatland, "Stability of flow and the transition to turbulence around a quartz tuning fork in superfluid ^4He at very low temperatures", *Physical Review B* **89**, 214503 (2014).
- ¹⁵S. N. Fisher, A. J. Hale, A. M. Guénault, and G. R. Pickett, "Generation and Detection of Quantum Turbulence in Superfluid $^3\text{He-B}$ ", *Physical Review Letters* **86**, 244–247 (2001).
- ¹⁶D. I. Bradley, D. O. Clubb, S. N. Fisher, A. M. Guénault, R. P. Haley, C. J. Matthews, G. R. Pickett, V. Tsepelin, and K. Zaki, "Emission of Discrete Vortex Rings by a Vibrating Grid In Superfluid $^3\text{He-B}$: A Precursor to Quantum Turbulence", *Physical Review Letters* **95**, 035302 (2005).
- ¹⁷D. I. Bradley, D. O. Clubb, S. N. Fisher, A. M. Guénault, R. P. Haley, C. J. Matthews, G. R. Pickett, V. Tsepelin, and K. Zaki, "Decay of Pure Quantum Turbulence in Superfluid $^3\text{He-B}$ ", *Physical Review Letters* **96**, 035301 (2006).
- ¹⁸R. Garcia and E. T. Herruzo, "The emergence of multifrequency force microscopy", *Nature Nanotechnology* **7**, 217–226 (2012).
- ¹⁹D. Platz, E. A. Tholén, D. Pesen, and D. B. Haviland, "Intermodulation atomic force microscopy", *Applied Physics Letters* **92**, 153106 (2008).
- ²⁰D. I. Bradley, R. P. Haley, S. Kafanov, M. T. Noble, G. R. Pickett, V. Tsepelin, J. Vonka, and T. Wilcox, "Probing Liquid ^4He with Quartz Tuning Forks Using a Novel Multifrequency Lock-in Technique", *Journal of Low Temperature Physics* **184**, 1080 (2016).
- ²¹D. B. Haviland, "Quantitative force microscopy from a dynamic point of view", *Current Opinion in Colloid & Interface Science* **27**, 74–81 (2017).
- ²²S. N. Fisher, A. M. Guénault, C. J. Kennedy, and G. R. Pickett, "Blackbody Source and Detector of Ballistic Quasiparticles in $^3\text{He-B}$: Emission Angle from a Wire Moving at Supercritical Velocity", *Physical Review Letters* **69**, 1073–1076 (1992).

- ²³M. P. Enrico, S. N. Fisher, A. M. Guénault, G. R. Pickett, and K. Torizuka, “Direct Observation of the Andreev Reflection of a Beam of Excitations in Superfluid $^3\text{He-B}$ ”, *Physical Review Letters* **70**, 1846–1849 (1993).
- ²⁴S. L. Ahlstrom, D. I. Bradley, S. N. Fisher, A. M. Guénault, E. A. Guise, R. P. Haley, S. Holt, O. Kolosov, P. V. E. McClintock, G. R. Pickett, M. Poole, R. Schanen, V. Tsepelin, and A. J. Woods, “A Quasiparticle Detector for Imaging Quantum Turbulence in Superfluid $^3\text{He-B}$ ”, *Journal of Low Temperature Physics* **175**, 725–738 (2014).
- ²⁵D. I. Bradley, M. Človečko, S. N. Fisher, D. Garg, E. Guise, R. P. Haley, O. Kolosov, G. R. Pickett, V. Tsepelin, D. Schmoranzner, and L. Skrbek, “Crossover from hydrodynamic to acoustic drag on quartz tuning forks in normal and superfluid He^4 ”, *Physical Review B* **85**, 014501 (2012).
- ²⁶D. I. Bradley, R. George, A. M. Guénault, R. P. Haley, S. Kafanov, M. T. Noble, Yu. A. Pashkin, G. R. Pickett, M. Poole, J. R. Prance, M. Sarsby, R. Schanen, V. Tsepelin, T. Wilcox, and D. E. Zmeev, “Operating Nanobeams in a Quantum Fluid”, *Scientific Reports* **7**, 4876 (2017).
- ²⁷A. M. Guénault, A. Guthrie, R. P. Haley, S. Kafanov, Yu. A. Pashkin, G. R. Pickett, M. Poole, R. Schanen, V. Tsepelin, D. E. Zmeev, E. Collin, O. Maillet, and R. Gazizulin, “Probing superfluid ^4He with high-frequency nanomechanical resonators down to millikelvin temperatures”, *Physical Review B* **100**, 020506(R) (2019).
- ²⁸J. N. Lockyer, “Notice of an observation of the spectrum of a solar prominence”, *Proceedings of the Royal Society of London* **17**, 91–92 (1868).
- ²⁹W. Ramsay, “On a Gas Showing the Spectrum of Helium, the Reputed Cause of D_3 , One of the Lines in the Coronal Spectrum, Preliminary Note”, *Proceedings of the Royal Society of London* **58**, 65–67 (1895).
- ³⁰H. K. Onnes, “Investigations into the properties of substances at low temperatures, which have led, amongst other things, to the preparation of liquid helium”, Nobel lecture 4 (1913).
- ³¹W. H. Keesom and K. Clusius, “Specific Heat of Helium”, *Proceedings of the Koninklijke Akademie van Wetenschappen te Amsterdam: Section of Sciences* **35**, 307 (1932).
- ³²F. London, “The λ -Phenomenon of Liquid Helium and the Bose-Einstein Degeneracy”, *Nature* **141**, 643–644 (1938).
- ³³L. Tisza, “Transport Phenomena in Helium II”, *Nature* **141**, 913 (1938).
- ³⁴L. Landau, “Theory of the Superfluidity of Helium II”, *Physical Review* **60**, 356–358 (1941).

- ³⁵T. Ellis and P. V. E. McClintock, "The breakdown of superfluidity in liquid ^4He V. Measurement of the Landau critical velocity for roton creation", *Philosophical Transactions of the Royal Society A* **315**, 259–300 (1985).
- ³⁶R. P. Feynman, "Atomic theory of the Two Fluid Model of Liquid Helium", *Physical Review* **94**, 262–277 (1954).
- ³⁷L. Onsager, "Statistical Hydrodynamics", *Il Nuovo Cimento* **6**, 279–287 (1949).
- ³⁸R. P. Feynman, "Application of Quantum Mechanics to Liquid Helium", *Progress in Low Temperature Physics* **1**, 17–53 (1955).
- ³⁹W. F. Vinen, "Detection of Single Quanta of Circulation in Rotating Helium II", *Nature* **181**, 1524–1525 (1958).
- ⁴⁰A. N. Kolmogorov, "The local structure of turbulence in incompressible viscous fluid for very large Reynolds numbers", *Proceedings of the Royal Society of London A* **434**, 9–13 (1991).
- ⁴¹A. N. Kolmogorov, "Dissipation of energy in the locally isotropic turbulence", *Proceedings of the Royal Society of London A* **434**, 15–17 (1991).
- ⁴²O. Reynolds, "An experimental investigation of the circumstances which determine whether the motion of water shall be direct or sinuous, and of the law of resistance in parallel channels", *Philosophical Transactions of the Royal Society of London* **174**, 935–982 (1883).
- ⁴³C. F. Barenghi, L. Skrbek, and K. R. Sreenivasan, "Introduction to quantum turbulence", *Proceedings of the National Academy of Sciences* **111**, 4647–4652 (2014).
- ⁴⁴W. F. Vinen and J. J. Niemela, "Quantum Turbulence", *Journal of Low Temperature Physics* **128**, 167–231 (2002).
- ⁴⁵W. F. Vinen, "Mutual friction in a heat current in liquid helium II III. Theory of mutual friction", *Proceeding of the Royal Society A: Mathematical, Physical and Engineering Sciences* **242**, 493–515 (1957).
- ⁴⁶W. Thomson, "XXIV. Vibrations of a columnar vortex", *The London, Edinburgh, and Dublin Philosophical Magazine and Journal of Science* **10**, 155–168 (1880).
- ⁴⁷E. Fonda, D. P. Meichle, N. T. Ouellette, S. Hormoz, and D. P. Lathrop, "Direct observation of Kelvin waves excited by quantized vortex reconnection", *Proceeding of the National Academy of Sciences* **111**, 4707–4710 (2014).
- ⁴⁸M. S. Paoletti and D. P. Lathrop, "Quantum Turbulence", *Annual Review of Condensed Matter Physics* **2**, 213–234 (2011).
- ⁴⁹W. F. Vinen, "An Introduction to Quantum Turbulence", *Journal of Low Temperature Physics* **145**, 7–24 (2006).

- ⁵⁰D. I. Bradley, M. Človečko, S. N. Fisher, D. Garg, A. M. Guénault, E. Guise, R. P. Haley, G. R. Pickett, M. Poole, and V. Tsepelin, “Thermometry in Normal Liquid ^3He Using a Quartz Tuning Fork Viscometer”, *Journal of Low Temperature Physics* **171**, 750–756 (2013).
- ⁵¹L. D. Landau, “The Theory of a Fermi Liquid”, *Soviet Physics Journal of Experimental and Theoretical Physics* **3**, 920–925 (1957).
- ⁵²P. W. Anderson and P. Morel, “Generalized Bardeen-Cooper-Schrieffer States and the Proposed Low-Temperature Phase of Liquid He^3 ”, *Physical Review* **123**, 1911 (1961).
- ⁵³R. Balian and N. R. Werthamer, “Superconductivity with Pairs in a Relative p Wave”, *Physical Review* **131**, 1553 (1963).
- ⁵⁴J. Bardeen, L. N. Cooper, and J. R. Schrieffer, “Microscopic Theory of Superconductivity”, *Physical Review* **106**, 162–164 (1957).
- ⁵⁵D. D. Osheroff, R. C. Richardson, and D. M. Lee, “Evidence for a New Phase of solid He^3 ”, *Physical Review Letters* **28**, 885 (1972).
- ⁵⁶D. D. Osheroff, W. J. Gully, R. C. Richardson, and D. M. Lee, “New Magnetic Phenomena in Liquid He^3 below 3 mK”, *Physical Review Letters* **29**, 920 (1972).
- ⁵⁷N. Zhelev, M. Reichl, T. S. Abhilash, E. N. Smith, K. X. Nguyen, E. J. Mueller, and J. M. Parpia, “Observation of a new superfluid phase for ^3He embedded in nematically ordered aerogel”, *Nature Communications* **7**, 12975 (2016).
- ⁵⁸D. Vollhardt and P. Wölfle, *The Superfluid Phases of Helium 3* (Taylor and Francis, 1990).
- ⁵⁹S. Autti, V. V. Dmitriev, J. T. Mäkinen, A. A. Soldatov, G. E. Volovik, A. N. Yudin, V. V. Zavjalov, and V. B. Eltsov, “Observation of Half-Quantum Vortices in Topological Superfluid ^3He ”, *Physical Review Letters* **117**, 255301 (2016).
- ⁶⁰J. T. Mäkinen, V. V. Dmitriev, J. Nissinen, J. Rysti, G. E. Volovik, A. N. Yudin, K. Zhang, and V. B. Eltsov, “Half-quantum vortices and walls bounded by strings in the polar-distorted phases of topological superfluid ^3He ”, *Nature Communications* **10**, 237 (2019).
- ⁶¹C. A. M. Castelijns, K. F. Coates, A. M. Guénault, S. G. Mussett, and G. R. Pickett, “Landau critical velocity for a macroscopic object moving in superfluid ^3He -B: Evidence for gap suppression at a moving surface”, *Physical Review Letters* **56**, 69 (1986).
- ⁶²C. J. Lambert, “On the approach to criticality of a vibrating, macroscopic object in superfluid ^3He -B”, *Physica B: Condensed Matter* **165–166**, 653–654 (1990).

- ⁶³D. C. Carless, H. E. Hall, and J. R. Hook, "Vibrating wire measurements in liquid ^3He . I. The normal state", *Journal of Low Temperature Physics* **50**, 583–603 (1983).
- ⁶⁴A. M. Guénault, V. Keith, C. J. Kennedy, S. G. Mussett, and G. R. Pickett, "The mechanical behavior of a vibrating wire in superfluid ^3He -B in the ballistic limit", *Journal of Low Temperature Physics* **62**, 511–523 (1986).
- ⁶⁵D. O. Clubb, O. V. L. Buu, R. M. Bowley, R. Nyman, and J. R. Owers-Bradley, "Quartz Tuning Fork Viscometers for Helium Liquids", *Journal of Low Temperature Physics* **136**, 1–13 (2004).
- ⁶⁶R. Blaauwgeers, M. Blazkova, M. Človečko, V. B. Eltsov, R. de Graaf, J. Hosio, M. Krusius, D. Schmoranzler, W. Schoepe, L. Skrbek, P. Skyba, R. E. Solntsev, and D. E. Zmeev, "Quartz Tuning Fork: Thermometer, Pressure- and Viscometer for Helium Liquids", *Journal of Low Temperature Physics* **146**, 537–562 (2007).
- ⁶⁷D. I. Bradley, S. N. Fisher, A. Ganshin, A. M. Guénault, R. P. Haley, M. J. Jackson, G. R. Pickett, and V. Tsepelin, "The Onset of Vortex Production by a Vibrating Wire in Superfluid ^3He -B", *Journal of Low Temperature Physics* **171**, 582–588 (2013).
- ⁶⁸H. Yano, K. Ogawa, Y. Chiba, K. Obara, and O. Ishikawa, "Anisotropic Formation of Quantum Turbulence Generated by a Vibrating Wire in Superfluid ^4He ", *Journal of Low Temperature Physics* **187**, 515–522 (2017).
- ⁶⁹A. Kraus, A. Erbe, and R. H. Blick, "Nanomechanical vibrating wire resonator for phonon spectroscopy in liquid helium", *Nanotechnology* **11**, 165 (2000).
- ⁷⁰P. Zheng, W. G. Jiang, C. S. Barquist, Y. Lee, and H. B. Chan, "Anomalous Damping of a Microelectromechanical Oscillator in Superfluid ^3He -B", *Physical Review Letters* **117**, 195301 (2016).
- ⁷¹T. Kamppinen and V. B. Eltsov, "Nanomechanical Resonators for Cryogenic Research", *Journal of Low Temperature Physics* **196**, 283–292 (2019).
- ⁷²K. Y. Fong, D. Jin, M. Poot, A. Bruch, and H. X. Tang, "Phonon Coupling between a Nanomechanical Resonator and a Quantum Fluid", *Nano Letters* **19**, 3716–3722 (2019).
- ⁷³H. D. Young, R. A. Freedman, and A. L. Ford, *University Physics with Modern Physics*, 13th ed. (Pearson education, 2011).
- ⁷⁴E. Collin, L. Filleau, T. Fournier, Yu. M. Bunkov, and H. Godfrin, "Silicon Vibrating Wires at Low Temperatures", *Journal of Low Temperature Physics* **150**, 739–790 (2008).
- ⁷⁵D. I. Bradley, S. N. Fisher, A. M. Guénault, R. P. Haley, C. R. Lawson, G. R. Pickett, R. Schanen, M. Skyba, V. Tsepelin, and D. E. Zmeev, "Breaking the superfluid speed limit in a fermionic condensate", *Nature Physics* **12**, 1017–1021 (2016).

- ⁷⁶P. Günther, U. Fischer, and K. Dransfeld, "Scanning near-field acoustic microscopy", *Applied Physics B* **48**, 89–92 (1989).
- ⁷⁷K. Karrai and R. D. Grober, "Piezoelectric tip-sample distance control for near field optical microscopes", *Applied Physics Letters* **66**, 1842 (1995).
- ⁷⁸R. D. Grober, J. Acimovic, J. Schuck, D. Hessman, P. J. Kindlemann, J. Hespanha, A. S. Morse, K. Karrai, I. Tiemann, and S. Manus, "Fundamental limits to force detection using quartz tuning forks", *Review of Scientific Instruments* **71**, 2776 (2000).
- ⁷⁹D. I. Bradley, P. Crookston, M. J. Fear, S. N. Fisher, G. Foulds, D. Garg, A. M. Guénault, E. Guise, R. P. Haley, O. Kolosov, G. R. Pickett, R. Schanen, and V. Tsepelin, "Measuring the Prong Velocity of Quartz Tuning Forks Used to Probe Quantum Fluids", *Journal of Low Temperature Physics* **161**, 536–547 (2010).
- ⁸⁰S. Holt and P. Skyba, "Electrometric direct current I/V converter with wide bandwidth", *Review of Scientific Instruments* **83**, 064703 (2012).
- ⁸¹J. E. Sader, "Frequency response of cantilever beams immersed in viscous fluids with applications to the atomic force microscope", *Journal of Applied Physics* **84**, 64 (1998).
- ⁸²M. Morishita, T. Kuroda, A. Sawada, and T. Satoh, "Mean free path effects in superfluid ^4He ", *Journal of Low Temperature Physics* **76**, 387–415 (1989).
- ⁸³D. I. Bradley, A. M. Guénault, R. P. Haley, G. R. Pickett, and V. Tsepelin, "Andreev Reflection in Superfluid ^3He : A Probe for Quantum Turbulence", *Annual Review of Condensed Matter Physics* **8**, 407–430 (2017).
- ⁸⁴C. Bäuerle, Yu. M. Bunkov, S. N. Fisher, and H. Godfrin, "Temperature scale and heat capacity of superfluid $^3\text{He-B}$ in the 100 μK range", *Physical Review B* **57**, 14381 (1998).
- ⁸⁵F. Pobell, *Matter and Methods at Low Temperatures*, 3rd ed. (Springer, 2007).
- ⁸⁶D. J. Cousins, S. N. Fisher, A. M. Guénault, R. P. Haley, I. E. Miller, G. R. Pickett, G. N. Plenderleith, P. Skyba, P. Y. A. Thibault, and M. G. Ward, "An Advanced Dilution Refrigerator Designed for the New Lancaster Microkelvin Facility", *Journal of Low Temperature Physics* **114**, 547–570 (1998).
- ⁸⁷P. Das, R. B. de Ouboter, and K. W. Taconis, "A Realization of a London-Clarke-Mendoza Type Refrigerator", in *Low Temperature Physics LT9* (1965), pp. 1253–1255.
- ⁸⁸E. Collin, Yu. M. Bunkov, and H. Godfrin, "Addressing geometric nonlinearities with cantilever microelectromechanical systems: Beyond the Duffing model", *Physical Review B* **82**, 235416 (2010).

- ⁸⁹C. Hutter, D. Platz, E. A. Tholén, T. H. Hansson, and D. B. Haviland, “Reconstructing Nonlinearities with Intermodulation Spectroscopy”, *Physical Review Letters* **104**, 050801 (2010).
- ⁹⁰D. Platz, D. Forchheimer, E. A. Tholén, and D. B. Haviland, “The role of nonlinear dynamics in quantitative atomic force microscopy”, *Nanotechnology* **23**, 265705 (2012).
- ⁹¹R. W. Stark and W. H. Heckl, “Higher harmonics imaging in tapping-mode atomic force microscopy”, *Review of Scientific Instruments* **74**, 5111 (2003).
- ⁹²T. R. Rodríguez and R. García, “Compositional mapping of surfaces in atomic force microscopy by excitation of the second normal mode of the microcantilever”, *Applied Physics Letters* **84**, 449 (2004).
- ⁹³S. Jesse, S. V. Kalinin, R. Proksch, A. P. Baddorf, and B. J. Rodriguez, “The band excitation method in scanning probe microscopy for rapid mapping of energy dissipation on the nanoscale”, *Nanotechnology* **18**, 435503 (2007).
- ⁹⁴E. A. Tholén, D. Platz, D. Forchheimer, V. Schuler, M. O. Tholén, C. Hutter, and D. B. Haviland, “Note: The intermodulation lockin analyzer”, *Review of Scientific Instruments* **82**, 0261109 (2011).
- ⁹⁵M. Blažková, D. Schmoranzer, and L. Skrbek, “On cavitation in liquid helium in a flow due to a vibrating quartz fork”, *Low Temperature Physics* **34**, 298 (2008).
- ⁹⁶D. Duda, P. Švančara, M. La Mantia, M. Rotter, D. Schmoranzer, O. Kolosov, and L. Skrbek, “Cavitation Bubbles Generated by Vibrating Quartz Tuning Fork in Liquid ^4He Close to the λ -Transition”, *Journal of Low Temperature Physics* **187**, 376–382 (2017).
- ⁹⁷G. Tartini, *Trattato di musica secondo la vera scienza dell’ armonia* (Nella stamperia del Seminario, aspresso G. Manfré, 1754).
- ⁹⁸D. Platz, D. Forchheimer, E. A. Tholén, and D. B. Haviland, “Interaction imaging with amplitude-dependence force spectroscopy”, *Nature Communications* **4**, 1360 (2013).
- ⁹⁹W. I. Glaberson and R. J. Donnelly, “Growth of Pinned Quantized Vortex Lines in Helium II”, *Physical Review* **141**, 20 (1966).
- ¹⁰⁰G. W. Stagg, N. G. Parker, and C. F. Barenghi, “Superfluid Boundary Layer”, *Physical Review Letters* **118**, 135301 (2017).
- ¹⁰¹D. I. Bradley, M. J. Fear, S. N. Fisher, A. M. Guénault, R. P. Haley, C. R. Lawson, P. V. E. McClintock, G. R. Pickett, R. Schanen, V. Tsepelin, and L. A. Wheatland, “Transition to turbulence for a quartz tuning fork in superfluid ^4He ”, *Journal of Low Temperature Physics* **156**, 116–131 (2009).

- ¹⁰²D. Schmoranzner, M. J. Jackson, V. Tsepelin, M. Poole, A. J. Woods, M. Človečko, and L. Skrbek, “Multiple critical velocities in oscillatory flow of superfluid ^4He due to quartz tuning forks”, *Physical Review B* **94**, 214503 (2016).
- ¹⁰³D. Garg, V. B. Efimov, M. Giltrow, P. V. E. McClintock, L. Skrbek, and W. F. Vinen, “Behavior of quartz forks oscillating in isotopically pure ^4He in the $T \rightarrow 0$ limit”, *Physical Review B* **85**, 144518 (2012).
- ¹⁰⁴F. V. Kusmartsev, “Fluctuative Mechanism of Vortex Nucleation in the Flow of ^4He ”, *Physical Review Letters* **76**, 1880 (1996).
- ¹⁰⁵H. A. Nichol, L. Skrbek, P. C. Hendry, and P. V. E. McClintock, “Experimental investigation of the macroscopic flow of He-II due to an oscillating grid in the zero temperature limit”, *Physical Review E* **70**, 056307 (2004).
- ¹⁰⁶R. Goto, S. Fujiyama, H. Yano, Y. Nago, N. Hashimoto, K. Obara, O. Ishikawa, M. Tsubota, and T. Hata, “Turbulence in Boundary Flow of Superfluid ^4He Triggered by Free Vortex Rings”, *Physical Review Letters* **100**, 045301 (2008).
- ¹⁰⁷D. E. Zmeev, F. Pakpour, P. M. Walmsley, A. I. Golov, W. Guo, D. N. McKinsey, G. G. Ihas, P. V. E. McClintock, S. N. Fisher, and W. F. Vinen, “Excimers He_2^* as Tracers of Quantum Turbulence in ^4He in the $T = 0$ Limit”, *Physical Review Letters* **110**, 175303 (2013).
- ¹⁰⁸M. S. Paoletti, M. E. Fisher, K. R. Sreenivasan, and D. P. Lathrop, “Velocity Statistics Distinguish Quantum Turbulence from Classical Turbulence”, *Physical Review Letters* **101**, 154501 (2008).
- ¹⁰⁹E. A. Guise, “Developing a Quasiparticle Detector for Quantum Turbulence Imaging Studies in Superfluid $^3\text{He-B}$ ”, PhD thesis (Lancaster University, 2014).
- ¹¹⁰A. J. Woods, “Visualisation of Quantum Turbulence in Superfluid $^3\text{He-B}$ Using a Novel 2D Quasiparticle Detector”, PhD thesis (Lancaster University, 2015).
- ¹¹¹S. N. Fisher, A. M. Guénault, C. J. Kennedy, and G. R. Pickett, “Beyond the Two-Fluid Model: Transition from Linear Behavior to a Velocity-Independent Force on a Moving Object in $^3\text{He-B}$ ”, *Physical Review Letters* **63**, 2566 (1989).
- ¹¹²C. J. Lambert, “Theory of pair breaking by vibrating macroscopic objects in superfluid ^3He ”, *Physica B: Condensed Matter* **178**, 294–303 (1992).
- ¹¹³V. Tsepelin, A. W. Baggaley, Y. A. Sergeev, C. F. Barenghi, S. N. Fisher, G. R. Pickett, M. J. Jackson, and N. Suramlishvili, “Visualization of quantum turbulence in superfluid $^3\text{He-B}$: Combined numerical and experimental study of Andreev reflection”, *Physical Review B* **96**, 054510 (2017).
- ¹¹⁴C. F. Barenghi, Y. A. Sergeev, and N. Suramlishvili, “Ballistic propagation of thermal excitations near a vortex in superfluid $^3\text{He-B}$ ”, *Physical Review B* **77**, 104512 (2008).

- ¹¹⁵D. I. Bradley, “Repetitive Single Vortex-Loop Creation by a Vibrating Wire in Superfluid $^3\text{He-B}$ ”, *Physical Review Letters* **84**, 1252 (2000).
- ¹¹⁶J. Rysti and J. Tuoriniemi, “Quartz Tuning Forks and Acoustic Phenomena: Application to Superfluid Helium”, *Journal of Low Temperature Physics* **177**, 133–150 (2014).
- ¹¹⁷E. Pentti, J. Rysti, A. Salmela, A. Sebedash, and J. Tuoriniemi, “Studies on Helium Liquids by Vibrating Wires and Quartz Tuning Forks”, *Journal of Low Temperature Physics* **165**, 132 (2011).
- ¹¹⁸V. A. Bakhvalova, I. A. Gritsenko, E. Rudavskii, V. K. Chagovets, and G. A. Sheshin, “Studies of kinetic processes in a concentrated $^3\text{He-}^4\text{He}$ solution using an oscillating tuning fork”, *Low Temperature Physics* **41**, 502 (2015).
- ¹¹⁹A. Salmela, J. Tuoriniemi, and J. Rysti, “Acoustic Resonances in Helium Liquids Excited by Quartz Tuning Forks”, *Journal of Low Temperature Physics* **162**, 678–685 (2011).
- ¹²⁰T. S. Riekkii, J. Rysti, J. T. Mäkinen, A. P. Sebedash, V. B. Eltsov, and J. T. Tuoriniemi, “Effects of ^4He Film on Quartz Tuning Forks in ^3He at Ultra-low Temperatures”, *Journal of Low Temperature Physics* **196**, 73–81 (2019).
- ¹²¹R. J. Donnelly and C. F. Barenghi, “The Observed Properties of Liquid Helium at the Saturated Vapor Pressure”, *Journal of Physical and Chemical Reference Data* **27**, 1217 (1998).
- ¹²²B. M. Abraham, Y. Eckstein, J. B. Ketterson, M. Kuchnir, and P. R. Roach, “Velocity of sound, Density and Grüneisen Constant in Liquid ^4He ”, *Physical Review A* **1**, 250 (1970).
- ¹²³K. R. Atkins, “Third and Fourth Sound in Helium II”, *Physical Review* **113**, 962 (1959).
- ¹²⁴G. G. Stokes, “On the effect of the internal friction of fluids on the motion of pendulums”, *Transactions of the Cambridge Philosophical Society* **9**, 8 (1852).
- ¹²⁵H. L. Larquer, S. G. Sydoriak, and T. R. Roberts, “Sound Velocity and Adiabatic Compressibility of Liquid Helium Three”, *Physical Review* **113**, 417 (1959).
- ¹²⁶M. Človečko, E. Gažo, M. Skyba, and P. Skyba, “NMR-like effect on the anisotropic magnetic moment of surface bound states in the topological superfluid $^3\text{He-B}$ ”, *Physical Review B* **99**, 104518 (2019).
- ¹²⁷D. I. Bradley, S. N. Fisher, A. M. Guénault, R. P. Haley, N. Mulders, G. R. Pickett, D. Potts, P. Skyba, J. Smith, V. Tsepelin, and R. C. V. Whitehead, “Magnetic Phase Transition in a Nanonetwork of Solid ^3He in Aerogel”, *Physical Review Letters* **105**, 125303 (2010).

- ¹²⁸A. M. Guénault, R. P. Haley, S. Kafanov, M. T. Noble, G. R. Pickett, M. Poole, R. Schanen, V. Tsepelin, J. Vonka, T. Wilcox, and D. E. Zmeev, “Acoustic damping of quartz tuning forks in normal and superfluid ^3He ”, *Physical Review B* **100**, 104526 (2019).